Universidad Autónoma de Baja California
Instituto de Ingeniería
Maestría y Doctorado en Ciencias e Ingeniería

‘‘Fabricación y caracterización de nanoestructuras por FIB- SEM para aplicaciones electrónicas y optoelectrónicas’’

TESIS
Que para obtener el grado de:

Doctor en Ingeniería

Presenta

Oscar Manuel Pérez Landeros

Director
Dr. Nicola Radnev Nedev

Co-Director
Dr. Mario Alberto Curiel Álvarez

Mexicali, Baja California Agosto de 2019

1 Contenido.

2 Introducción.

El sector manufacturero electrónico en México, comprende principalmente aparatos o componentes que procesan algún tipo de información. Esta industria ha venido incrementando su producción desde los últimos años y se prospecta una producción de 5571 mmd para el 2020, este sector manufacturero se divide en 5 subsectores: audio y video, computación y oficina, semiconductores, comunicaciones, y equipo médico e instrumentos de precisión, medición, navegación, control y ópticos.

El subsector de semiconductores ha sido por varios años el de mayor contribución. México, según datos de oficiales se encuentra en condiciones competitivas a nivel mundial. México destaca como el país con menores costos de operación en manufactura de electrónicos en comparación con Estados Unidos. [1]

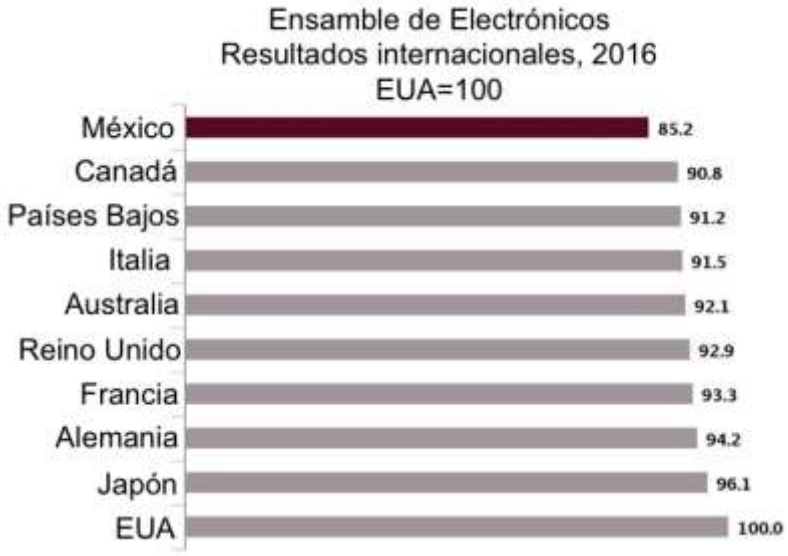

Tabla 2.1. Índice de costo.

Con la invención del transistor la industria electrónica se redujo en tamaño y costo de producción de tal manera que el ritmo de integración se duplica cada dos años. Esto ya se había pronosticado en 1965 por Gordon Moore cofundador de Intel, con su famosa "Ley de Moore". Esta ley establece que cada dos años la densidad de transistores en una oblea se verá duplicada y ha tenido vigencia hasta la actualidad. [2]

La ahora, industria Microelectrónica se enfrenta a retos cada vez más difíciles, relacionados con esta reducción ya que se alcanzan límites físicos de fabricación con las actuales técnicas, así como los límites físicos para la operación correcta de los dispositivos. Esto conlleva a la miniaturización también de las técnicas y a la búsqueda de nuevos métodos de fabricación, desarrollo de nuevos materiales o uso de materiales convencionales con dimensiones "nano", cuales muestran nuevas propiedades en comparación con las propiedades de materiales de bulto (bulk properties).

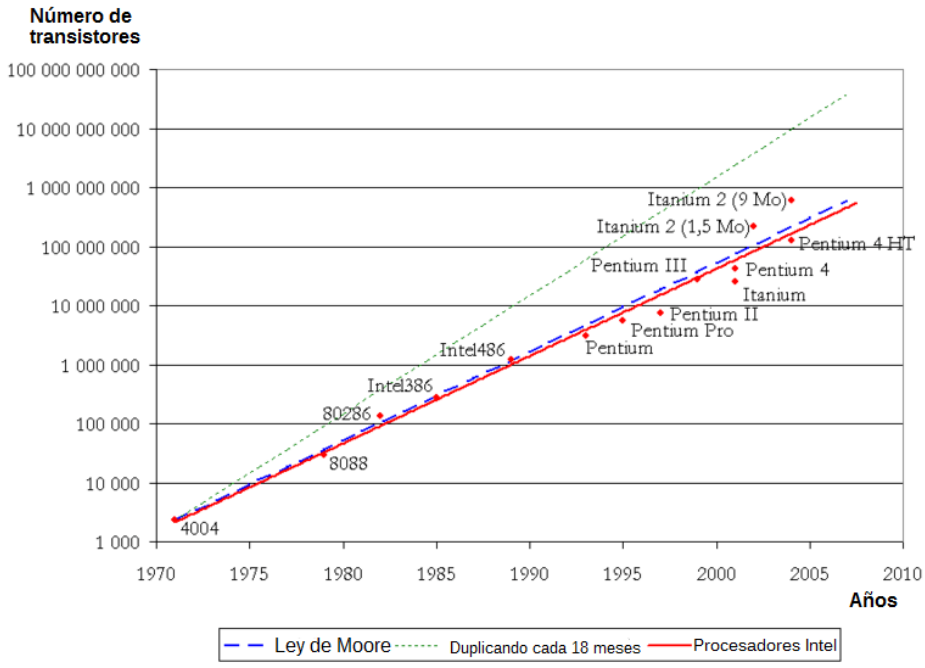

Tabla 2.2. Densidad de transistores integrados en los procesadores Intel vs Ley de Moore.

2.1 Planteamiento del problema.

La microelectrónica se encuentra en constante evolución, los dispositivos microelectrónicos y optoelectrónicos están migrando a la nanoescala (con dimensiones entre 10 y 100 nanómetros). Las tecnologías actuales enfrentan un reto en cuanto a fabricación de componentes electrónicos. En la escala de los nanómetros, complicaciones en la fabricación electrónica se acentúan, sin embargo, fenómenos y propiedades nuevas y en algunos casos muy útiles también comienzan a surgir. Estas propiedades pueden ser utilizadas; en combinación con mecanismos a nivel nanoestructuras, para medir, controlar, almacenar y convertir señales eléctricas, ópticas y/o impulsos mecánicos. Los mecanismos nanoestructurados, aunque de gran utilidad, representan también un reto más de fabricación. Toda esta fusión de propiedades resulta en micro-dispositivos conocidos como MEMS (Micro-Electro-Mechanical Systems) Estos retos que se enfrentan en la industria microelectrónica forman un amplio campo de investigación. Este campo multidisciplinario ha sido testigo de un crecimiento explosivo desde hace dos décadas y existen muchas revistas dedicadas especialmente a la nanociencia ciencia y tecnología de MEMS.

2.2 Objetivo Principal.

Estudiar las propiedades de materiales nanoestructurados a base de Si cristalino y amorfo, óxido de silicio y los metales; Pt, Al, Au Cu y Ag, para propuestas en posibles aplicaciones de estos en dispositivos electrónicos y optoelectrónicos.

2.2.1 Objetivos específicos.

- Fabricar y caracterizar películas de platino nanoestructuradas por medio del sistema FIB-SEM
- Fabricar y caracterizar películas de SiO_2 nanoestructuradas por medio del sistema FIB-SEM
- Definir nanoestructuras en base de Si cristalino utilizando erosión con iones de Ga^+ (FIB-SEM system)
- Definir nanoestucturas de óxido de silicio partiendo de una capa continua delgada o ultradelgada de SiO_2 obtenida via oxidación térmica o por espurreo
- Definir nanoestucturas de Al, Au Cu o Ag partiendo de películas delgadas depositadas por evaporación térmica
- Estudiar a detalle las propiedades de las nanoestructuras fabricadas.
- Fabricar nanoestructuras basadas en Si para su posible aplicación en MEMS.

2.3 Justificación.

El estudio de los materiales nanoestructurados en la industria microelectrónica debe su interés a la creciente demanda de velocidad de procesamiento y capacidad de almacenamiento en dispositivos electrónicos de uso común, educativo e industrial.

La industria semiconductora; en el país, ha venido desarrollándose rápidamente. Por su abundancia en el planeta y sus propiedades electrónicas, dispositivos basados en silicio se fabrican por variedad de técnicas físicas y químicas. Sin embargo, este elemento ha demostrado excelentes propiedades mecánicas en la micro y nano escala por lo que tiene extensa aplicación en tecnologías MEMS

El presente trabajó se enfoca en la fabricación de nanoestructuras basadas en silicio para su utilización en dispositivos electrónicos.

Las técnicas de fabricación físicas principalmente utilizadas son evaporación térmica, recocido térmico rápido y erosión por haz de iones focalizados. Tecnologías de fabricación químicas también son requeridas en procesos de capa de sacrificio.

La realización de este proyecto es fundamental para extender el alcance en sensores electrónicos, optoelectrónicos y electroquímicos en el “Laboratorio de Semiconductores, Microelectrónica y Nanotecnología” del Instituto de Ingeniería de la UABC, así como generar una nueva línea de investigación en el ramo de microactuadores.

3 Marco teórico.

3.1 Nanomateriales.

Nano es un prefijo que denota un factor de 10^{-9}. El término se asocia muchas veces al intervalo de tiempo de un nanosegundo; la billonésima parte de un segundo, y a la escala de longitud del nanómetro (nm); la billonésima parte de un metro. En sus más amplios términos, nanociencia, nanotecnología, y nanomateriales. [3] Por convención, cualquier estructura o material más pequeño que 100 nm en al menos una dimensión, sería una nano estructura o nanomaterial, aunque el limite no está estrictamente establecido. [4] Los nanomateriales se clasifican en 3 tipos según sus dimensiones nanométricas en espacio tridimensional. Un material 0D, es un material con dimensiones igual o menore a 100 nm en los tres ejes espaciales, esto quiere decir que ninguna de sus dimensiones supera los 100nm. Si el nanomaterial supera los 100 nm en una de sus dimensiones se clasifica 1D, y si los supera en dos de sus dimensiones será 2D. Los materiales que superan 100 nm en tres dimensiones son llamados materiales de bulto.

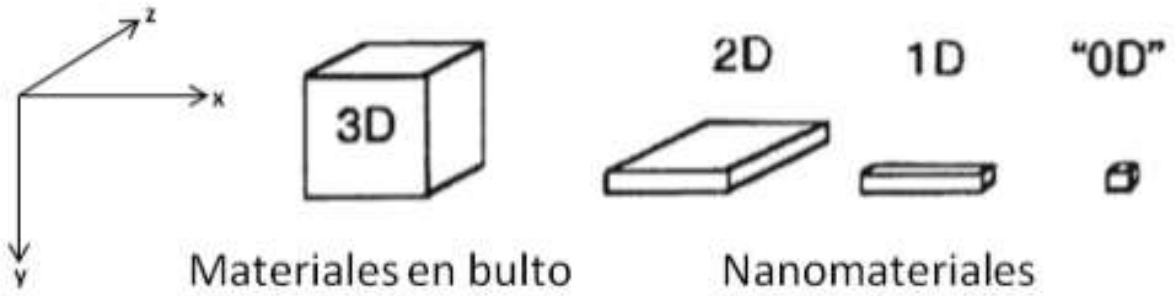

Figura 3.1.1. Clasificación de los materiales según sus dimensiones nanométricas.

La característica principal de un nanomaterial, es que sus propiedades de bulto se ven modificadas o alteradas a la nanoescala, esto se debe a que los átomos de la superficie compiten de forma igualitaria o en mayoría contra los átomos internos. En un material de bulto, donde los átomos internos son mayoría, los átomos superficiales no contribuyen en gran medida en las propiedades que estos presentan.

3.2 Materiales semiconductores.

Los semiconductores son el grupo de materiales que tienen conductividad eléctrica intermedia entre metales y aislantes. Esto significa que la conductividad de estos materiales se puede variar órdenes de magnitud con la temperatura, excitación óptica, y contenido de impurezas. Esta variabilidad de propiedades eléctricas hace de los materiales semiconductores la selección natural para la investigación de dispositivos electrónicos.

Los materiales semiconductores se encuentran en la columna IV y las columnas vecinas de la tabla periódica. En la columna IV, silicio y germanio, son llamados

semiconductores elementales ya que están compuestos de átomos de una misma especie. Además de los materiales elementales, compuestos atómicos de las columnas III y V, así como ciertas combinaciones de las columnas II y VI, y de IV, forman semiconductores compuestos. [5]

a)	II	III	IV	V	VI
		B	C	N	
		Al	Si	P	S
	Zn	Ga	Ge	As	Se
	Cd	In		Sb	Te

b)	Elemental	Compuestos IV	Compuestos binarios III-V	Compuestos binarios II-VI
	Si	SiC	AlP	ZnS
	Ge	SiGe	AlAs	ZnSe
			AlSb	ZnTe
			GaN	CdS
			GaP	CdSe
			GaAs	CdTe
			GaSb	
			InP	
			InAs	
			InSb	

Tabla 3.1. Materiales semiconductores: (a) elementos semiconductores de la tabla periódica; (b) semiconductores elementales y compuestos.

3.2.1 Estructura atómica de un sólido.

Los sólidos exhiben un rango de propiedades extremadamente amplio, lo que los hace tan útiles e indispensables para la humanidad. Mientras que nuestra familiaridad con tantos distintos tipos de sólidos hacen de este hecho poco impresionante, es en efecto extraordinario cuando vemos sus orígenes. El origen de todas las propiedades de los sólidos no es otra cosa que la interacción entre electrones en las capas externas de sus átomos, los llamados electrones de valencia. Estos electrones interactúan entre ellos y con los núcleos de los átomos constituyentes. [6]

Un sólido cristalino se distingue por el hecho de que los átomos que conforman el cristal se encuentran ordenados de manera periódica. Esto es, hay algunos arreglos básicos de átomos que se repiten a lo largo de todo el sólido. Sin embargo no todos los sólidos son cristales (Figura 1); algunos no tienen absolutamente ninguna arreglo periódico (sólidos amorfos), y otros están compuestos de muchas regiones de pequeños cristales de distinta orientación (sólidos policristalinos). [5]

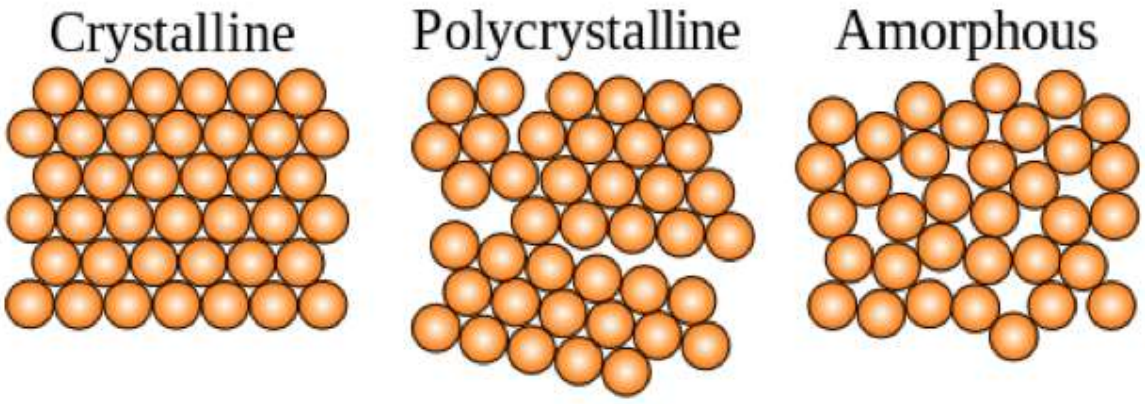

Figura 3.2.1. Tipos de sólido de acuerdo a su arreglo atómico: (a) sólido cristalino, (b) sólido policristalino, (c) sólido amorfo.

3.2.2 Silicio.

Hasta la fecha, los científicos han identificado más de 100 diferentes elementos. Uno de los más importantes y común de estos es el silicio (Si). Cuando las personas escuchan la palabra “silicio”, la mayoría piensan en *Silicon Valley*, donde muchas compañías de alta tecnología tienen sus sede (*Silicon Valley* debe su sobrenombre al silicio). Las personas también piensan en silicón, una clase de compuesto que contiene silicio, oxigeno, carbono, e hidrógeno. Las siliconas son usadas con varios propósitos, así para implantes de cuerpo, como para brazos artificiales, piernas, o pechos.

El silicio es el segundo elemento más común de la tierra, aportando más del 28% de la masa total. También, es el séptimo elemento más abundante del universo entero.

Leyendo la tabla periódica podemos encontrar el símbolo Si del elemento silicio. Con número atómico 14 y masa 28.08, podemos encontrarlo en el grupo 14 ó IVA.

Elementos en un mismo grupo usualmente comparten características, o propiedades. Muchas veces reaccionan con otros elementos o compuestos en forma similar. [7]

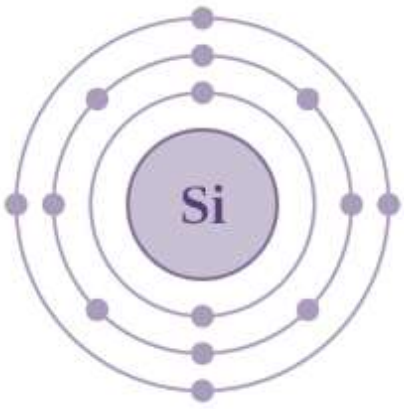

Figura 3.2.2. Modelo de Bohr de un solo átomo de silicio.

3.3 Materiales para sistemas microelectro-mecánicos.

Sin duda alguna, una de las tecnologías más increíbles desarrolladas en las últimas décadas del siglo XX fue en el área de los dispositivos microelectromecánicos (MEMS). Estos MEMS consisten en estructuras mecánicas y eléctricas microfabricadas trabajando en conjunto para percibir o controlar el ambiente local. No fue accidente que el desarrollo de los MEMS haya acelerado rápidamente durante 1990, ya que el campo podía tomar ventajas de las innovaciones en términos de proceso, equipos y materiales durante la revolución de circuitos integrados de 1960-80s. Una comprensión integral de los MEMS requiere de un conocimiento maduro en los materiales usados para construir dispositivos, ya que las propiedades del material de cada componente pueden influenciar el desempeño de cada del sistema. Debido a que la fabricación de MEMS muchas veces depende del uso de materiales de estructura, sacrificio, y máscaras en un mismo sustrato, asuntos relacionados a la selectividad de grabados químicos, adhesión, microestructura, y una serie de otras propiedades de considerable importancia en el diseño. Una discusión sombre “materiales” para MEMS es en realidad una discusión sobre “sistemas de materiales” para MEMS, ya que las tecnologías de fabricación raramente utilizan un único material sino más bien una colección de ellos, ya cada uno con una función crítica. [8]

Dispositivos MEMS son en la actualidad usados en nuestro día a día sin saber siquiera que existen. Puedes encontrar más de un MEMS en tu celular, por dar el ejemplo más sencillo; el giroscopio y el acelerómetro, estos dos MEMS son los encargados de que tu aplicación de mapas se oriente correctamente, o de que la pantalla rote 90 grados al girar el celular. Otras aplicaciones en un celular pueden hacer uso de estos

dispositivos, para por ejemplo contar los pasos en el día, medir velocidad o aceleración, apagar o encender el celular, entre muchas otras. Otro aparato menos común; pero muy usado, basados totalmente en MEMS, es el proyector y el proyector digital de cine, basados en la tecnología MEMS pero ya que su función principal es la de reflejar o no la luz que se proyecta de cada pixel son llamados MOEMS (Micro-opto-electro-mechanical systems). [9] [10]

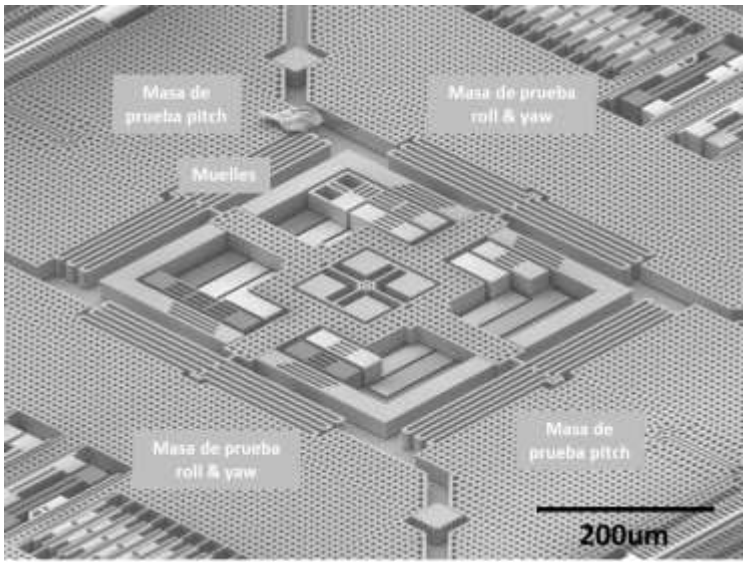

Figura 3.3.1. Masas de prueba de un giroscopio L3G4200D.

3.3.1 Monocristal de silicio.

El uso del silicio como material de sensores microfabricados se data desde1954, cuando se publicó por primera vez el efecto piezoresistivo en germanio y silicio. [11] El resultado de este estudio sugirió que los medidores de tensión hechos de estos materiales podían ser 10 o 20 veces más grande que aquellos hechos de metal, esto eventualmente llevó al desarrollo comercial de medidores de tensión hechos de silicio a finales de 1950. Durante 1960 y a inicios de 1970, técnicas para micromaquinar sustratos de silicio a miniaturas de manera física o química, materiales flexibles en los que se pueden fabricar medidores de tensión fueron desarrollados permitiendo una producción de alto volumen basada en sensores de presión de silicio a mediados del año 1970.

Un mono cristal de silicio tiene una estructura cristalina de diamante (cubica). Tiene una banda prohibida de 1.1 eV, y como muchos otros materiales semiconductores puede ser dopado con impurezas para alterar su conductividad. El fósforo (P) es un elemento común para silicio tipo-n y boro para silicio tipo-p. Un oxido sólido de silicio (SiO_2) que es químicamente estable bajo la mayoría de condiciones puede ser fácil de crecer en superficies de silicio. Mecánicamente, silicio puro es una material frágil con un módulo de Young de aproximadamente 190GPa, un valor comparable con el acero (210 GPa). Siendo de los elementos más abundantes sobre la tierra, el silicio puede ser refinado con tecnología robusta de arena hasta producir material de grado electrónico. Existen procesos industriales de bajo consto capaces de producir obleas de silicio con áreas mayores a las 8 pulgadas de diámetro y muy baja densidad de defectos.

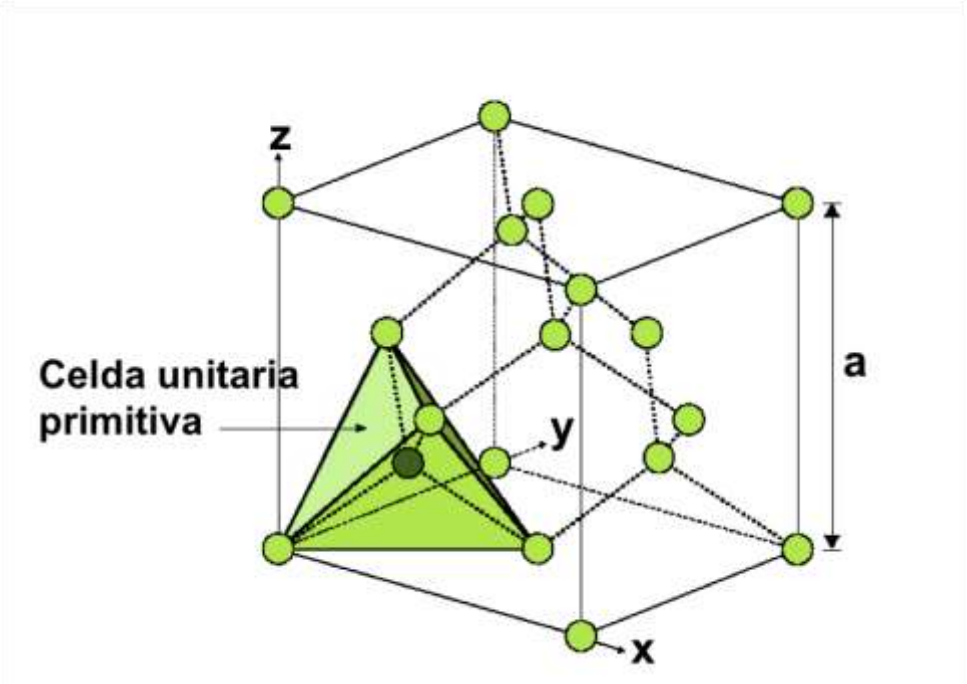

Figura 3.3.2. Estructura del diamante y celda unitaria primitiva.

Para aplicaciones MEMS, un monocristal de silicio tiene varias funciones clave. Los monocristales de silicio son quizá el material de bulto más versátil para micromaquinado, debido a la disponibilidad del bien caracterizado grabado anisotrópico y materiales de mascarillas para grabado. [8]

3.3.2 Polisilicio.

Sin duda el sistema de materiales más común para la fabricación de dispositivos MEMS micromaquinados en superficie utilizan polisilicio como el material estructural primario, dióxido de silicio (SiO_2) como material de sacrificio, y nitruro de silicio (Si_3N_4) como aislante eléctrico de la estructura del dispositivo. La fuerte confianza en estos

materiales se debe en parte al hecho de que estos tres materiales son usados en la fabricación de circuitos integrados, y como resultado, tecnologías de deposición y grabado químico están a la mano y están ampliamente disponibles. Al igual que el mono cristal de silicio, el polisilicio puede ser dopado durante y después del depósito de la película usando procesos estándar para circuitos integrados. Dióxido de silicio puede ser depositado o crecido en un amplio rango de temperaturas (200 a 1150^{o}C) para cumplir con varios procesos y requerimientos. El óxido de silicio es soluble en ácido fluorídrico (HF), sin erosionar las estructuras de polisilicio. [12]

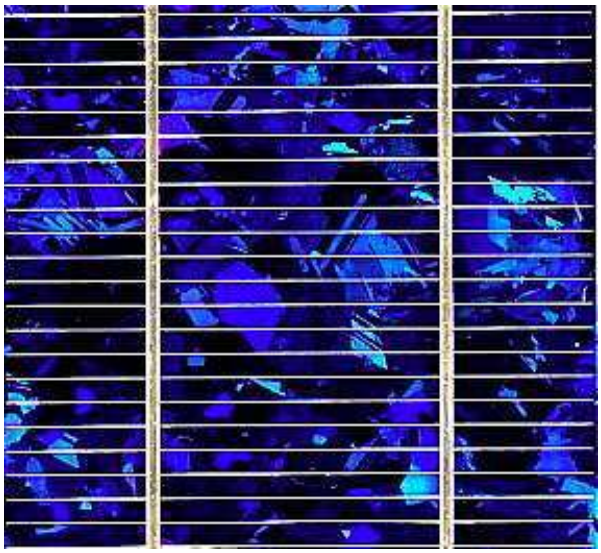

Figura 3.3.3. Celda solar de polisilicio.

3.3.3 Metales.

Los metales son usados en muchos rangos de capacidades distintos, desde máscaras de grabado químico e interconexiones conductivas de películas delgadas hasta componentes estructurales en microsensores y microactuadores. Las películas

metálicas pueden ser depositadas por una amplia variedad de técnicas, siendo las más comunes evaporación térmica, erosión catódica, deposición de vapor químico (CVD), y electroplatinado. Debido a su amplio rango de métodos de deposición, las películas delgadas metálicas son una de las clases de materiales más versátiles usadas en dispositivos MEMS. [8]

Probablemente el aluminio es el metal más utilizado en el micromaquinado de dispositivos. En MEMS, todas las películas delgadas pueden ser utilizadas en conjunto con polímeros como la poliamida ya que estas películas pueden se depositadas por espurreo a bajas temperaturas. En muchos casos estas películas de aluminio son usadas como capa estructural; sin embargo, también puede ser utilizada como capa de sacrificio. La combinación poliamida/aluminio como material estructural y de sacrificio, respectivamente, han demostrado ser efectivas en micromaquinado de superficie. [13] [14]

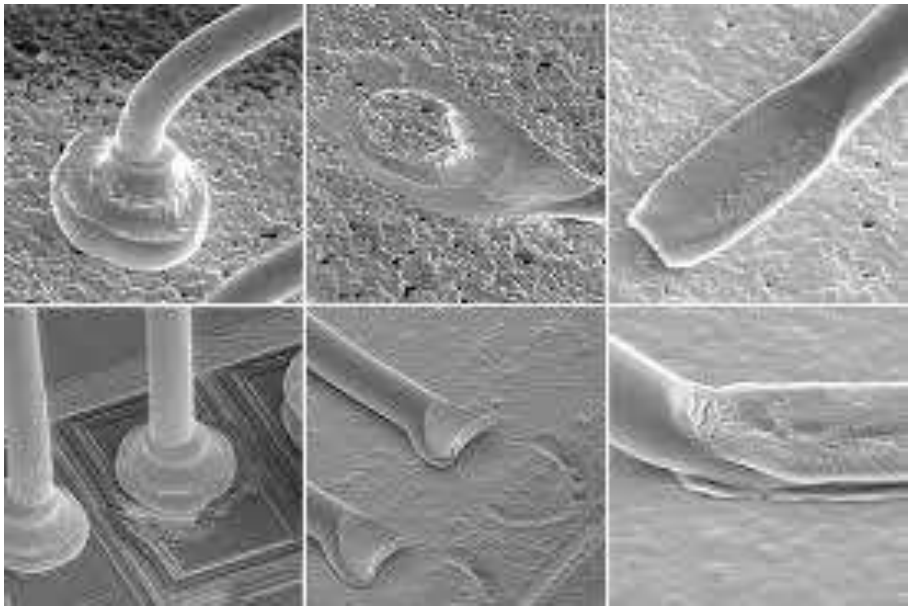

Figura 3.3.4. Algunos tipos de contactos metálicos "wirebond"

3.4 Técnicas y equipos de fabricación y preparación de muestras.

3.4.1 Evaporadora Térmica.

La evaporación térmica, es una técnica física para deposición de películas delgadas y gruesas de distintos materiales, estos pueden ser elementales o compuestos; metales, aislantes o semiconductores. La evaporación se puede llevar a cabo a distintas presiones, sin embargo, es recomendable niveles de alto vacío (Tabla 3.2).

Vacío	Presión
Bajo/Low	750 – .750 torr
Medio/Medium	.750 – 10^{-3} torr
Alto/High	10-3 – 10^{-7} torr
Ultra alto/Ultrahigh	≤ 10^{-7} torr

Tabla 3.2. Nivel de vacío según rangos de presión.

3.4.2 Sistema de doble haz focalizado FIB-SEM.

El sistema de haz doble incorpora dos sistemas en uno; haz de iones focalizados (FIB), y microscopio electrónico de barrido (SEM). Esta combinación ofrece muchas ventajas sobre un sistema de haz único; FIB o SEM, especialmente para preparación de muestras y aplicaciones en microscopía, en las cuales el haz de iones puede ser utilizado para remoción de material en un punto específico, y el SEM para imagen y análisis no destructivo. Los sistemas de doble haz, se presentan en una amplia variedad de técnicas y aplicaciones. Esta combinación es muy útil para la preparación

muestras en sección transversal, usando el haz de electrones para observar y monitorear la sección transversal al tiempo que el haz de iones erosiona normal a la superficie de la muestra. Este monitoreo permite detener la erosión precisamente cuando el área de interés queda expuesta. Típicamente; los sistemas de haz doble, se configuran de modo que entre la columna de electrones, y la columna de iones exista una diferencia de inclinación de 52º, la columna FIB emplea galio (Ga) como fuente de iones, y la columna SEM es de emisión de campo. En este caso, la erosión iónica se debe realizar a una inclinación de 52º para que la erosión se normal a la superficie, y correcciones de imagen por software deben ser utilizadas para la obtención más adecuada de imágenes por SEM. [15]

Estas herramientas del sistema dual FIB-SEM permite determinar espesores de capas o multicapas delgadas y ultra delgadas así como capas más gruesas por medio del corte de sección transversal, comúnmente llamado trinchera, el sistema de inyección de gases (GIS) juega un papel importante ya que mediante el depósito de películas protectoras previo a la realización del corte se protegen zonas de interés. De la misma manera, en laminillas para microscopio de transmisión (TEM) estos depósitos de protección son muy utilizados.

Los materiales que se pueden depositar dentro de una cámara de FIB no solo fungen como protección, también pueden ser utilizados para crear estructuras tridimensionales con distintas utilidades, desde contactos metálicos y aislantes eléctricos, hasta complejas estructuras electromecánicas.

Todos estos procesos pueden ser monitoreados en tiempo real por SEM, permitiendo un control muy avanzado y preciso de los procedimientos realizados. Sin embargo, el haz de electrones tiene también la capacidad de descomponer los gases del GIS y así

depositar películas aún más finas y sin problemas de contaminación de iones como lo es con FIB. [16]

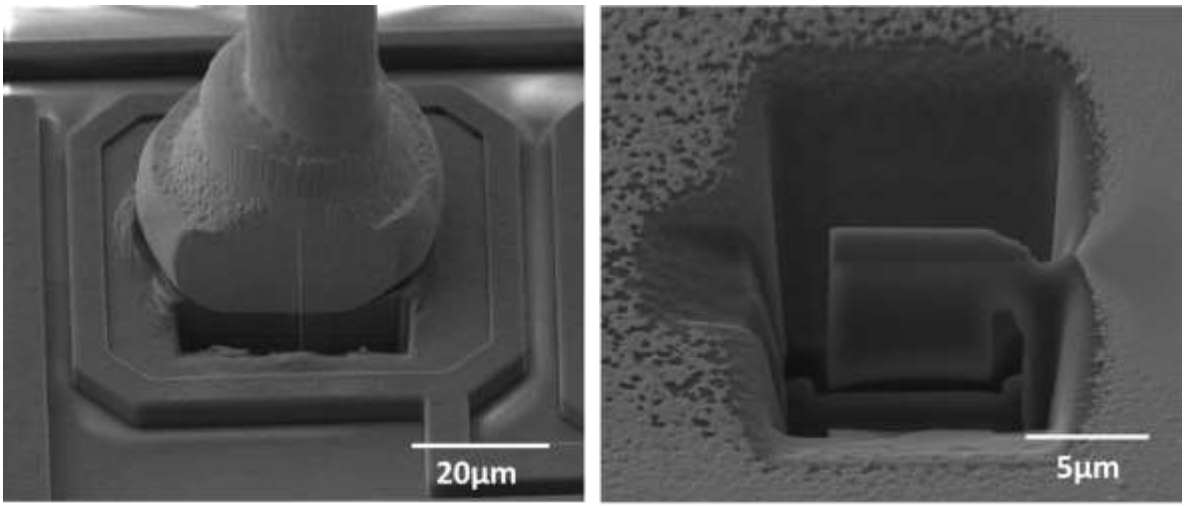

Figura 3.4.1. Vista de la sección transversal de una trinchera en dispositivo electrónico (Izquierda) y corte de preparación de laminilla para TEM (derecha).

3.4.3 Columna SEM.

Las partes principales de la columna de SEM son: Cañón de electrones (Schottky FE Gun), condensador (Condenser (C1)), alineación del cañón (Gun Alignment), lentes intermedios de centrado (IML Centering), estigmadores (Stigmators), bobinas de escaneo (scanning coils),y lente objetiva (Objetive (OBJ)). La configuración de estas partes se muestra en la Figura 3.4.1. [17]

Figura 3.4.2. Configuración general de las partes principales de una columna de electrones por cañón Shottky de emisión de campo del sistema FIB-SEM Lyra 3.

El principio básico del funcionamiento del SEM convencional comienza en la emisión electrónica de un cátodo de tungsteno, los electrones emitidos pasan a través de una columna en un vacío en el rango de 10-7 torr. [18] En la columna, lentes electromagnéticas condensan a los electrones emitidos volviéndolos un haz casi puntual en el rango de10 nm de diámetro. Posteriormente este haz es alineado por lentes de alineación electromagnéticos. Después, el astigmatismo se corrige por el siguiente juego de lentes. Enseguida, bobinas de escaneo controlan el movimiento del haz para el barrido. Por último, el haz es condensado por la lente objetiva una vez más, puntualizándolo sobre la muestra.

3.4.4 Columna FIB.

La columna de iones posiciona un delgado haz de iones “FIB”. Este haz puede ser usado para obtención de imágenes o para crear estructuras definidas sobre cierto espécimen. Las posibilidades y el rendimiento dependen del tipo de columna, la energía de los iones, y la configuración de la óptica iónica. [17]

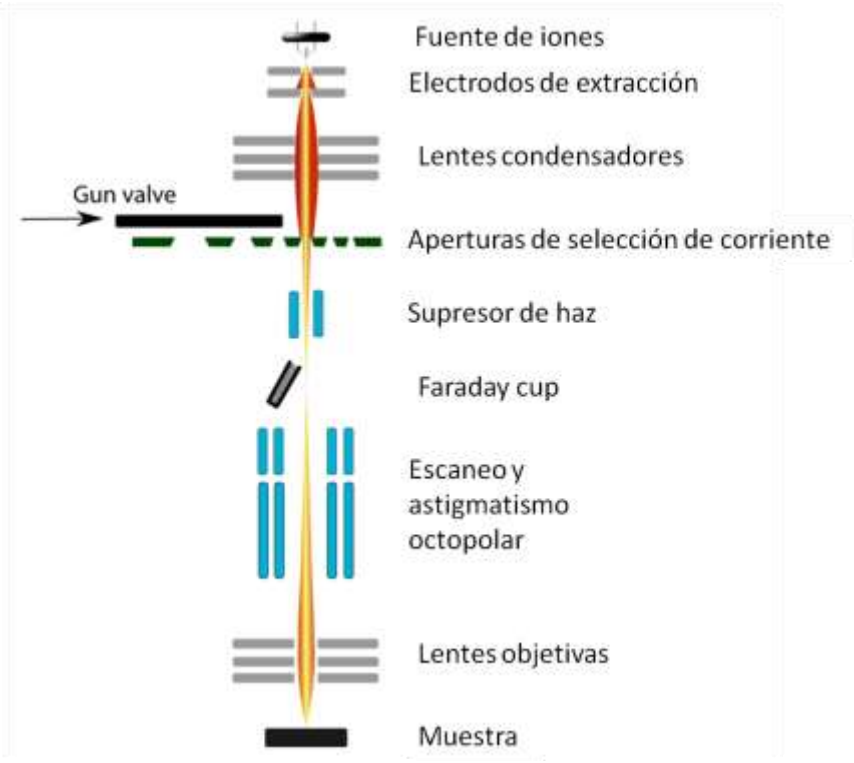

Figura 3.4.3. Configuración general de las partes principales de una columna de iones de Ga^+ del sistema FIB-SEM Lyra 3.

El principio del funcionamiento del sistema FIB es muy parecido al del sistema SEM, iones emitidos desde una fuente de iones; generalmente Ga+, se extraen por medio de electrodos de extracción, estos iones se condensan por medio lentes condensadores, posteriormente orificios de distintos diámetros llamados aperturas de selección de corriente reducen el diámetro del haz y, por lo tanto, la corriente iónica. Después, un octopolo de barrido controla el escaneo y el astigmatismo. Finalmente, lentes objetivas puntualizan el haz sobre la muestra. [17] [18]

3.4.5 Espectroscopia de energía dispersiva de rayos X.

Los rayos X son fotones de energía mayor a la luz UV y menor a los rayos gama. Muy apenas, la menor emergía de rayos X es cerca de 10eV, y su límite superior es 100 keV surgiendo en la naturaleza como resultado de muchos procesos, principalmente cosmológicos. La generación controlada de rayos X casi siempre depende del bombardeo de un objetivo (usualmente metálico) con electrones de energía media. Dos eventos ocurren. Primeramente, los electrones son excitados a estados de energías más altas por los electrones primarios. Los átomos excitados se relajan hasta sus estados de menor energía, liberando su energía excedente en forma de rayos X. Ya que, la energía desprendida es específica del átomo que la libera, se le conoce como “rayos X característicos”. Otro evento que produce rayos X es la desaceleración de los electrones primarios que generan rayos X con energías que van desde 0 hasta la energía del haz primario, a esta energía es llamada “rayos X bremsstrahlung” [19].

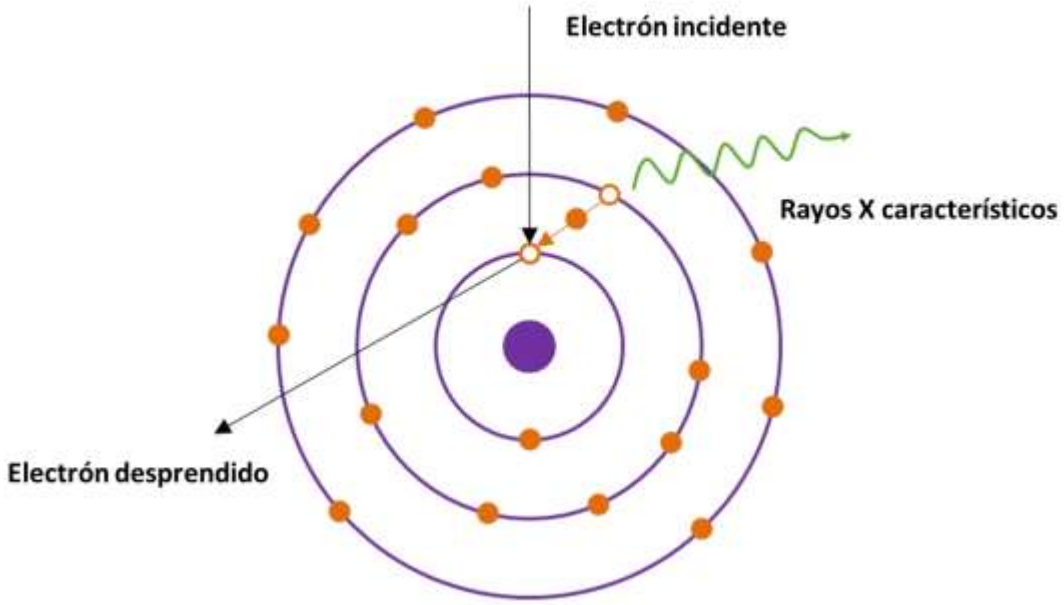

Figura 3.4.4. Representación esquemática de algunos fenómenos que ocurren tras el impacto de un electrón del haz primario. Un electrón incidente puede liberar electrones de sus orbitales o puede otorgar energía suficiente a electrones internos para pasar a un estado excitado donde posteriormente liberará su energía excedente en forma de rayos X.

3.4.6 Elipsometría.

Debido a los avances en las tecnologías de computación, las técnicas de elipsometría espectroscópica se han desarrollado rápidamente, y debido a esto; las áreas de aplicación se han expandido en gran medida.

Elipsometría es una técnica que caracteriza la transmisión o reflexión de las muestras. El Elipsómetro mide el cambio en la polarización de la luz una vez que la luz es reflejada en la muestra o transmitida por la misma. El nombre 'Elipsómetro' resulta del hecho de que la luz polarizada linealmente muchas veces se vuelve 'elíptica' una vez

reflejada. Los ángulos (Ψ, Δ) representan la proporción de amplitud Ψ y la diferencia de fase Δ; entre ondas de luz polarizadas ‘s’ y ‘p’ (Ver Figura 17**)**. Estos valores (Ψ, Δ), son medidos cambiando la longitud de onda de la luz, desde la región del ultravioleta/visible hasta el infrarrojo. [20]

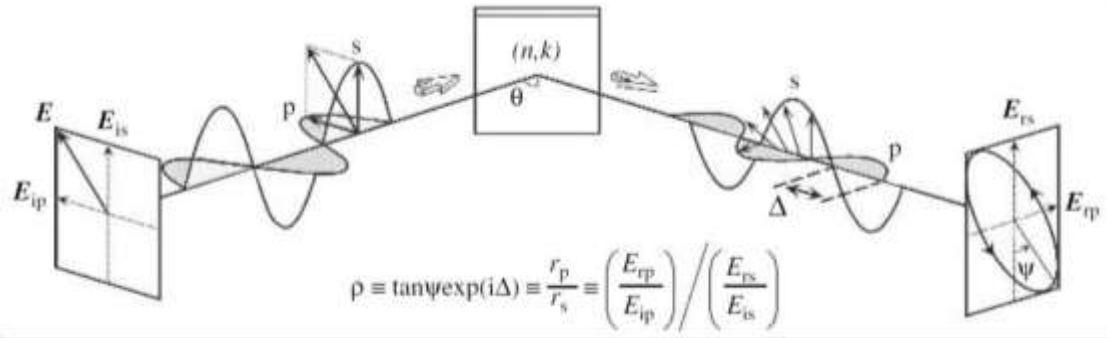

Figura 3.4.5. Espectroscopia elipsométrica, principio básico del funcionamiento.

Esta técnica es muy versátil, útil en materiales elementales como compuestos, con aplicaciones en películas delgadas y ultradelgadas así como metálicas y no metálicas. Esta herramienta es perfecta para análisis rápidos de espesor y rugosidad que te permitan seleccionar muestras para estudios complementarios como por ejemplo microscopias SEM/EDS y secciones trasversales FIB. [21]

4 Diseño de experimentos: Metodología de fabricación y parámetros determinantes.

En esta sección se muestran los experimentos fundamentales para el manejo adecuado de los equipos. Estos experimentos permiten conocer a fondo las capacidades de los equipos y sus posibles aplicaciones.

4.1 Fabricación de muestra M01.

Se fabricó muestra de Si-n con óxido térmico de 12 nm de espesor y una película delgada de oro de 140 nm de espesor. Esta muestra fue utilizada en experimentos bajo distintas condiciones iniciales con el objetivo de determinar las condiciones de trabajo óptimas del equipo de FIB.

La muestra, llamada M01 en este documento, se fabricó bajo condiciones de alto vacío en el equipo de deposición térmica “TE12” (Ver capítulo de equipos y técnicas de fabricación).

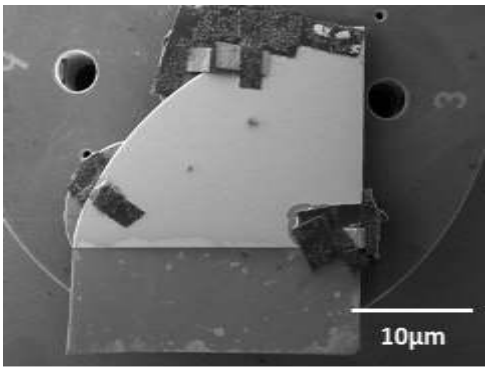

Figura 4.1.1. Oblea de silicio con crecimiento de 12 nm de óxido térmico recubierta con una película de oro de 140 nm de espesor.

El espesor de la película de oro depositada fue estimado por medio de microbalanza de cuarzo y elipsometría de ángulo variable. Posteriormente, se realizaron trincheras para medir el espesor de la película en sección transversal con el sistema dual FIB-SEM.

El procedimiento de trinchera inicia con una inspección del área a baja magnificación; entre 30 y 200x, posteriormente se realiza una inspección detallada de la zona deseada; muchas veces en alta resolución, mayor a 100 kx. Una vez determinada la posición exacta para la trinchera se procede a realizar una cobertura de Pt menor de 10 nm por haz de electrones y otra cobertura mayor de 100 nm por haz de iones (Figura 4.1.2 b)).

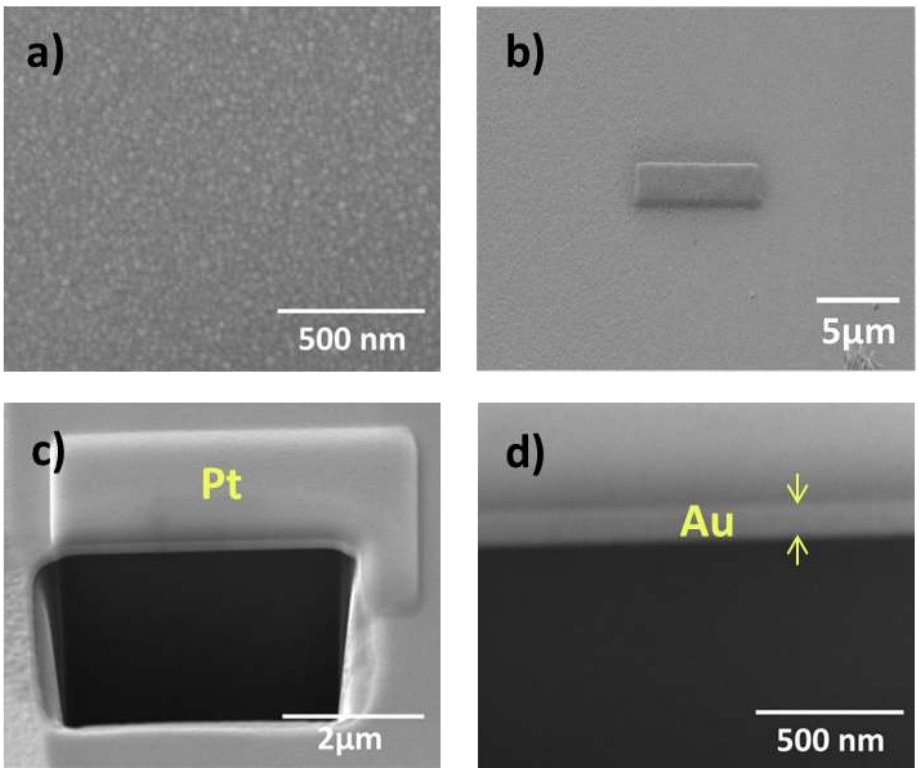

Figura 4.1.2. Proceso de caracterización de película delgada de Au sobre oxido térmico. a) Alta magnificación sobre película sin tratamiento. b) depósito de Pt de protección de 200 nm de espesor. c) Trinchera pulida por haz de iones atreves a través de las películas de Pt y Au y del sustrato. d) Determinación del espesor de la película de interés, Au de aproximadamente 140 nm de grosor.

4.2 Parámetros de erosión.

Para comenzar la experimentación con el equipo FIB-SEM se establecieron 5 parámetros de erosión. Estas configuraciones tienen como función permitir la rápida selección de parámetros de haz de Ga^+ para funciones específicas.

También, en procesos automatizados permiten al usuario seleccionar cambios de corriente o voltajes de aceleración y corrección de haz. La siguiente tabla muestra las típicas configuraciones de uso regular en el cañón de iones.

Parámetro de erosión	Energía	Voltaje de condensador	Voltaje objetiva	Tamaño de apertura	Corriente de haz	Tamaño de punto focal (ss)
1. Burda	30 keV	~25.8 kV	17 kV	400 µm	~11 nA	~2µm
2. Fina, pulído	30 keV	25 kV	16 kV	200 µm	500 pA -1 nA	~500 nm
3. Pulído fino, deposición	30 keV	25 kV	16 kV	100 µm	100 - 200 pA	~200 nm
4. Deposición, imágen	30 keV	25 kV	16 kV	50 µm	~80 pA	~100 nm
5. Imagen de alta resolución	30 keV	25 kV	16 kV	20 µm	~10 pA	~25 nm

Tabla 4.1. Tabla de parámetros de erosión estándar.

Los experimentos de prueba de cada parámetro consisten erosiones de 2x2 µm y captura de imágenes.

Se establecieron 5 configuraciones previas, cada parámetro con una utilidad específica. El parámetro #1, para erosiones de dimensiones en el orden de los micrómetros con una corriente de ~11nA, útil en materiales con tasas bajas de erosión. El parámetro #2 con una corriente de 500 pA – 1 nA, funcional para erosiones de dimensiones menores $1\mu m^3$ y pulídos burdos. Parámetro #3, usado en erosiones finas con calidad de pulido

nanométrico o para depositar precursores GIS. Parámetro #4, usado en la deposición de materiales GIS o captura de imagen. Parámetro #5, utilizado para la adquisición de imágenes de alta resolución, es la configuración de menor corriente.

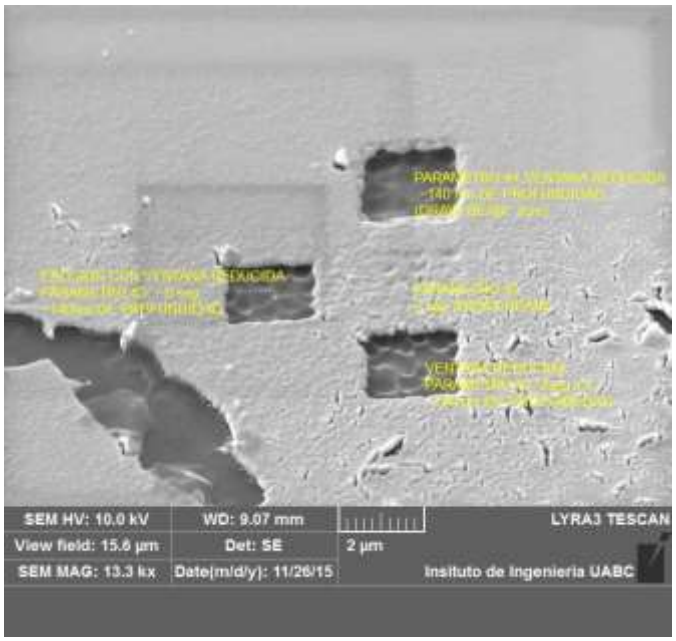

Figura 4.2.1. Algunos efectos de la intensidad de haz en barridos sobre película delgada de Au.

4.3 Ventajas de los diferentes tipos de escaneo.

El barrido convencional llamado “Fly back” (Figura 4.3.1) es utilizado para la captura de imágenes, se caracteriza por barrer línea por línea, de izquierda a derecha. No es muy útil para la limpieza de un área. Este barrido tiene un retado cada vez que inicia una línea por lo que puede acumular material o incrementar la dosis iónica con cada barrido al inicio de cada escaneo.

Figura 4.3.1. Patrón de barrido tipo Fly Back.

Los efectos de este retardo con el escaneo “Fly back” se ven reducidos al utilizar el modo de escaneo “Zig-Zag” (Figura 4.3.2). Este modo barre la superficie de la muestra de izquierda a derecha y de derecha a izquierda lo que compensa el retardo a cada lado del barrido y reduce los efectos de acumulación de dosis.

Figura 4.3.2. Patrón de barrido tipo Zig-Zag.

Los modos de escaneo “Outside-In” y “Inside-Out” (Figura 4.3.3) barren en forma de espiral del centro hacia afuera y de afuera hacia el centro de cualquier geometría de erosión o deposito por haz de iones o electrones.

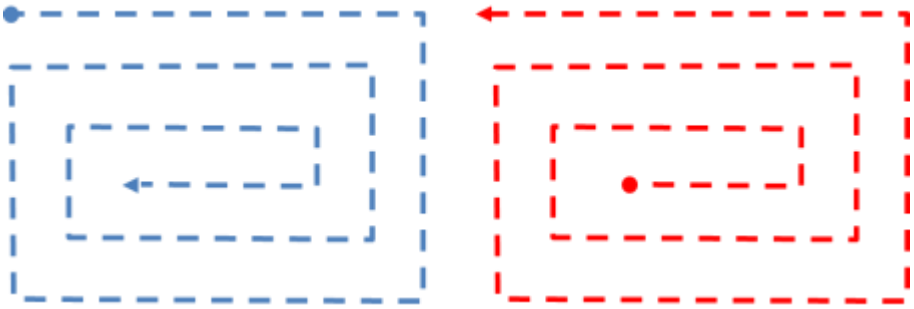

Figura 4.3.3. Patrones de barrido tipo Outside-In (Azul) e Inside-Out (Rojo).

Para limpiar una zona, el barrido “RLE” (Figura 4.3.4) aporta los mejores resultados, este modo de escaneo comienza vertical y termina horizontal. También es útil para generar patrones de cuadriculas que dependen del espaciamiento entre líneas de escaneo, parámetro que puede modificarse desde la ventana de diseño del “Draw beam”.

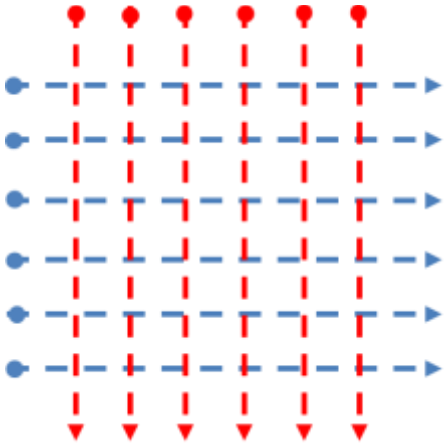

Figura 4.3.4. Patrón de barrido tipo RLE.

4.4 Geometrías simples.

4.4.1 Perímetros.

En este experimento se realizaron erosiones de geometrías simples o sin relleno (Figura 4.4.1). Estas geometrías poseen la mejor resolución de línea ya que se basan en los parámetros de haz preestablecidos. Es decir, el espesor de línea depende del spot size y enfoque determinados, y de todos los parámetros que definen y perfeccionan la calidad del haz de iones.

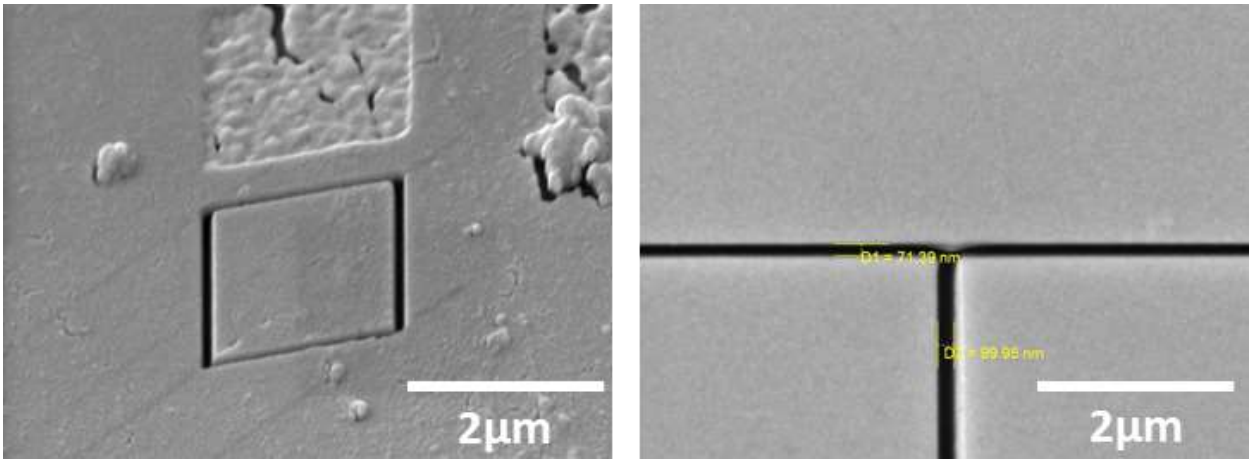

Figura 4.4.1. Imágenes SEM de geometrías erosionadas sobre Au depositado por evaporación térmica.

4.4.2 Determinar condiciones de haz para patrones definidos en el orden de los micrómetros con profundidad nanométrica.

Se grabaron cuadrículas de 2x2 µm área y 150 nm de profundidad aproximadamente. Los resultados se muestran en las siguientes imágenes.

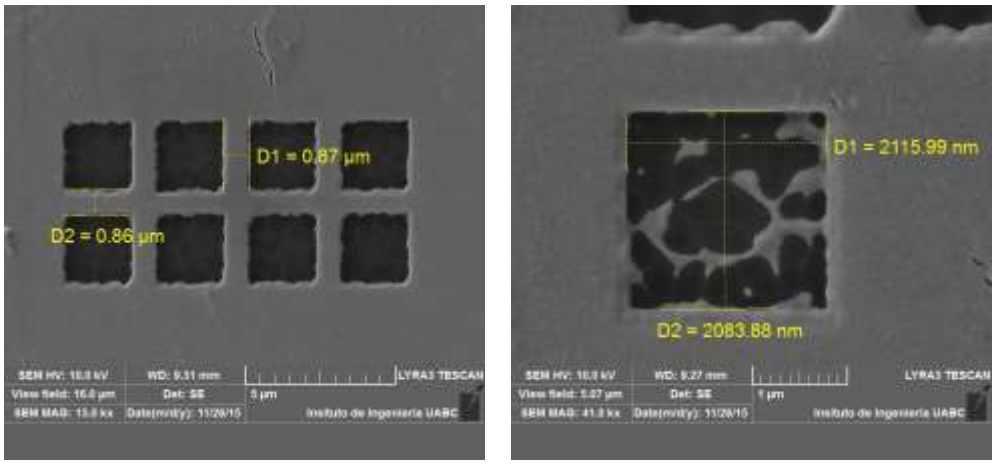

Figura 4.4.2. Imágenes SEM de cuadrículas simples de 2x2 µm con profundad de 150nm.

4.4.3 Uso de máscaras digitales.

Una de las herramientas más útiles para la erosión selectiva de patrones, son las máscaras, estas máscaras permiten o evitan la erosión, grabado o activación de zonas específicas protegiendo el resto de la muestra.

En este experimento se utilizaron mascaras digitales, utilidad de las herramientas “Draw Beam”, llamadas “Void rectangle” o “void poligon”. Con el uso de estas máscaras digitales se evita la erosión del haz de iones sobre diseños ya realizados haciendo las veces de una máscara física.

Se preparó para erosión la muestra M01, en ella se dibujó una sencilla estructura rectangular con la utilidad “Filed rectangle”. Sobre este, se dibujó una máscara concéntrica. Como resultado se obtuvo una estructura de contorno rectangular bien definido.

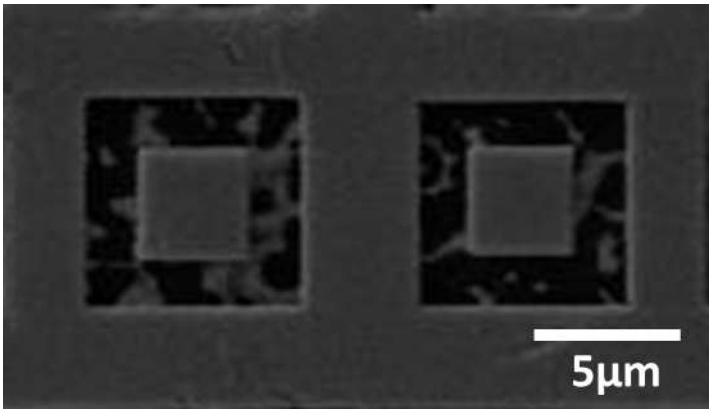

Figura 4.4.3. Máscaras void rectangle

Una vez conseguidos los resultados deseados con una sola mascara, se realizó un diseño de múltiples máscaras. Buscando las mejores condiciones de haz para posterior mente re escalar el diseño y encontrar la mínima resolución posible.

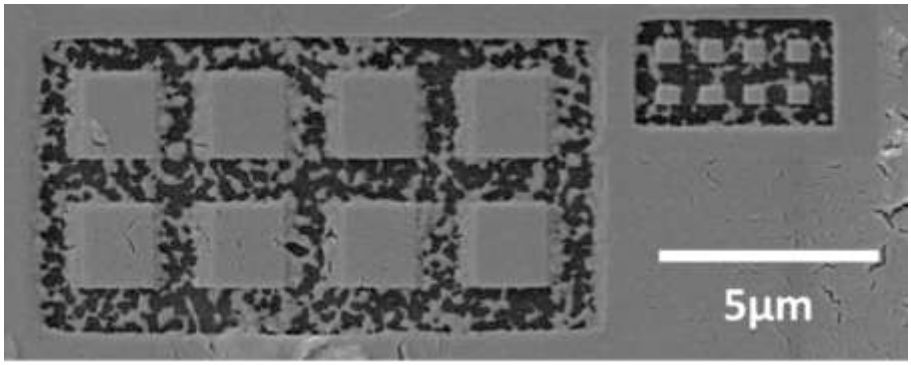

Figura 4.4.4. Imágenes SEM de diseño con múltiples máscaras.

La mínima resolución posible alcanzada se muestra en la figura 4.4.5. Estructuras definidas con características menores a los 100 nm bajo condiciones óptimas de haz.

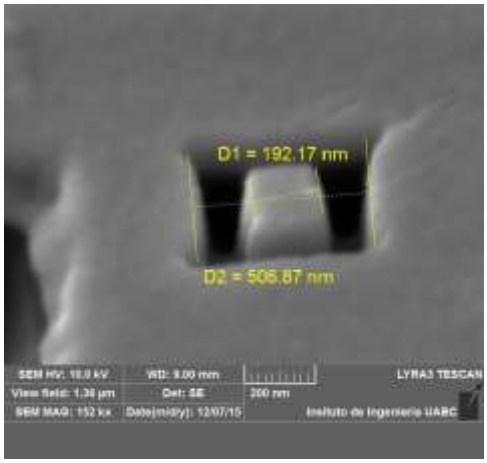

Figura 4.4.5. Mínima estructura permisible sobre Au delgado bajo condiciones estándar de haz de iones.

Como resultado tras la erosión se obtuvo un patrón de cuadrículas dentro de los parámetros preestablecidos (Figura 4.4.6). Estos experimentos permiten conocer las condiciones óptimas del haz de iones para diseños simples y complejos, sin embargo, experimentos de este tipo deben realizarse para cada tipo de muestra ya que las tazas de erosión dependen de la dureza de cada elemento.

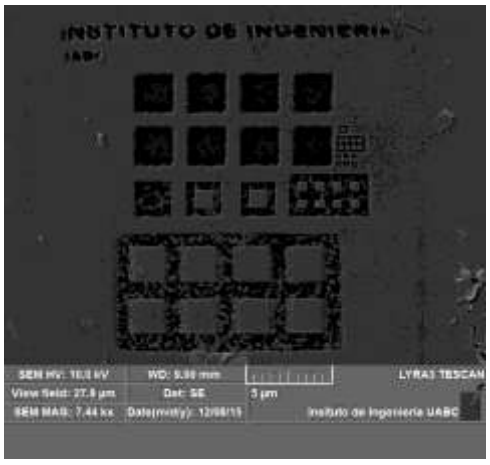

Figura 4.4.6. Perspectiva de todas las cuadrículas con y sin máscara realizadas sobre oro delgado.

4.5 Diseños complejos de erosión y depósito con mapa de bits.

Para diseños rápidos y relativamente sencillos las herramientas de “Draw Beam” son muy útiles, sin embargo, para diseños más complejos existe la opción de exportar diseños desde distintas plataformas en formato de mapa de bits.

Para probar la herramienta “Bit Map” se utilizó el clásico “Paint” de Microsoft, en él se escribió la leyenda “Instituto de Ingeniería UABC” con formato monocromo, misma que fue erosionada sobre la muestra M01. Las dimensiones del diseño una vez grabado sobre la muestra rondaban los 800nm cuadrados.

Figura 4.5.1. Diseño mapa de bits. Imagen SEM. Imagen FIB. Barra de escala de 5 µm sobre las tres imágenes.

4.5.1 BIT MAP Escala de grises.

En este experimento se trabajó con diseños en distintas escalas de grises. Para una escala de grises dada con luminosidad entre 0 y 240, el tiempo de erosión es dividido en 0% para el negro máximo, 100% para el blanco máximo.

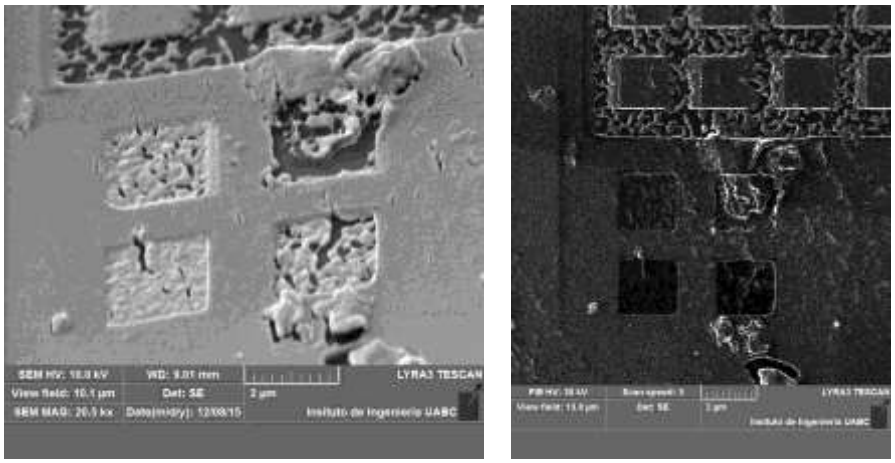

Figura 4.5.2. Imágenes SEM y FIB de erosión por escala de grises.

4.6 Depósitos por del sistema de gases y diseños complejos.

Luego de la experiencia que dejó la experimentación con la erosión y captura de imágenes con distintas configuraciones de haz, se comenzaron las pruebas FIB-SEM y GIS para depósito de materiales.

Se depositó platino por FIB y por SEM en cuadriculas de 1x1 µm y 2 x 2 µm respectivamente. La duración total de ambos depósitos fue de 5 minutos. La corriente de haz de electrones de 0.265 µA fue medida por “Faraday cup”. La corriente de haz de iones se seleccionó por estándar 80pA. Los espesores de los depósitos resultantes se midieron por sección transversal, esta fue realizada por haz de iones dando como resultado un grosor de Pt de140 nm para haz de electrones y 340 nm para haz de iones.

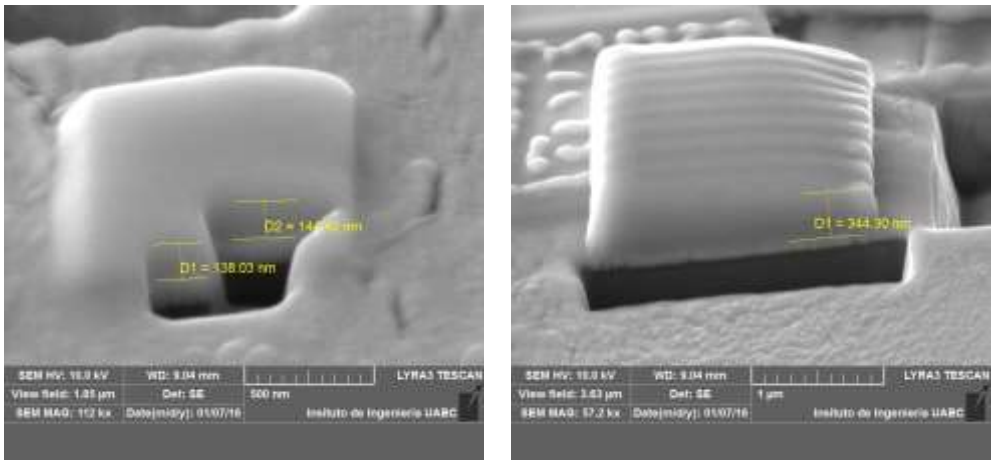

Figura 4.6.1. Imágenes SEM de depósitos de Pt por haz de electrones y de iones.

4.7 Escudo UABC, grabado sobre SiO2 térmico.

En esta etapa de la experimentación se diseñó en “Photoshop” el escudo de la UABC. En formato mapa de bits (.bmp), se hicieron varios diseños buscando la mejor resolución y calidad del diseño (Figura 4.7.1). Cada píxel en la imagen es un punto del haz de iones o electrones. Así, a mayor calidad de imagen, mejor resolución de del haz de iones y/o electrones. Es decir, a mayor cantidad de pixeles, mayor cantidad de puntos de barrido. Sin embargo, esto es inútil si no se adecua el haz correctamente.

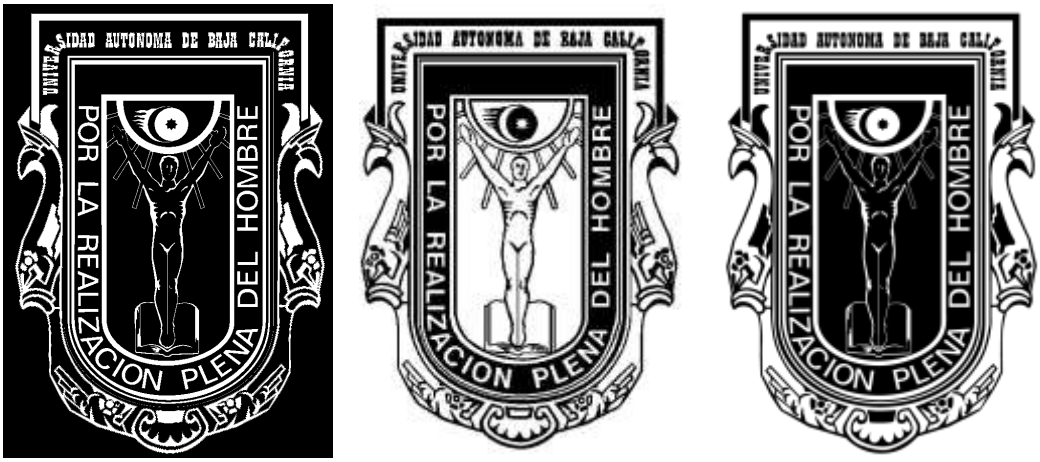

Figura 4.7.1. Distintos diseños formato BMP detallados en “Photoshop”.

Una vez erosionados los diseños, la captura de imagen requiere de ciertas condiciones de haz. Para cualquier caso; SEM o FIB, el ajuste del foco es de primera importancia. Sin embargo, en el caso de imágenes por haz de iones, la velocidad de barrido y la intensidad de haz juegan un papel mucho más importante que en imágenes por electrones ya que el haz de iones erosiona y destruye la muestra con cada barrido. En

esta sección no se detallaran las condiciones del ambos haces. Una comparativa de las imágenes que se obtienen por SEM y FIB bajo condiciones estándar se muestra en la figura 4.7.2.

Figura 4.7.2. Imágenes SEM-FIB. Escudo UABC erosionado sobre oro delgado con platilla BMP.

El escaneo del haz de iones sobre la superficie tiene efecto en la calidad de la erosión y características específicas que fueron examinadas de forma experimental.

5 Resultados experimentales: Nanopartículas metálicas.

En esta sección se abordara la experimentación más avanzada, los resultados de este trabajo fueron publicados en distintas revistas indizadas y arbitradas.

5.1 Obtención de nanopartículas metálicas y bimetálicas de Au, Cu y Au/Cu a partir de películas delgadas.

En esta sección se presenta la experimentación para las capas de metales delgados de Au, Cu y Au / Cu obtenidos por deposición por pulverización catódica en el sistema FIB-SEM. Después de la deposición, las capas se sometieron a recocido térmico rápido en vacío para formar nanopartículas de Au, Cu y Au / Cu. Se estudió el efecto de los iones Ga implantados en sustratos de SiO2 / Si; previo de la deposición de la capa de Au, sobre el tamaño y la morfología de las nanoestructuras obtenidas. Una ventaja de las NP obtenidas por el método propuesto es que no contienen contaminantes de carbono, lo cual es esencial para las aplicaciones en las áreas de plasmónica y metamateriales [22]

5.2 Pulverización catódica de haz de iones focalizados.

La deposición se llevó a cabo en un sistema de doble haz FIB / SEM TESCAN Lyra 3 XMU. El blanco y el sustrato se colocaron a 90 ° entre sí en un soporte metálico en forma de L. El blanco se colocó lo más cerca posible del sustrato. Durante la deposición, la plataforma se inclinó a 55 ° con respecto a su posición horizontal, de modo que el haz de iones de Ga era perpendicular al plano del soporte del blanco y paralelo al sustrato (Figura 5.2.1).

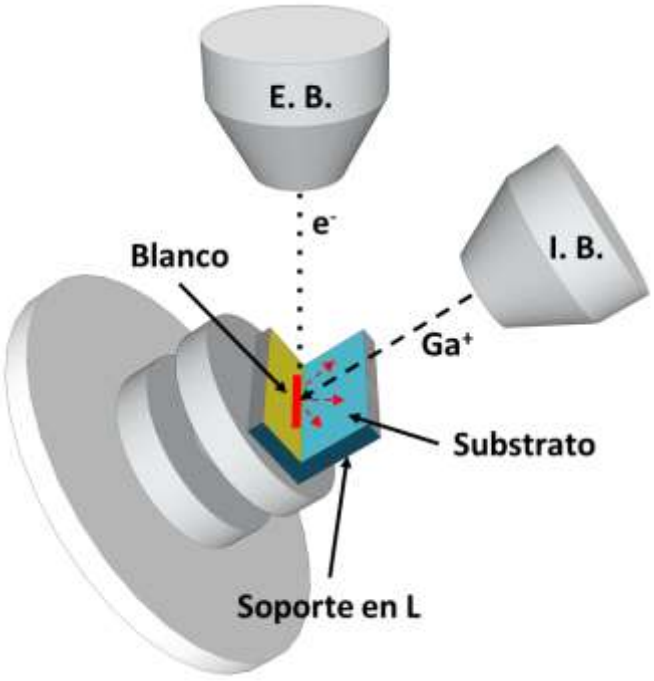

Figura 5.2.1. Representación esquemática del proceso de deposición; E.B. - haz de electrones, I.B. - haz de iones.

Cuarzo y silicio cristalino oxidado térmicamente con 25 nm de SiO2 en la parte superior se utilizaron como sustratos. Se utilizaron filamentos de Au y Cu de alta pureza como blancos. El material a depositar se erosionó de áreas rectangulares con un ancho fijo de 15 µm y una longitud variable (Figura 5.2.2.).

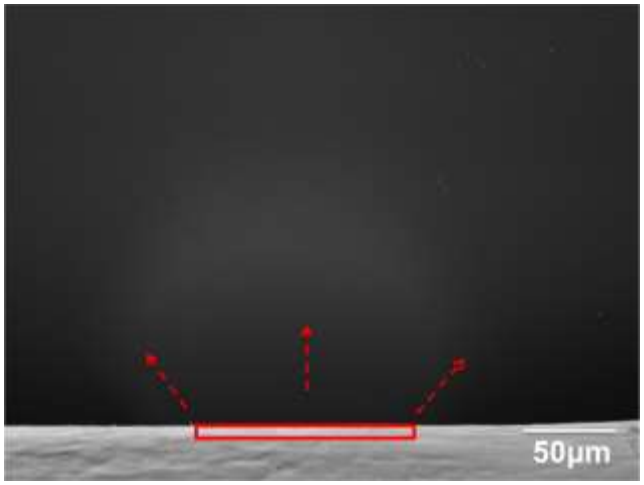

Figura 5.2.2. Silicio cristalino como sustrato y blanco de Cu. El rectángulo en color rojo representa el área rectangular erosionada en blanco de Cu.

El espesor de la película se varió utilizando diferentes tiempos de erosión. El voltaje de aceleración, la corriente del haz y el tamaño del punto focal (spot size) se ajustaron a 30 kV, 1 nA y 50 nm, y la presión de la cámara durante la deposición fue de 3.5 × 10-2 Pa. Para depositar las bicapas de Au / Cu, los blancos de oro y cobre se colocaron uno junto al otro tocándose para ser erosionados consecutivamente y obtener así la superposición de las capas, la erosión se realizó desde áreas orientadas a 35° desde

los bordes del blanco (Figura 5.2.3). Los espesores de la película se determinaron por sección transversal de trincheras realizadas en distintas zonas.

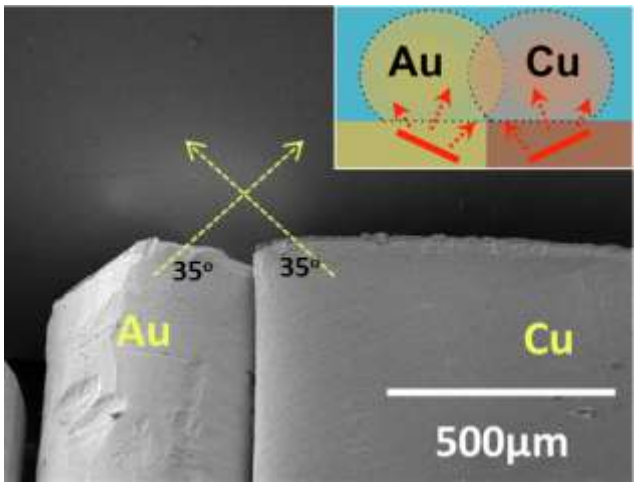

Figura 5.2.3. Imagen SEM y esquema de la configuración de los blancos de Au y Cu para el depósito de bicapa. El inserto en la imagen muestra la zona de superposición de las capas.

Después de la deposición, las capas se sometieron a un recocido térmico al vacío de 6,7 × 10-3 Pa durante 1 o 5 min. El recocido se llevó a cabo utilizando una placa de tungsteno calentada con corriente eléctrica sobre la cual se colocaron las muestras. La temperatura de la placa durante el recocido fue de 1100 ° C.

Los espesores de capa de las muestras de control con metal depositado sobre sustratos de cuarzo por evaporación térmica se midieron con un elipsómetro de ángulo variable J. A. Woollam M-2000. Los espectros de transmisión de las capas en el sustrato de cuarzo se midieron en el rango de 185-1400 nm utilizando el espectrómetro UV-Vis Shimadzu 2600.

La Figura (5.2.4 a) muestra la imagen SEM de la película de Cu depositada sobre el sustrato SiO2 / Si mediante la erosión de un volumen con dimensiones de 60 × 15 × 0,3

µm. Debido a que el objetivo se colocó a 90° respecto al sustrato, el grosor de la película varía en dirección perpendicular al objetivo. También se observa una variación en la dirección paralela al objetivo, en particular en regiones cercanas a los bordes laterales de la película gruesa. El grosor medido a distintas distancias de la trinchera uno (T1), ubicada en el centro de la zona más gruesa de la película, se muestra en la Tabla 5.1. La Figura 5.2.4 b) muestra la morfología de la superficie en T1, donde el grosor de la película es ~ 180 nm. Se observó una morfología granular similar para espesores en el rango de 180-30 nm.

Trinchera	T1	T2	T3	T4	T5	T6
Distancia a T1 (µm)	0	30	60	90	40	50
Espesor (nm)	185	119	50	30	99	90

Tabla 5.1. Espesor de película de Cu depositada por pulverización catódica de haz de iones.

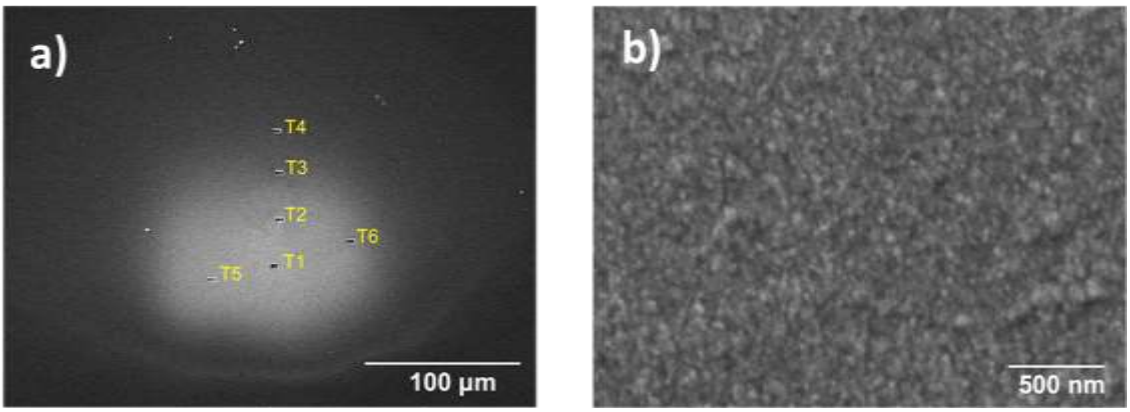

Figura 5.2.4 Vista completa del depósito de Cu con trincheras previas al recocido. b) Alta magnificación de la zona más gruesa del depósito en T1.

5.3 Recocido térmico rápido.

Las películas depositadas se sometieron a recocidos térmicos rápidos (RTA).

El recocido a alta temperatura durante 1 y 5 minutos no modificó la morfología de la película con espesor en el rango mencionado. Sin embargo, en áreas donde el grosor era inferior a 30 nm, la periferia de la imagen en la Figura 5.3.5.

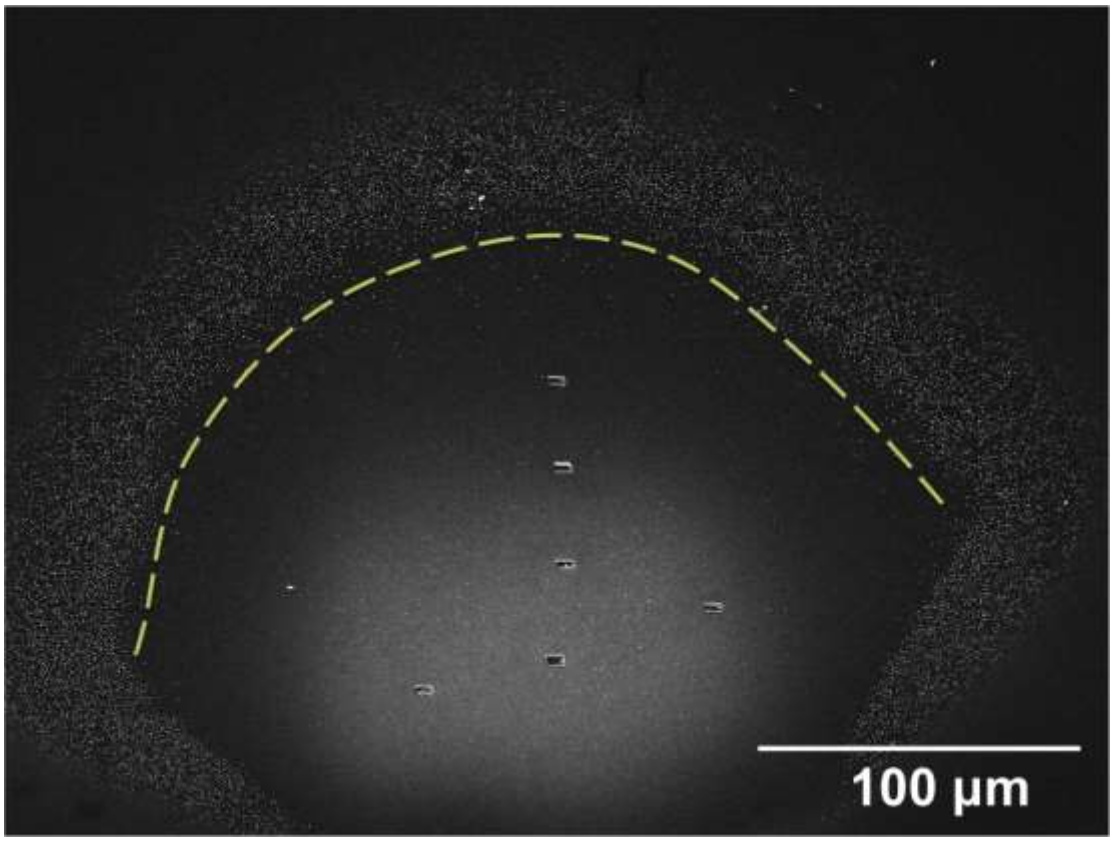

Figura 5.3.1. Imagen SEM de la película de Cu después de un minuto de recocido.

El recocido de 1 min conduce a la formación de nanopartículas con diferentes tamaños y densidad espacial (Figura 5.3.2.)

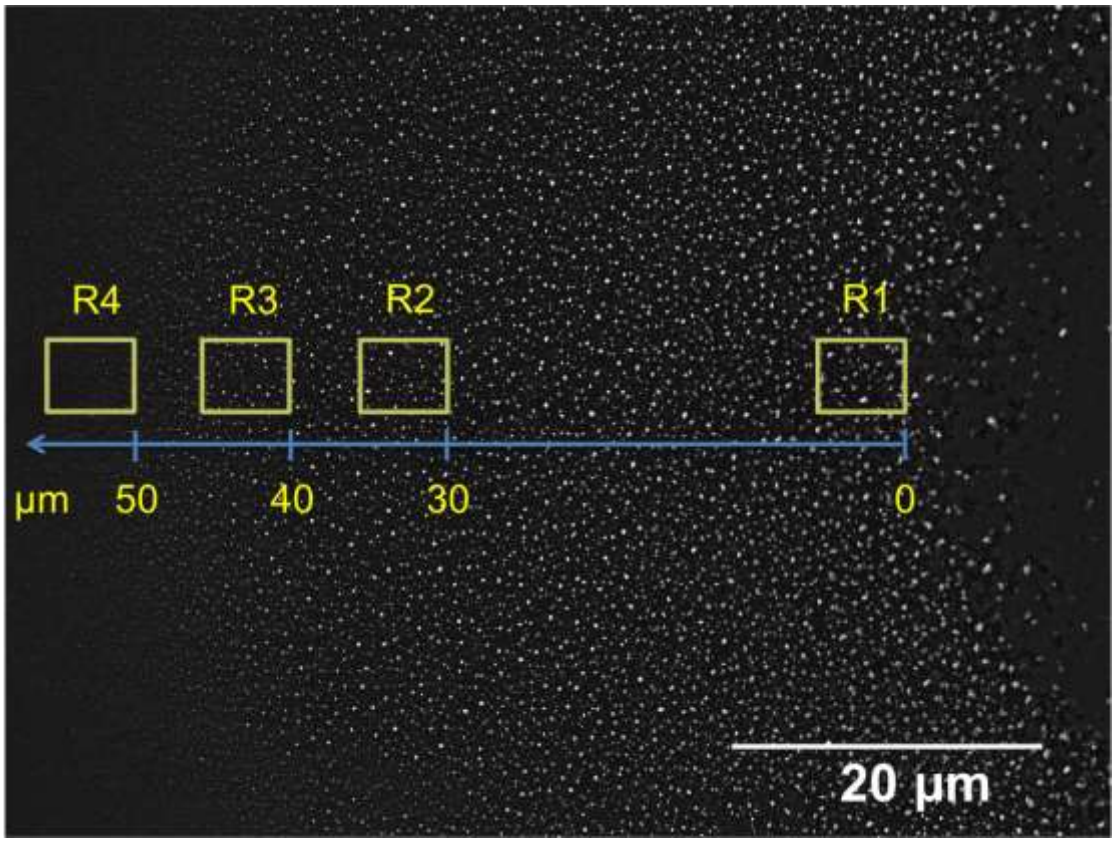

Figura 5.3.2. Partículas de Cu, el tamaño de partícula disminuye en dirección de R4.

Con el aumento de la distancia a R1, el tamaño de los NP formadas disminuye como resultado del menor espesor de la película. La Figura 5.3.3 muestra las nanopartículas formadas a 0, 30, 40, y 50 µm de R1. Las nanopartículas más grandes en estas regiones tienen un tamaño de 400, 200, 150 y 70 nm, respectivamente. Además, las nanopartículas cambian a una forma más redondeada con la disminución de tamaño.

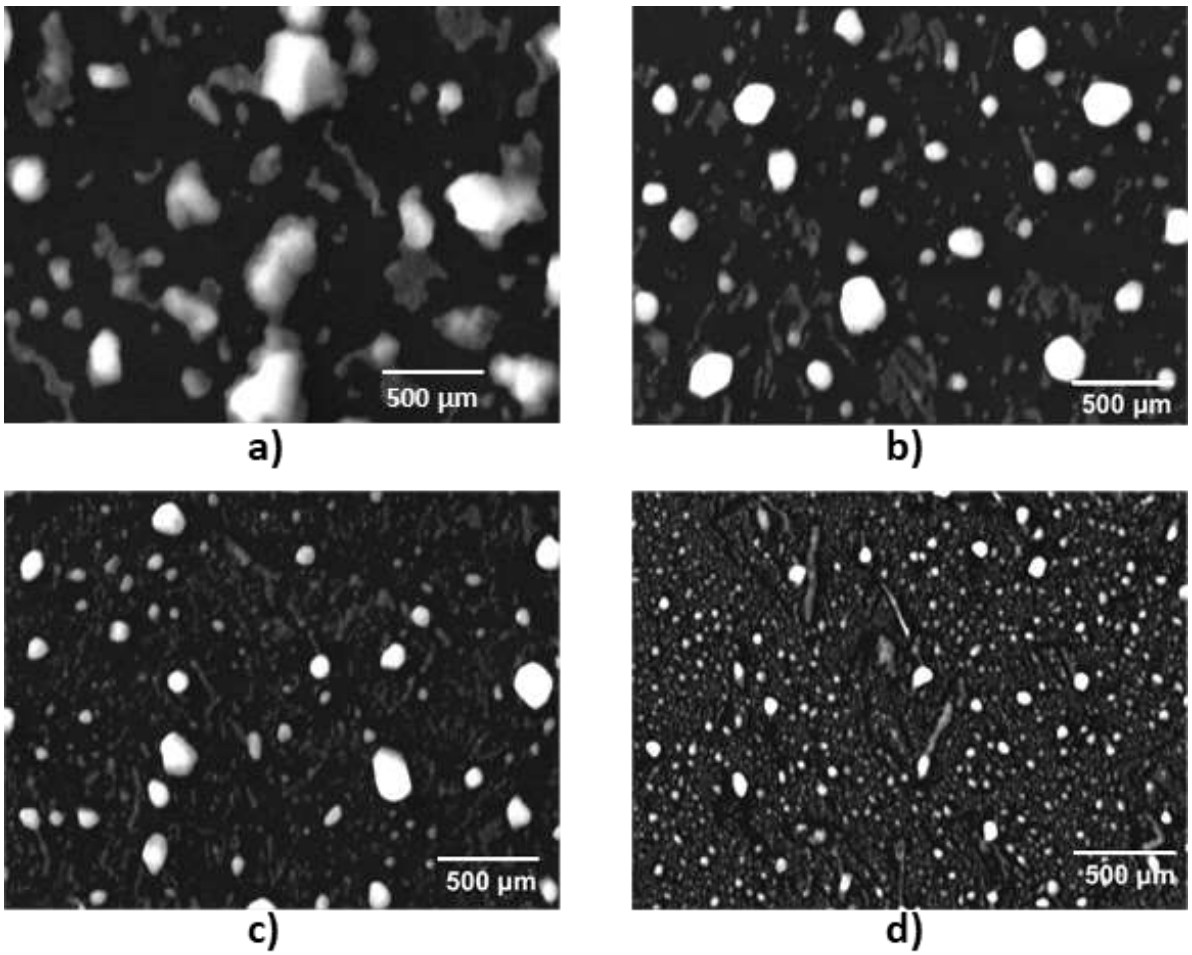

Figura 5.3.3. Nanopartículas en de Cu; obtenidas por SEM a 100kx, en las regiones R1, R2, R3, y R4; a), b), c) y d) respectivamente.

Se obtuvieron resultados similares para las películas de Au depositadas. Como en el caso del recocido a alta temperatura de Cu, no cambió la morfología de la capa gruesa (Figura 5.3.4) y de manera similar lleva a la formación de nanopartículas en la periferia donde el espesor de la capa es <30 nm.

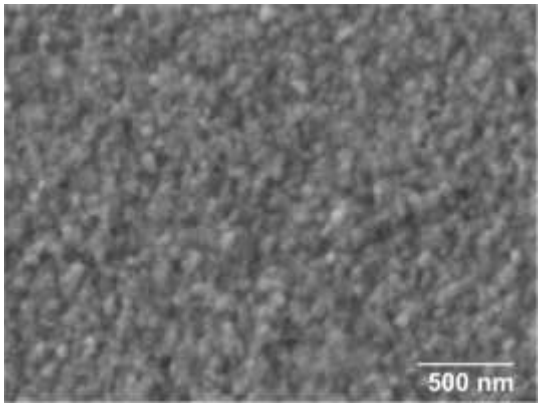

Figura 5.3.4. Imagen SEM en zona gruesa de película de Au recocida.

Se observó una diferencia importante en la región de transición entre la película gruesa y la región de las nanopartículas donde se formaron nanoislas con forma arbitraria (Figura. 5.3.5 a). De manera similar que en la zona R4 de la película de Cu, la Figura 5.1.9 b) muestra nanopartículas a una distancia de 50 μm de la película continua.

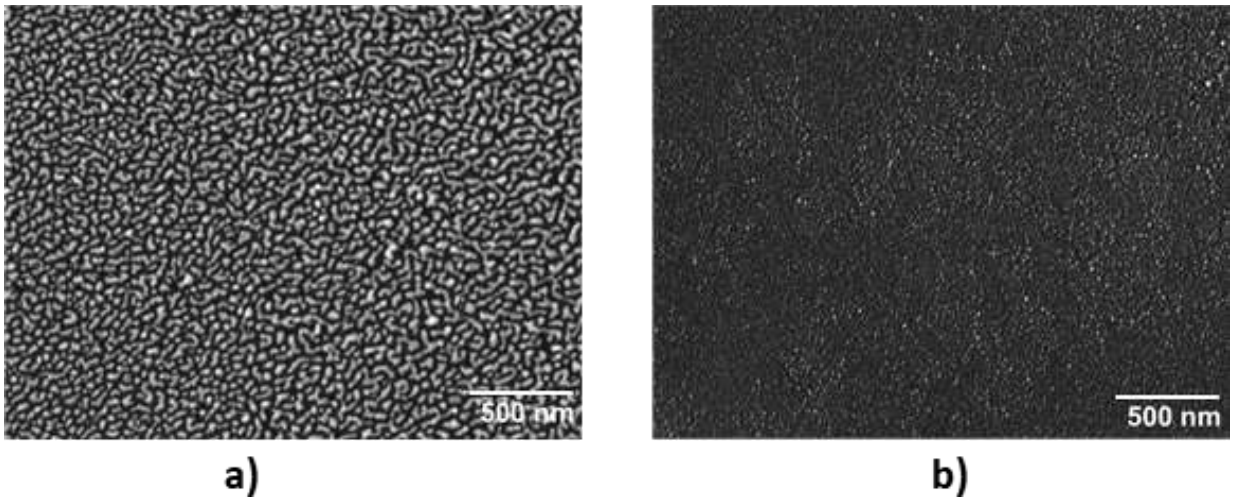

Figura 5.3.5. a) Nanoislas de forma irregular crecidas en la región que comprende la transición película gruesa a delgada <30 nm. b) Nanopartículas formadas a una distancia de 50 μm de las nanoislas.

En contraste, las películas de Au y Cu con un grosor en el centro de ~ 20 nm o menos, obtenidas en tiempos de erosión menores, resultaron sin características superficiales apreciables. El recocido a alta temperatura durante 1 minuto de estas películas de ~ 20 nm de espesor conlleva a la formación de nanopartículas con forma casi esférica y diámetros promedio de ~ 20 ± 2 y ~ 21 ± 2 nm, respectivamente (Figura 5.3.6). Un segundo recocido de 1 minuto no dio como resultado una coalescencia adicional ni un aumento del tamaño promedio de las nanopartículas; únicamente aumentó el número de partículas con forma cercana a una esfera.

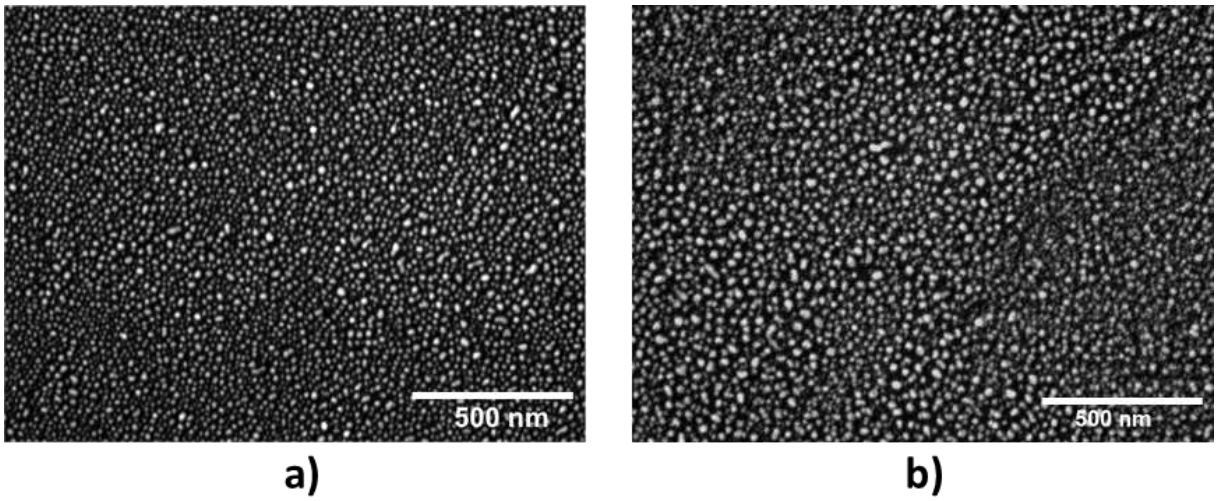

Figura 5.3.6. Imágenes SEM de las películas de ~ 20 nm de Au y Cu recocidas durante 1 minuto. Diametros promedio de; a) 20 nm, b) 21 nm.

La Figura 5.3.7a) muestra imágenes SEM de nanopartículas bimetálicas de Au / Cu obtenidas por 5 min de recocido en bicapas de Au / Cu. El tamaño de nanopartícula varía en un amplio rango, entre 30 y 100 nm. Como se ve en la Figura 5.3.7 b), la espectroscopia de EDS reveló la ausencia de Ga, los únicos elementos detectados en las nanopartículas son Au y Cu. Se detectó mucho residuo de Cu entre las áreas más

alejadas de las nanopartícula, sin embargo, las zonas contiguas se encontraron libres de residuos de ambos metales.

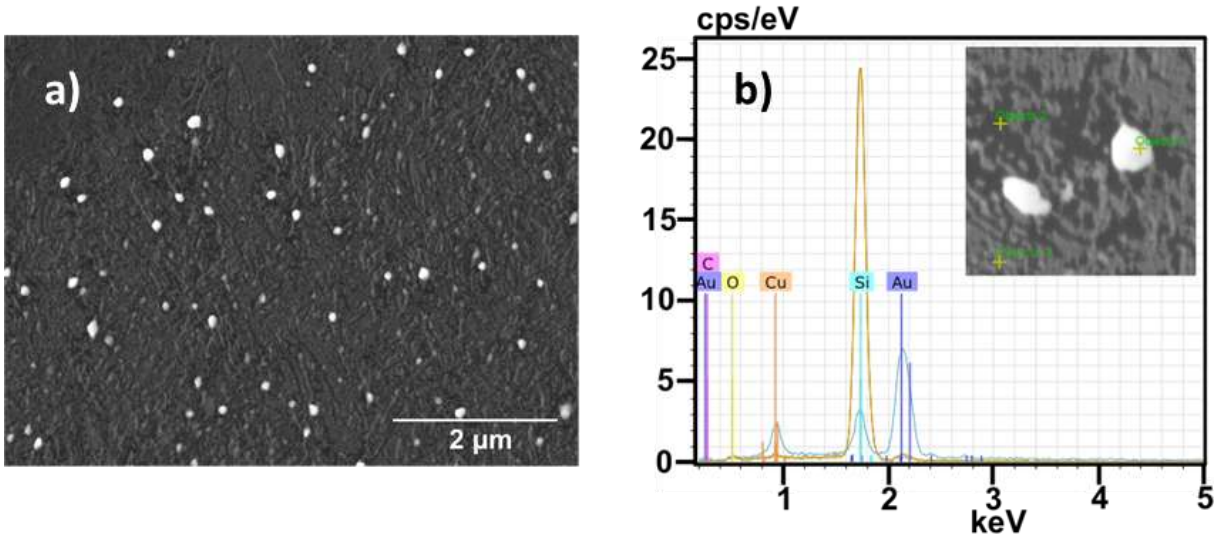

Figura 5.3.7. a) Imágenes SEM de las nanopartículas de Au/Cu obtenidas después de 5 minutos de recocido; b) Espectros EDS de nanopartícula Au/Cu (Objet 1), áreas sin (Objet 2) y con (Objet 3) residuos metálicos

5.4 Efectos de iones de galio implantados por FIB.

El efecto de formación de nanopartículas metálicas de distintos diametros se observó en tanto en áreas con una dosis de implante de Ga muy bajas como altas, por ejemplo en áreas utilizadas solo para enfocar el haz de iones en la superficie se veian afectadas. Este hallazgo nos motivó a estudiar con más detalle el efecto de Ga + implantado en la forma y el tamaño de los nanopartículas formadas después del recocido a alta temperatura.

La Figura 5.4.1 muestra la imagen SEM de una película de Cu recocido. Se distinguen dos regiones con muy pocas nanopartículas. La región 1 está alrededor del SiO2

depositado por haz de iones en una película de Cu no recocida para proteger la superficie metálica antes de fresar una zanja. Sin embargo, en este caso particular no se grabó ninguna trinchera. Aunque el área de deposición se definió como 5 × 1 µm, la región sin nanopartículas es mucho más grande, ~ 9 × 5 µm. El motivo es la deposición de dióxido de silicio fuera del área definida y, como resultado, la capa de Cu se cubrió con SiO2. Esta observación ha sido reportada para coberturas de Pt fuera del área de deposición hasta ~ 2 µm [23]. La región 2, alrededor de una trinchera previa al proceso de recocido. En ella se observan partículas escasamente distribuidas, algunas de ellas con un tamaño mucho mayor que las nanopartículas fuera de la región.

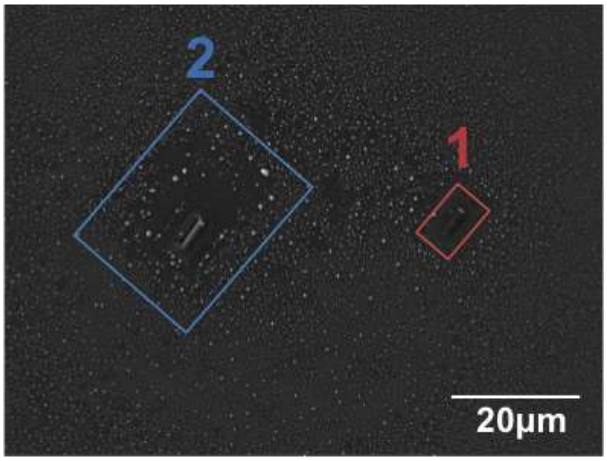

Figura 5.4.1. Imagen SEM de película de Cu recocida con dos regiones de algunas nanopartículas distribuidas en zonas dopadas con Ga.

Los iones Ga se implantaron en sustratos de SiO2 / Si durante 1, 2, 4 y 16 min en el sistema FIB / SEM en las siguientes condiciones: voltaje de aceleración de 30 kV, corriente de iones de 1 pA y área de implantación de 2 × 2 µm. Luego, la película de Au con un espesor de ~ 20 nm se evaporó térmicamente en los sustratos implantados, así

como en una muestra de control de cuarzo. Todas las muestras metalizadas se recocieron durante 1 min (Figura 5.4.3). Se formaron nanopartículas de oro con un diámetro de aproximadamente 20 nm sobre el sustrato de cuarzo (Figura 5.4.2).

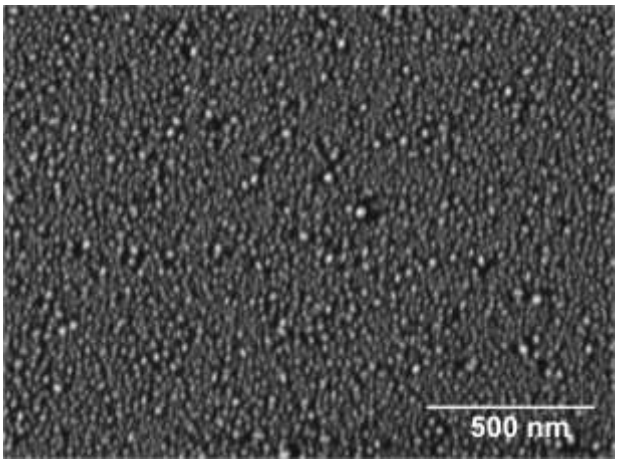

Figura 5.4.2. Nanopartículas obtenidas sobre cuarzo después de la evaporación térmica de ~ 20 nm de Au y 1 minuto de recocido de alta temperatura.

Para todas las muestras implantadas con Ga hay una diferencia significativa en el tamaño de los nanoclusters formados en el área implantada y fuera de ella (Figura 5.4.3). Vale la pena señalar que durante 2 minutos o más el tiempo de implantación, el área implantada se desplaza en la dirección de la conexión a tierra eléctrica debido a la carga de la superficie de SiO2 (Figura 5.4.3. b) - d)). Por este motivo, la dosis total se implantó solo en la región donde las áreas inicial y final se superponen. Se formaron nanoislas con formas irregulares en la superficie de los sustratos implantados de 1 y 2 minutos separados por grandes áreas sin oro o zonas con residuos de Au (Figura 5.4.3. a), b)). Las nanoislas en la muestra de 2 minutos tienen en promedio una longitud y un ancho ligeramente mayores que los de 1 minuto. Las nanopartículas fuera de las

regiones implantadas tienen un tamaño de ~ 20 nm. El aumento adicional del tiempo de implantación a 4 minutos permite la formación de nanopartículas esféricas con diámetros más grandes que en el cuarzo. Fuera de las áreas superpuestas, donde la dosis implantada fue más pequeña, las nanoestructuras en la Figura 5.4.3. c) exhiben una forma similar a las nanoislas en la Figura 5.4.3. a), b). En la superficie de la muestra implantada de 16 minutos, solo se formaron unas pocas nanopartículas con un diámetro mayor que 200 nm (Figura 5.4.3. d).

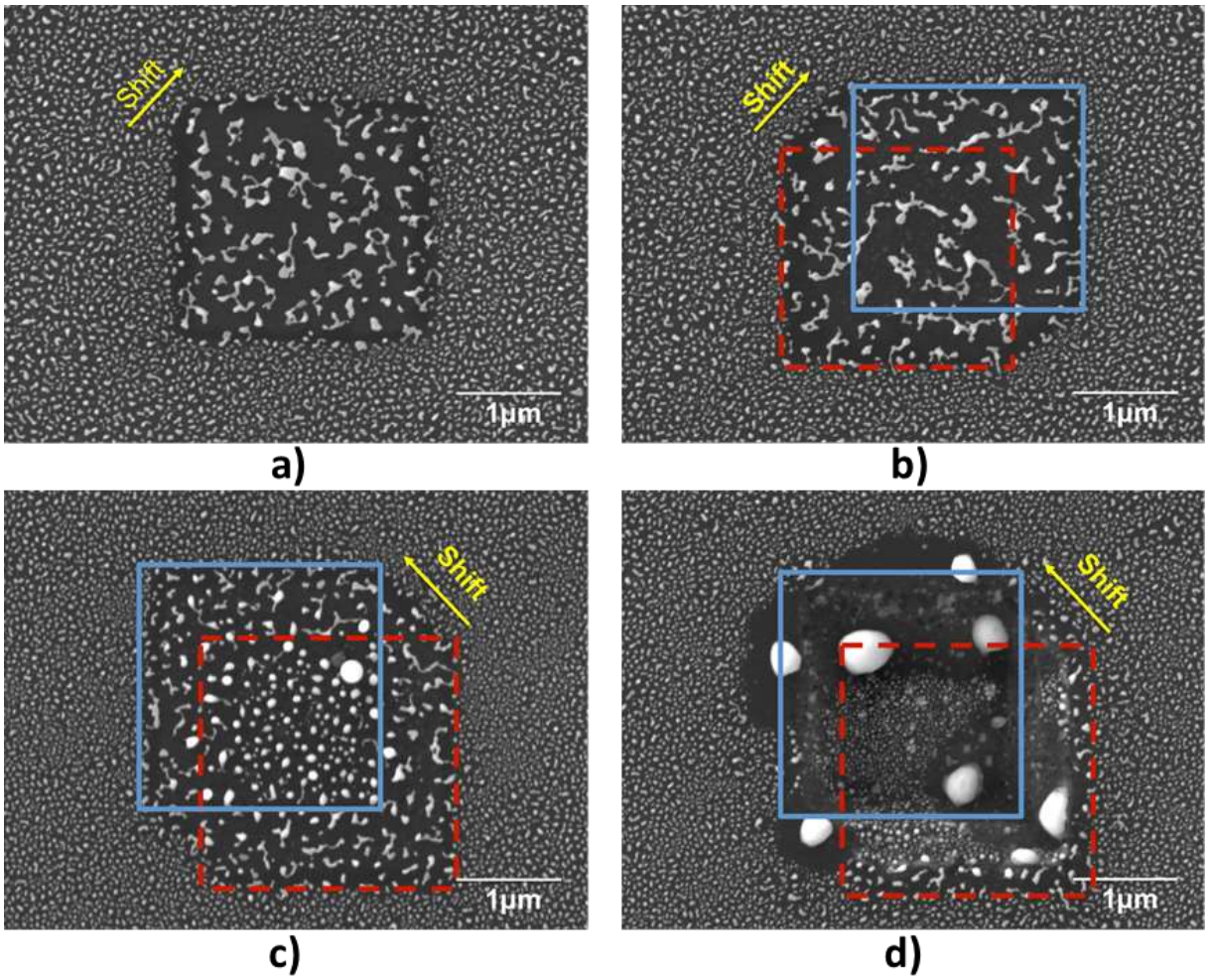

Figura 5.4.3. Imágenes SEM de la película recocida de Au depositada sobre el sustrato SiO2 / Si con implantación de iones Ga durante 1 a), 2 b), 4 c) y 16 d) min. Los cuadros punteados (rojos) y sólidos (azules) muestran el área inicial y final de la implantación; la flecha sólida muestra la dirección de desplazamiento.

Una de las posibles razones del efecto de Ga observado en la formación de nanoestructuras es la disminución de las temperaturas de fusión (Tm) de las aleaciones binarias Au / Ga y Cu / Ga [24, 25]. La reducción de Tm depende del porcentaje de Ga y es más pronunciada para la aleación de Au / Ga. Se puede suponer que para un tiempo de implantación más largo, la concentración de Ga en el metal, resultante de la difusión fuera del sustrato de SiO_2 / Si, es lo suficientemente alta como para mantener el punto de fusión por debajo de la temperatura de la muestra durante todo el proceso de recocido. Por lo tanto, la formación de nanopartículas y la coalescencia se producirían a temperaturas superiores a Tm. El análisis de EDS realizado después del recocido confirmó la presencia de Ga en las muestras con mayores tiempos de implantación. Por ejemplo, la concentración de atómica de Ga fue > 12% en las nanoesferas de Au en la superficie de muestras implantadas de 4 y 16 minutos y menos de 1% atómico en las muestras implantadas durante 1 y 2 minutos. Se ha demostrado que el acercamiento y la coalescencia de las nanopartículas de Au aumentan con la temperatura y que cuando la temperatura de recocido es inferior a Tm, la coalescencia puede propiciar la formación de diferentes formas de nanopartículas, incluido el tipo nanotira [26]. Para probar si la disminución de Tm es el único efecto de Ga en la coalescencia, se llevó a cabo el siguiente experimento. Las muestras sin implantación de Ga y recocidas durante 1 min se recocieron adicionalmente hasta 5 min en pasos consecutivos de 1 min. Algunas muestras se recocieron durante 5 minutos en un solo paso. En ninguno de estos casos se observó una formación de nanoislas similares a los de la Figura 5.4.3. a), b) o nanopartículas grandes como las de la Figura 5.4.3. c), d). Es bien sabido que el Tm de las nanopartículas metálicas es inferior a la de una película delgada del mismo material

[27, 28]. Por lo tanto, se podría esperar que después de 1 minuto de recocido y formación de nanopartículas con un tamaño de ~ 20 nm, los pasos de recocido subsiguientes conducirían a la coalescencia y formación de nanoestructuras más grandes. Sin embargo, esto no se observó, el único cambio fue en la forma de las nanopartículas a formas más esféricas. Los resultados obtenidos indican que el efecto Ga es más complejo que una simple reducción del punto de fusión de una aleación homogénea de Au / Ga. Se ha demostrado que la deposición de Ga por crecimiento epitaxial por haces moleculares (MBE) lleva a la formación de nanopartículas aisladas de Ga [29, 30, 31] ya que el Ga no humecta fácilmente la superficie el SiO_2 [32]. Se puede suponer que una alta concentración de Ga en una región cercana a la interfaz Au / SiO_2, debido a la difusión de iones de Ga del óxido a Au, modifica la superficie y las energías de la interfaz metal / SiO2, lo que promueve condiciones más favorables para la coalescencia de las nanopartículas. La temperatura de fusión más baja puede llevar a una mayor movilidad de las nanopartículas. Después de algunas mejoras de optimización, el efecto observado de Ga en la formación de nanoestructuras puede usarse para definir patrones adecuados para aplicaciones en nanodispositivos.

La Figura 5.4.4 muestra espectros UV-Vis de aproximadamente 20 nm de capa de oro evaporada térmicamente sobre sustrato de cuarzo sin recocido y de capas recocidas durante 1 y 3 min (en tres pasos consecutivos de 1 min). Las muestras recocidas muestran picos a 557 y 535 nm debido a la resonancia de plasmón de superficie localizada (LPSR) en nanopartículas de Au. El pico máximo se desplaza hacia longitudes de onda más cortas con el aumento del tiempo de recocido porque las nanopartículas cambian a una forma más esférica [33], según lo confirmado por SEM. La posición del máximo de LSPR a 535 nm está ligeramente desplazada hacia el rojo

en comparación con el pico de LSPR de nanopartículas de oro de 18 ± 2 nm reportado en [34] muy probablemente porque las NP obtenidas en este trabajo tienen un tamaño promedio mayor y la constante dieléctrica del entorno circundante diferente.

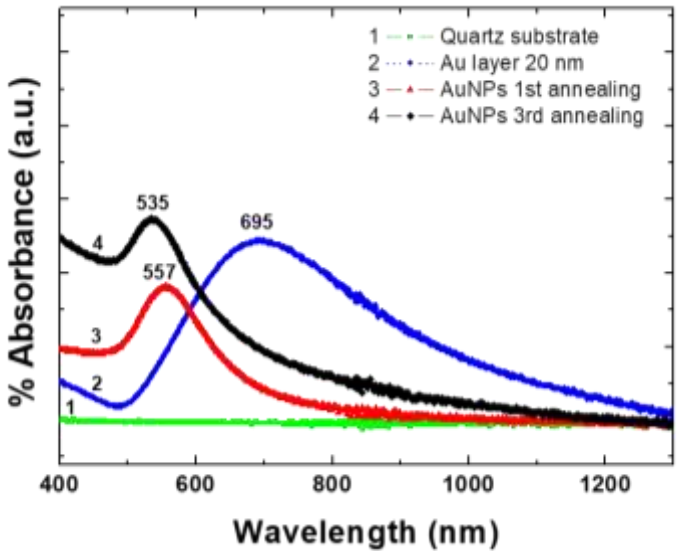

Figura 5.4.4. Espectros UV – Vis de muestra de Au en sustrato de cuarzo: curva 2–20 nm capa de Au sin recocido; Curvas 3 y 4: capas de Au recocidas durante 1 y 3 minutos, respectivamente. También se muestra la absorbancia del sustrato de cuarzo (curva 1).

6 Resultados experimentales: nanotubos de TiO2.

Los nanotubos de dióxido de titanio (TiO2) crecidos en lámina de Ti tienen un área de superficie específica alta, buena capacidad de intercambio iónico y propiedades fotocatalíticas. Por lo tanto, se muy investigados para varias aplicaciones potenciales como catalizadores, generadores de hidrógeno, materiales resistentes a la corrosión y electrocromáticos, en celdas solares, etc. [35, 36, 37, 38, 39, 40, 41]. Los nanotubos en aleaciones de Ti, como Ti6Al4V, Ti6Al7Nb, también han atraído mucho atención para su aplicación en el campo biomédico [42, 43, 44, 45, 46].

La formación de capas de anatasa y rutilo de TiO2 en la superficie Ti6Al4V también se ha informado sobre el tratamiento de oxidación térmica a temperaturas superiores a 200 ° C y 400 ° C, respectivamente [47].

Los materiales nanoestructurados de TiO2 sin dopar y dopados atraen mucha atención como materiales prometedores para aplicaciones de sensores. Se ha demostrado que las estructuras de TiO2 cuasi unidimensionales con su gran área de superficie y alta porosidad tienen un mejor rendimiento de detección de gases en comparación con los densos agregados de nanopartículas [48] y las capas de TiO2 NT se estudian activamente para la fabricación de sensores químicos [48, 49]. Los cambios de resistencia [48, 49, 50, 51] han sido en su mayoría.

6.1 Análisis químico y morfológico

La morfología de las superficies de la muestra se analizó mediante microscopía electrónica de barrido. La composición elemental de los nanotubos se determinó mediante espectroscopia de rayos X de energía dispersiva (EDS). Para eliminar la contribución de Al y V del sustrato Ti6Al4V, los nanotubos se desprendieron del sustrato utilizando cinta adhesiva y se colocaron en cinta de carbono y cobre. La lámina de cobre garantiza que no se incluya ninguna contribución del Al del porta muestras del microscopio en los espectros adquiridos. Se obtuvieron valores similares de concentración de Al en ambos tipos de mediciones.

En la Figura 6.1.1 se muestran micrografías SEM de la superficie de cuatro muestras y las secciones transversales de estas. Las imágenes revelan la presencia de matrices de nanotubos uniformemente distribuidos sobre el sustrato. Los valores promedio de diámetro interno, longitud y espesor de pared de los cuatro tipos de nanotubos se dan en la Tabla 6.1.

Muestra	Diámetro [nm]	Longitud [nm]	Espesor de pared [nm]
1	60	338	8-9
2	65	481	8-12.5
3	80	373	10-13
4	120	497	12-14.5

Tabla 6.1. Promedio de diámetro, longitud y espesor de nanotubos

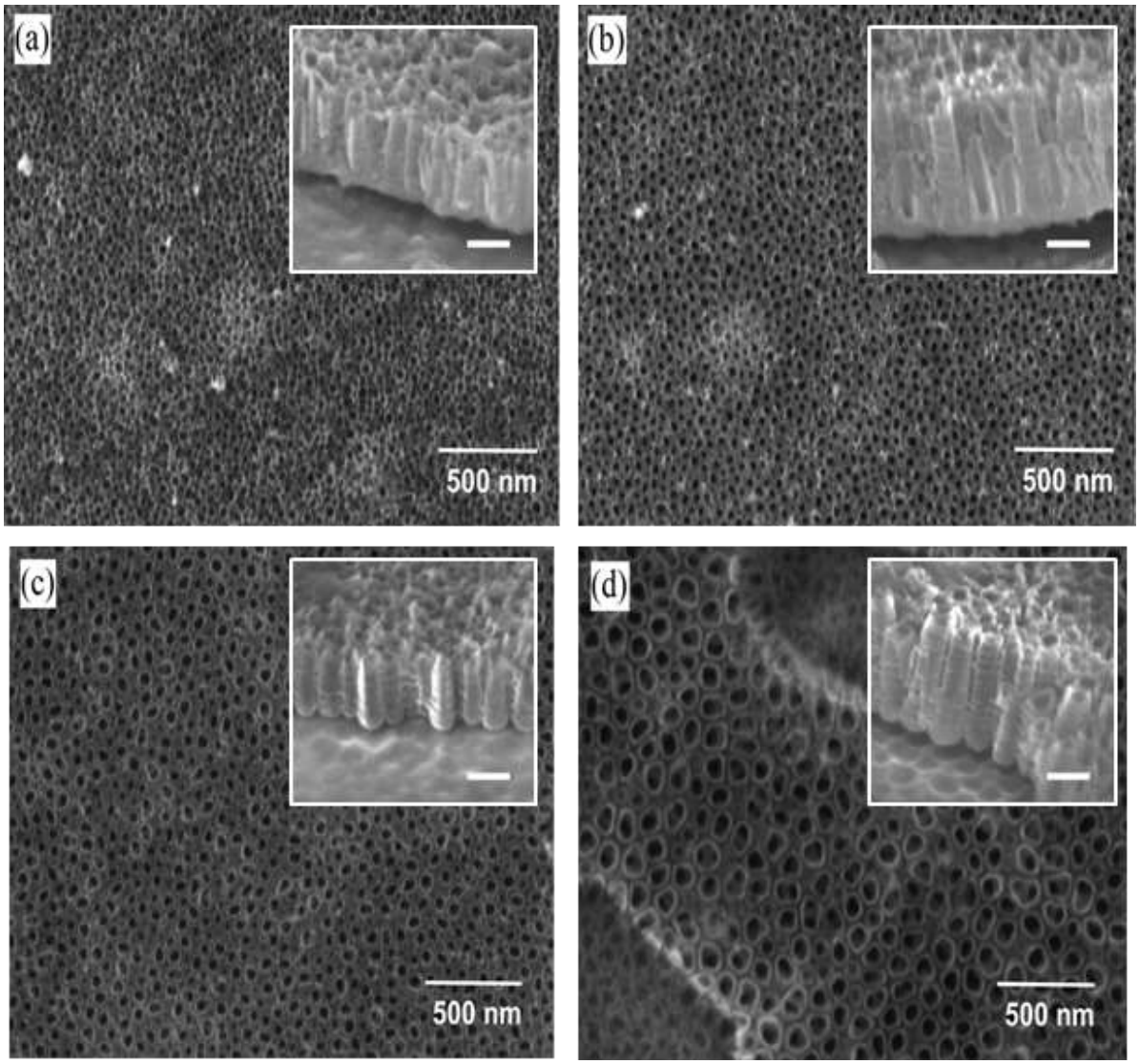

Figura 6.1.1. Imágenes SEM de superficiales de los 4 tipos de muestras de nanotubos de TiO_2, insertado en las imágenes la correspondiente vista transversal con escala de 200 nm.

Los espectros EDS se tomados en todos los tipos de nanotubos en cinta de carbono. Se observaron picos que indican la presencia de Ti, O, Al, C y Si, mientras que no se detectó vanadio (Figura 6.1.2). Las concentraciones obtenidas en porcentaje en peso se dan en la Tabla 6.2. No se observan variaciones sustanciales de la concentración de Al en los nanotubos crecidos en diferentes condiciones de anodización. Las señales de C y Si en el espectro resultaron de la cinta de carbono.

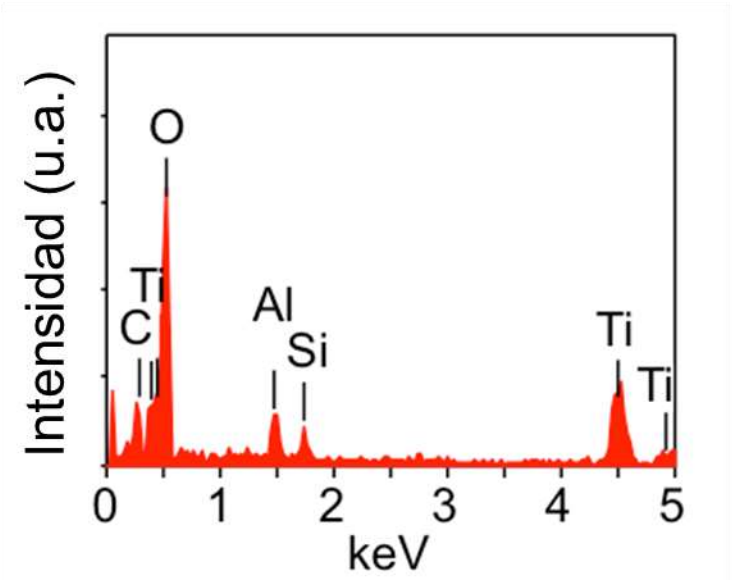

Figura 6.1.2. Espectro EDS de nanotubos de TiO_2 sobre cinta de carbono.

Muestra	NT diámetro	Ti	O	Al	C	Si
1	60	48.5	38.8	1.9	10.5	0.3
2	65	49.4	32.2	3.3	14.4	0.7
3	80	48	39	3	8	1.6
4	120	47.6	38.4	1.9	11.5	0.6

Tabla 6.2. Tabla de concentración de distintos elementos.

La Figura 6.1.4 muestra el cambio relativo del coeficiente de reflexión para muestras de TiO2 NT recocidas a 450 ° C durante 2 h en aire en función del diámetro de los nanotubos para la exposición a vapores de etanol. Una comparación con la Figura 6.1.3 indica que: (i) la sensibilidad de las muestras recocidas con un diámetro de 60 nm y 65 nm es significativamente menor que la sensitividad de las recosidas y (ii) una dependencia del tamaño con la sensitividad también se observa, pero es opuesta a la observada en la Figura 6.1.3 para las muestras recocidas. Dado que los resultados de SEM no mostraron un deterioro apreciable de la calidad del nanotubo por el recocido, se puede esperar que la superficie real de los nanotubos no haya cambiado de manera significativa.

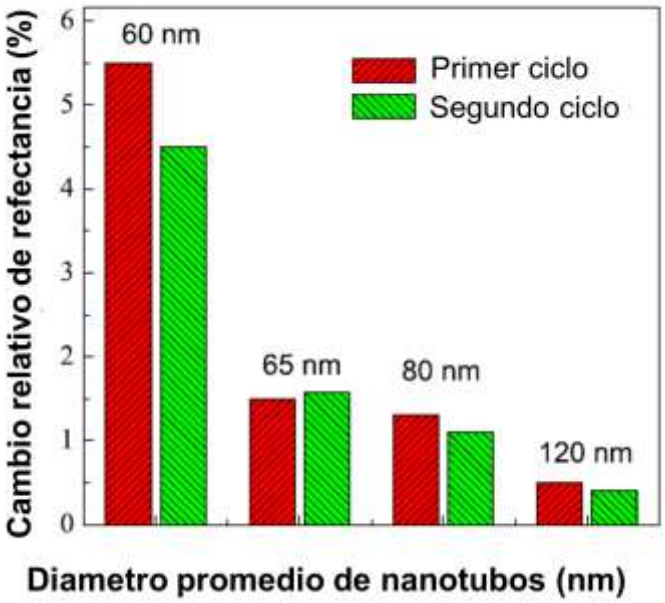

Figura 6.1.3. Cambio relativo del coeficiente de reflexión en nanotubos de TiO2 amorfos en función diámetro de tubo en dos ciclos de exposición a etanol.

La dependencia del tamaño que se ve en la Figura 6.1.4, es decir, la mayor sensitividad de las muestras con NT de diámetros más grandes, puede relacionarse con el aumento observado de la cantidad y / o la cristalinidad de la fase de anatasa con el aumento del diámetro de NT. La disminución de la sensitividad de los nanotubos con un diámetro de 60 nm y 65 nm inducida por el recocido podría ser la consecuencia de la formación de vacancias de oxígeno y otros cambios de composición en la superficie de los nanotubos que tienen lugar en el recocido debido a la presencia de átomos de aluminio incorporados del sustrato.

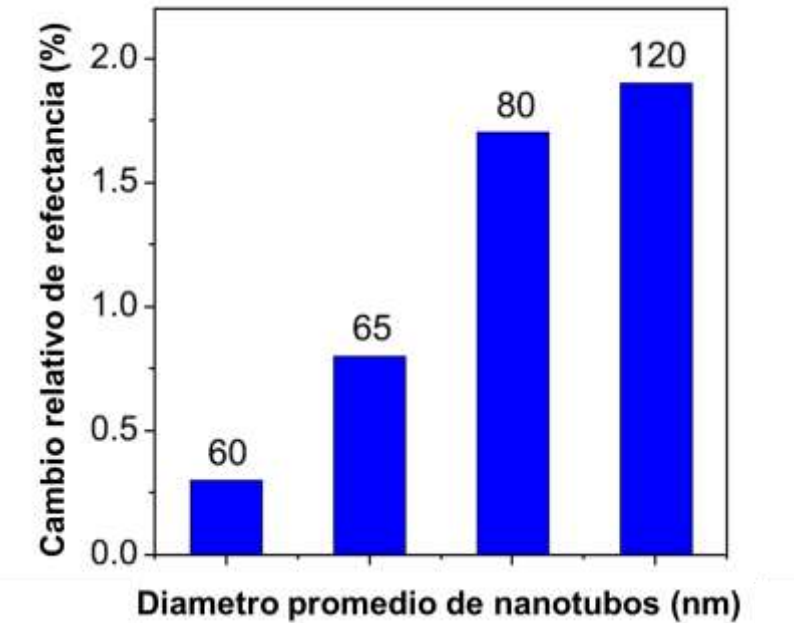

Figura 6.1.4. Cambio relativo del coeficiente de reflexión en nanotubos de TiO2 recocidos a 450^{o} C durante 2 hrs. en función diámetro de tubo en un ciclo de exposición a etanol.

6.2 Caracterización estructural y óptica de nanotubos de TiO_2 alineados verticalmente para implementación en minería de datos.

Los nanotubos de TiO_2 alineados verticalmente han sido muy investigados en ciencia de los materiales. Debido a sus propiedades se utilizan en Aplicaciones biomédicas, fotoquímicas, eléctricas y ambientales. [52]. Las propiedades de estos nanotubos dependen en gran medida de su morfología, por ejemplo, los diámetros (interno y externo) Tiene un gran efecto sobre las propiedades físicas así como su longitud. Por esta razón, deben medirse con precisión [53].

6.2.1 Caracterización estructural por FIB – SEM.

La caracterización de 20 muestras de nanotubos de TiO_2 se realizó para obtener sus características principales como lo son: diámetro interno y externo, longitud de tubo y densidad de tubos.

Todas las muestras se analizaron por SEM y sus diámetros externos fueron medidos como se muestra en la Figura 6.2.1.

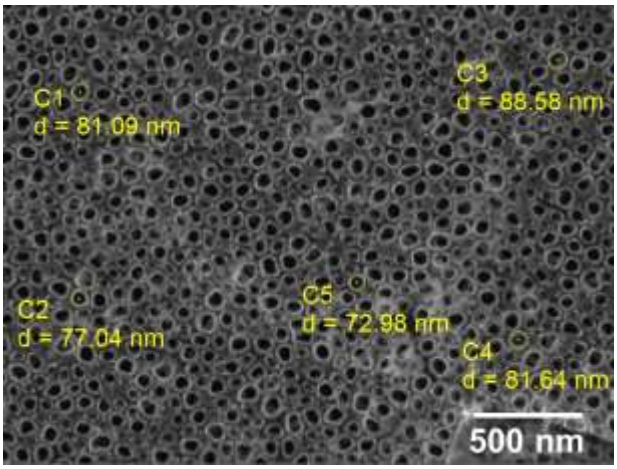

Figura 6.2.1. Medición de diámetros internos de nanotubos de TiO_2.

Mediciones de longitud de tubo se llevaron a cabo por medio de medición de sección transversal. Estas secciones se obtuvieron por medio de trincheras de corte FIB. Dicha trinchera se realizó posterior a la protección de la superficie de tubos, para esto se depositó una capa de ~400 nm. Imagen completa de trinchera y medición de sección transversal se muestran en la Figura 6.2.2.

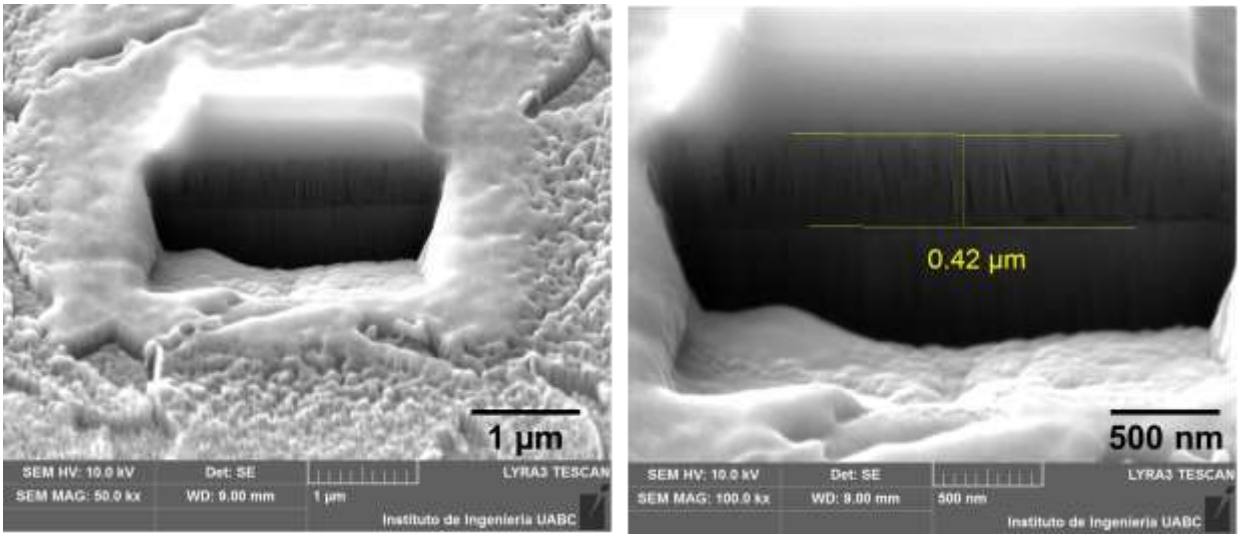

Figura 6.2.2. Imagen SEM de vista completa de trinchera sobre nanotubos de TiO_2 (izquierda) y medición de longitud de tubo de la misma (derecha).

6.2.2 Caracterización óptica por elipsometría de ángulo variable.

Se tomaron espectros de las muestras de nanotubos de TiO_2 por elipsometría de ángulo variable, esta técnica no es idealmente usada en este tipo de mediciones ya que no existen librerías apara materiales de este tipo, y se especializa en películas continuas y delgadas. Sin embargo los resultados fueron requeridos y usados en análisis de minería de datos para la estimación de características de tubo, en este caso diámetro externo.

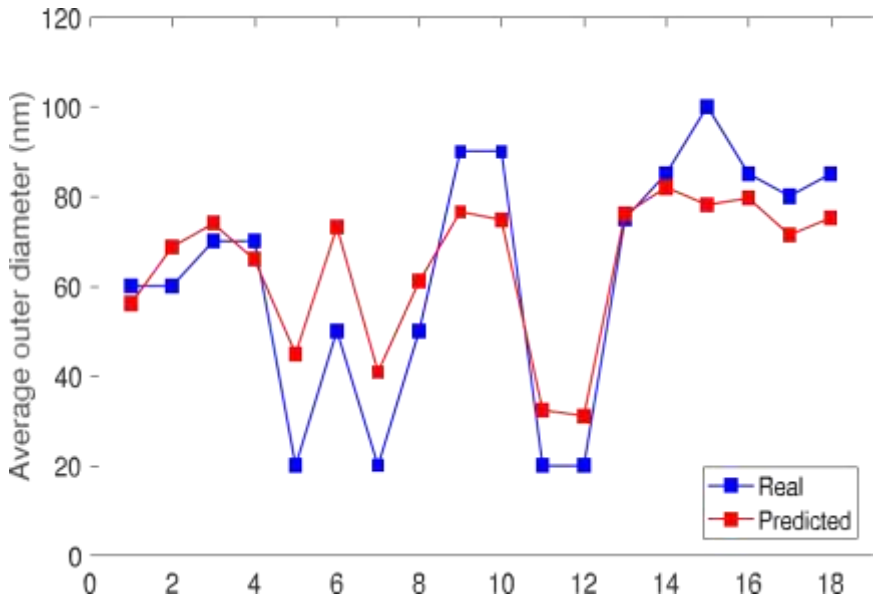

Figura 6.2.3. Grafica comparativa de diámetro promedio real vs calculado (algoritmo KNN).

La Figura 6.2.3 muestra una comparativa entre resultados de medición de diámetro externo promedio por SEM (Real) y calculados (Predicted) por el método de KNN (Vecinos cercanos K) del que no se hablará aquí, sin embargo la información a detalle fue publicada [54].

Los datos obtenidos por elipsometría de ángulo variable Psi y Delta se tomaron a 45, 55, 65, y 75 grados en un rango espectral de 245 – 1000 nm de longitud de onda.

7 Resultados experimentales: Películas delgadas de SiOx.

Las películas de SiOx utilizadas en este estudio se depositaron mediante evaporación térmica de SiO en vacío sobre sustratos de c-Si, seguido de tratamientos de recocido a diferentes condiciones. Las películas de SiOx depositadas tienen x = 1.15 y un espesor de ~ 50 nm. Se produjeron tres grupos de estructuras: recocido a 250 ° C durante 30 minutos en argon para estabilización de SiOx (muestras de control); 700 ° C y 1000 ° C durante 60 min en N2 para la formación de nanoclusters de Si amorfos y cristalinos. Las películas se metalizaron y se micromaquinaron (se formaron trincheras rectangulares alrededor de los dos contactos) a través del sistema FIB para seleccionar el área activa de las películas que contribuirá a la corriente fotovoltaica medida vs voltaje aplicado.

7.1 Deposición de contactos y micromaquinado.

Se realizaron pruebas de FIB para aislar la zona activa (corral), esto con el objetivo de conocer los parámetros de erosión adecuados para la muestra. En la Figura 7.1.1 se muestran corrales erosionados con el parámetro de erosión 1 (los parámetros estándar pueden verse en la Tabla 4.1)

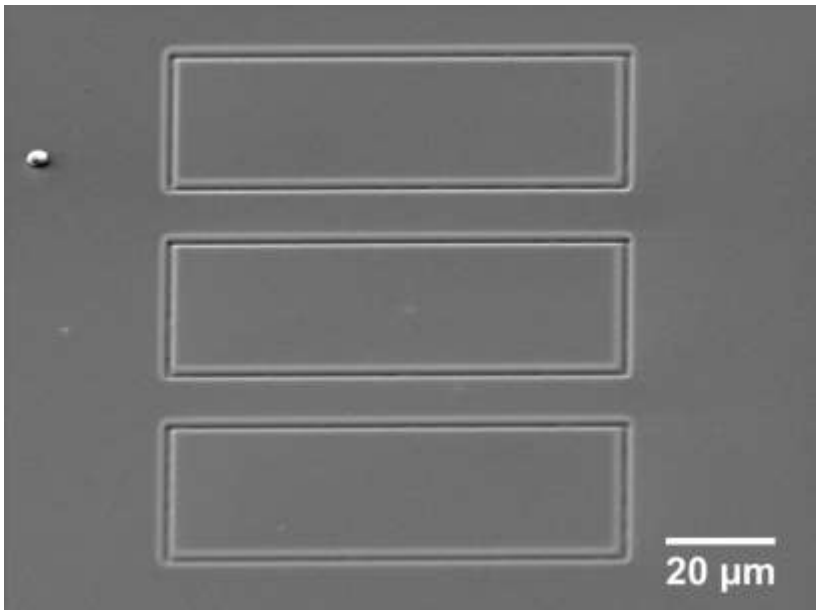

Figura 7.1.1. Imagen SEM de corrales de prueba erosionados sobre muestras de c-Si.

Una vez concluidas las pruebas de erosión, se depositaron contactos de Pt en las zonas activas seleccionadas de cada muestra. Los contactos metálicos de 50 x 50 µm se depositaron primero mediante un haz de electrones seguido de un depósito de iones hasta alcanzar 100 nm de espesor de Pt. Se delimitaron corrales para contactos adyacentes a distancias de 50 µm (Figura 7.1.2. a), b), c)) y 200 µm (Figura 7.1.2. d), e), f)). Los corrales con aproximadamente 1 µm de ancho de línea, se erosionaron a distancia de los contactos de Pt (entre 5 y 15 µm).

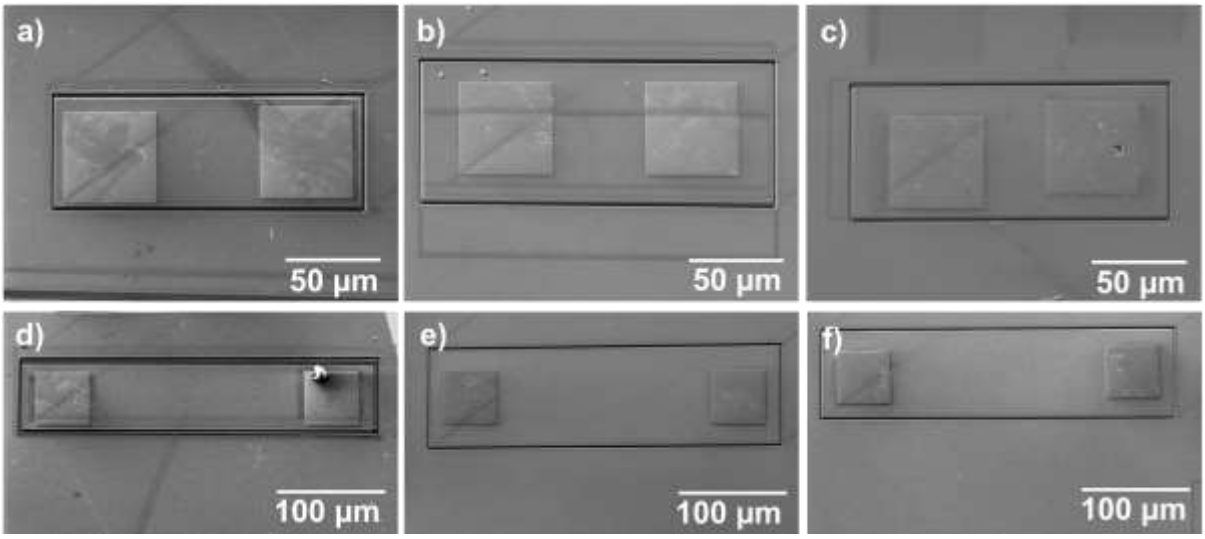

Figura 7.1.2. Corrales en muestras recocidas a 250°, 700° y 1000° C, y contactos de Pt a 50 µm a), b), c) y 200 µm de distancia d), e), f).

7.2 Caracterización eléctrica.

Todas las muestras fueron caracterizadas eléctricamente a distintas longitudes de onda con lámparas LED (IR, rojo, verde, azul, UV) y en obscuridad. Las mediciones obtenidas de corriente vs voltaje (I-V) muestran foto-respuesta solo para luz UV.

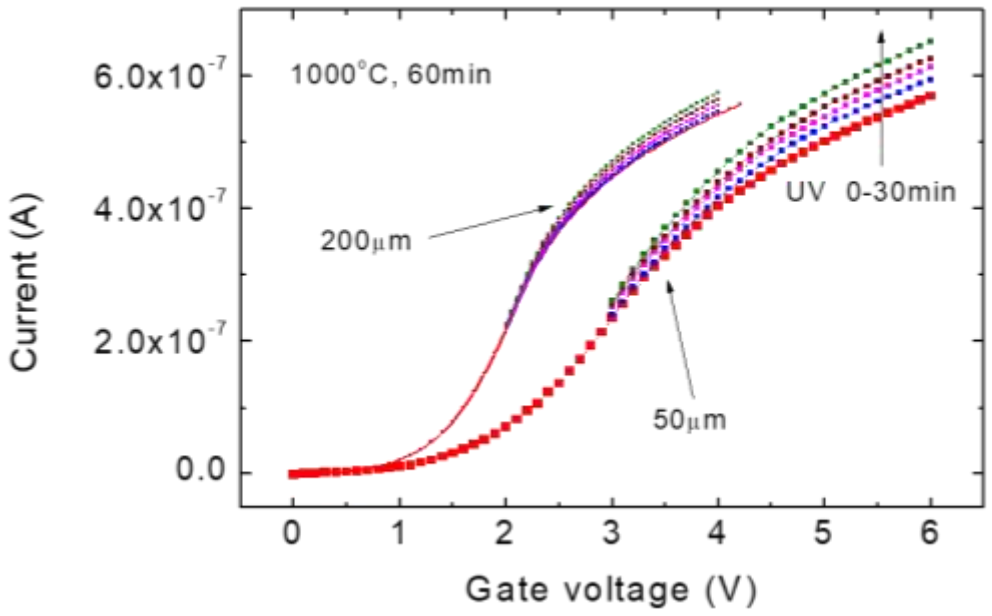

Figura 7.2.1. La gráfica muestra las curvas obtenidas bajo iluminación UV durante 5, 10, 15 y 30 min para muestra recocida a 1000°C en contactos distanciados 50 μm y 200 μm.

La Figura 7.2.1 muestra la respuesta I-V obtenida bajo iluminación UV en muestras de 1000 ° C con canales de 50 y 200 µm. Se detectaron fotocorrientes más grandes en la muestra de canal de 50 µm. Después de la medición en oscuridad, la respuesta UV se obtuvo mediante mediciones I-V con iluminación UV durante 5, 10, 15 y 30 min. La Figura 7.2.2 muestra la respuesta UV relativa ($\Delta I / I_0$) de las muestras de canal corto y largo.

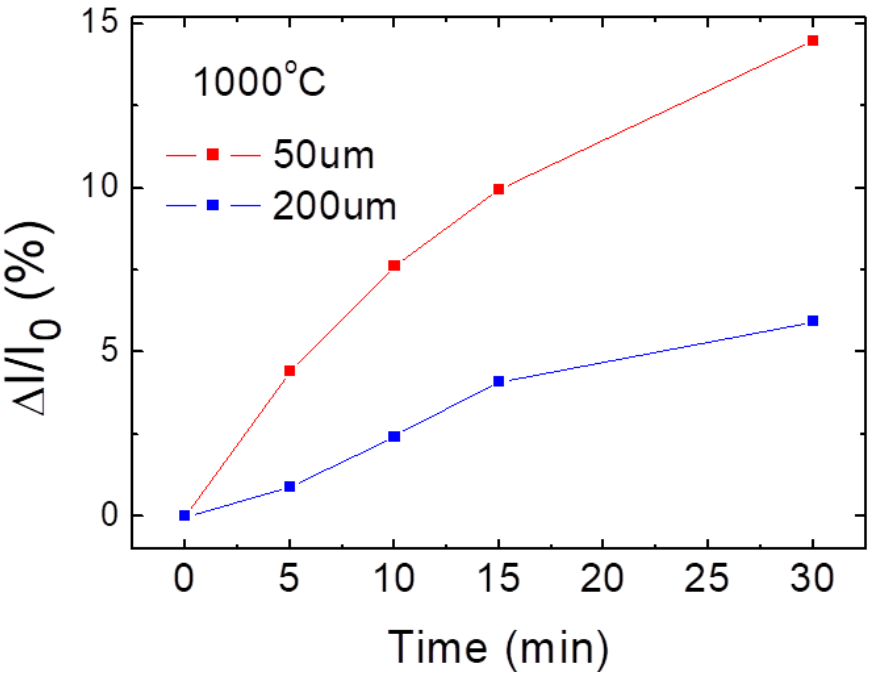

Figura 7.2.2. Respuesta UV relativa muestra 1000_o C de 50 µm vs 200 µm.

8 Resultados experimentales: Futuras aplicaciones para el uso de materiales en MEMS.

Estructuras basadas en Si y SiO_2 son actualmente de uso fundamental en la industria electrónica, específicamente en el área de MEMS. Con la experimentación básica y avanzada se obtuvieron herramientas suficientes para preparar muestras para TEM y fabricar estructuras tipo cantiléver así como materiales con aplicaciones en sensores electromecánicos y optomecánnicos, así como en aplicaciones biomédicas de la industria MEMS.

8.1 Cantiléver por erosión de iones.

Se microestructuraron por FIB voladizos tipo cantiléver por medio de FIB. Utilizando el parámetro 3, se llegó a una estructura final muy fina, aproximadamente 800 nm de grosor (Figura 8.1.2), suspendida por uno de sus extremos hasta una longitud de ~4 µm. Cuatro de estas estructuras se muestran en la Figura 8.1.1.

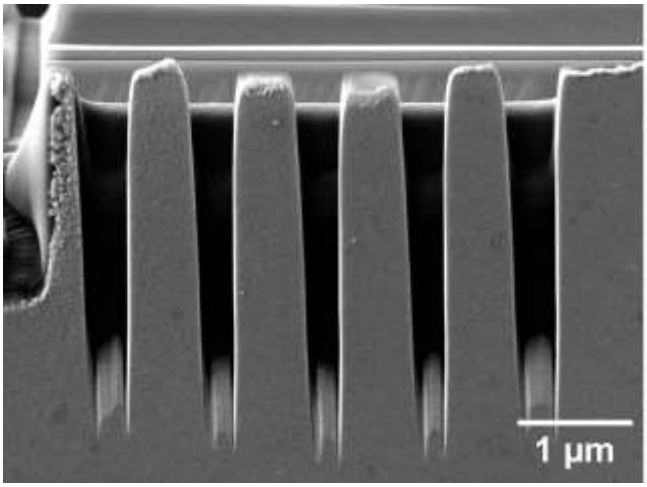

Figura 8.1.1. Imagen SEM de cantilévers fabricados en sustrato de Si por erosión de iones.

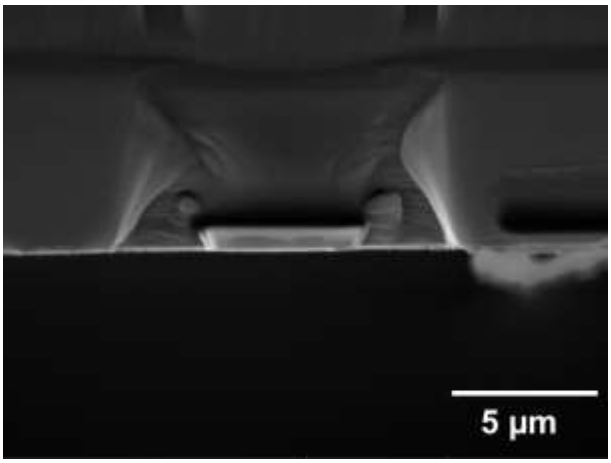

Figura 8.1.2. Vista frontal de cantiléver con ~800 nm de grosor.

Las estructuras fueron depositadas con Au térmico, posteriormente se erosionaron en ellas nanoserpentines que funcionan como contacto eléctrico en aplicaciones microelectrónicas (Figura 8.1.3).

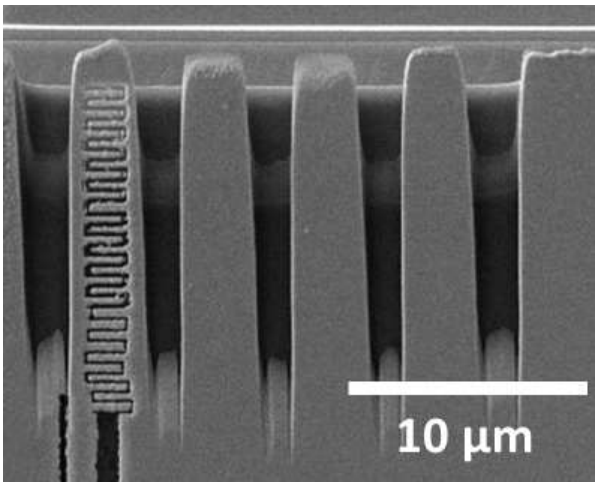

Figura 8.1.3. Cantiléver nano estructurado en película de Au depositada por evaporación térmica.

Estas estructuras tipo cantiléver pueden ser utilizadas en distintas aplicaciones mediante la funcionalización de la superficie. La clave está en la deposición controlada de películas funcionales convirtiendo el cantiléver en un sensor químico o bioquímico, óptico, eléctrico,de presión, ect. [55, 56, 57, 58, 59, 60]

9 Conclusiones

Se fabricaron por medio del sistema FIB-SEM y se estudiaron micro y nano estructuras basadas en Si cristalino, silicio amorfo y óxido de silicio, a partir de películas delgadas de platino, Aluminio, oro, cobre y plata depositadas por evaporación térmica, espurreo y pulverización de haz de iones focalizados. Las nanoestructuras obtenidas se estudiaron a detalle por espectroscopia elipsométrica de ángulo variable, espectroscopia de dispersión energía de rayos X, UV- visible, y caracterización eléctrica I-V.

El efecto de galio en sustratos y películas metálicas fue estudiado a partir de películas muy delgadas de Au, Cu y Au/Cu depositadas por erosión de haz de iones focalizados. Las películas obtenidas fueron sometidas a recocido rápido en alto vacío con el que se obtuvieron nanopartículas con tamaños que dependen de la dosis de Ga^{+} implantada para aplicaciones en plasmónica.

Diferentes tipos de nanotubos de óxido de titanio sintetizados por métodos electroquímicos bajo diferentes condiciones fueron caracterizados. Relación entre variables de fabricación como; corriente, voltaje, solución y tiempo de anodización, y sus características principales como; longitud de tubo, diámetro interno y externo, y grosor de pared fue definida por medio de microscopia SEM y el sistema FIB.

Muestras de nanotubos de TiO_2 en fase amorfa en sustratos de Ti puro y Ti6Al4V fueron sometidos a recocidos térmicos en los que se consiguió fase anatasa útil en sensores UV. Los recocidos fueron desde los 250 hasta los 550^{o} C y los cambios estructurales se estudiaron por difracción de rayos X y espectroscopia Raman.

Diferentes tipos de nanotubos de TiO_2 sintetizados por métodos electroquímicos a partir de sustratos de Ti puro y Ti6Al4V fueron estudiados y microestructurados por medio del sistema FIB-SEM. Sus características ópticas se estudiaron por espectroscopía elipsométrica, los datos obtenidos fueron utilizados en algoritmos matemáticos para su aplicación en minería de datos.

Nanotubos de óxido de titanio sintetizados en sustrato de Ti6Al4V en fase amorfa y anatasa fueron estudiados en aplicaciones de sensores de gas. El cambio relativo de reflectancia fue medido en ambos tipos de nanotubos en ambiente de etanol demostrando una sensitividad que depende del diámetro de los nanotubos y en caso de nanotubos amorfos la sensitividad aumenta con la disminución del diámetro, mientras que en muestras recocidas se observa una tendencia opuesta.

10 Bibliografía

[1] ProMéxico, con datos del Sistema de Cuentas Nacionales, INEGI, 2017, [En línea].

[2] Jaeger, R. C. (2001). Introduction to Microelectronic Fabrication: Volume 5 of Modular Series on Solid State Devices (Vol. 2). Upper Saddle River: Prentice Hall.)..

[3] Nanochemistry: A Chemical Approach to Nanomaterials, Geoffrey A. Ozin,André C. Arsenault,Ludovico Cademartiri.

[4] Eklund, P. (2007). Multifunctional nanostructured Ti-Si-C thin films (Doctoral dissertation, Institutionen för fysik, kemi och biologi).)y (Minoli, D. (2005). Nanotechnology applications to telecommunications and networking. John Wiley & Sons..

[5] Streetman, B. G., & Banerjee, S. (1995). Solid state electronic devices (Vol. 4). Englewood Cliffs, NJ: Prentice Hall.) .

[6] Kaxiras, E., & Efthimios, K. (2003). Atomic and electronic structure of solids. Cambridge University Press..

[7] Sommers, M. A. (2008). Understanding the elements of the periodic table–silicon. The Rosen Publishing Inc., New York, 404(22), 405..

[8] Gad-el-Hak, M. (2005). MEMS: design and fabrication. CRC press..

[9] Brown, A. K. (2005). Gps/ins uses low-cost mems imu. IEEE Aerospace and Electronic Systems Magazine, 20(9), 3-10..

[10] Sarvar, F., Hutt, D. A., & Whalley, D. C. (2002). Application of adhesives in MEMS and MOEMS assembly: a review. In 2nd International IEEE Conference on Polymers and Adhesives in Microelectronics and Photonics. POLYTRONIC 2002.

[11] Smith, C. S. (1954). Piezoresistance effect in germanium and silicon. Physical review, 94(1), 42..

[12] Adams, A. C. (1988). Dielectric and polysilicon film deposition. VLSI technology, 233-271..

[13] Schmidt, M. A., Howe, R. T., Senturia, S. D., & Haritonidis, J. H. (1988). Design and calibration of a microfabricated floating-element shear-stress sensor. IEEE Transactions on Electron Devices, 35(6), 750-757..

[14] Mahadevan, R., Mehregany, M., & Gabriel, K. J. (1990). Application of electric microactuators to silicon meromechanics. Sensors and Actuators A: Physical, 21(1-3), 219-225..

[15] Dual-Beam FIB-SEM system, Techniques and Automated Applications. Richard J Young and Mary Moore.

[16] Reyntjens, S., & Puers, R. (2001). A review of focused ion beam applications in microsystem technology. Journal of micromechanics and microengineering, 11(4), 287..

[17] Lyra Microscope User Manual..

[18] Principios básicos del Microscopio Electrónico de Barrido… Jaime Renau-Piqueras & Magdalena Faura..

[19] Bell, D. C., & Garratt-Reed, A. J. (2003). Energy dispersive X-ray analysis in the electron microscope. Garland Science..

[20] Fujiwara, H. (2007). Spectroscopic ellipsometry: principles and applications. John Wiley & Sons..

[21] Wang, Y. L., Chakrapani, V., Anderson, T., Zavada, J., Abernathy, C., & Hite, J. (2015). State-of-the-art Program on Compound Semiconductors 57 (SOTAPOCS 57). The Electrochemical Society..

[22] Höflich, K., Yang, R. B., Berger, A., Leuchs, G., & Christiansen, S. (2011). The Direct Writing of Plasmonic Gold Nanostructures by Electron-Beam-Induced Deposition. Advanced materials, 23(22-23), 2657-2661..

[23] Y. Lan, W. Chang, Y. Chang, C. Chang, C. Chen, Effect of focused ion beam deposition induced contamination on the transport properties of nano devices, Nanotechnology 26 (2015) 1–5..

[24] T.B. Massalski, J.L. Murray, L.H. Bennett, H. Baker (Eds.), Binary Alloy Phase Diagrams, American Society for Metals, Metals Park, OH, 1986..

[25] B. Predel, Cu-Ga (Copper-Gallium), Cr-Cs – Cu-Zr, in: O. Madelung (Ed.), Phase

Equilibria, Crystallographic and Thermodynamic Data of Binary Alloys, in Landolt-Börnstein - Group IV Physical Chemistry, vol. 5D, Springer, 1994, pp. 1–8..

[26] J. Wang, S. Chen, K. Cui, D. Li, D. Chen, Approach and coalescence of gold nano- particles driven by surface thermodynamic fluctuations and atomic interaction forces, ACS Nano 10 (2016) 2893–2902..

[27] J. Lee, J. Lee, T. Tanaka, H. Mori, In situ atomic-scale observation of melting point suppression in nanometer-sized gold particles, Nanotechnology 20 (2009) 1–4..

[28] E.A. Olson, M.Y. Efremov, M. Zhang, Z. Zhang, L.H. Allen, Size-dependent melting of Bi nanoparticles, J. Appl. Phys. 97 (3) (2005) 1–9..

[29] P.C. Wu, T. Kim, A.S. Brown, M. Losurdo, G. Bruno, H.O. Everitt, Real-time plasmon resonance tuning of liquid Ga nanoparticles by in situ spectroscopic ellipsometry, Appl. Phys. Lett. 90 (10) (2007) 1–3..

[30] Y. Yang, J.M. Callahan, T. Kim, A.S. Brown, H.O. Everitt, Ultraviolet nano-plasmonics: a demonstration of surface-enhanced Raman spectroscopy, fluorescence, and photodegradation using gallium nanoparticles, Nano Lett. 13 (6) (2013) 2837–2841..

[31] Y. Yang, N. Akozbek, T. Kim, J.M. Sanz, F. Moreno, M. Losurdo, A.S. Brown, H.O. Everitt, Ultraviolet–visible plasmonic properties of gallium nanoparticles investigated by variable-angle spectroscopic and Mueller matrix ellipsometry, ACS Photonics 1 (7)..

[32] T. Zhang, Y. Wang, K. Appusamy, B. Huang, J. Wang, F. Liu, S. Blair, S. Guruswamy, A. Nahata, Gallium platinum alloys–a new material system for UV plasmonics, Opt. Mater. Express 7 (8) (2017) 2880–2887..

[33] C.L. Nehl, J.H. Hafner, Shape-dependent plasmon resonances of gold nanoparticles, J. Mater. Chem. 18 (21) (2008) 2415–2419..

[34] Q. Wang, Q. Li, X. Yang, K. Wang n, S. Du, H. Zhang, Y. Nie, Graphene oxide–gold nanoparticles hybrids-based surface plasmon resonance for sensitive detection of microRNA, Biosens. Bioelectron. 77 (2016) 1001–1007..

[35] T. Sekino, Synthesis and applications of Titanium oxide nanotubes, in: T. Kijima (Ed.), Inorganic and Metallic Nanotubular Materials. Topics in Applied Physics

(2010), vol. 117, Springer-Verlag, Berlin Heidelberg, 2010, pp. 17e32, https://doi.org/10.1007/.

[36] P. Roy, S. Berger, P. Schmuki, TiO2 nanotubes: synthesis and applications, Angew. Chem. Int. Ed. 50 (2011) 2904e2939..

[37] M. Pelaez, N. Nolan, S. Pillai, M. Seery, P. Falaras, A.G. Kontos, P.S.M. Dunlop, J.W.J. Hamiltone, J.A. Byrne, K. O'Shea, M.H. Entezari, D.D. Dionysiou, A Review on the visible light active Titanium dioxide photocatalysts for environmental applications, .

[38] S. Bhardwaj, T. Rana, P. Laha, A. Barman, S. Biswas, Study of Titanium dioxide nanotube array for the application in dye-sensitized solar cells, Int. J. Mach. Mach. Mater. 2 (2014) 47e50..

[39] V. Galstyan, A. Vomiero, I. Concina, A. Braga, M. Brisotto, E. Bontempi, G. Faglia, G. Sberveglieri, Vertically aligned TiO2 nanotubes on plastic substrates for flexible solar cells, Small 7 (2011) 2437e2442, https://doi.org/10.1002/ smll.201101356..

[40] I. Paramasivam, H. Jha, N. Liu, P. Schmuki, A review of photocatalysis using self-organized TiO2 nanotubes and other ordered oxide nanostructures, Small 8 (2012) 3073e3103, https://doi.org/10.1002/smll.201200564. Epub 2012 Sep. 10..

[41] K. Lee, A. Mazare, P. Schmuki, One-dimensional titanium dioxide nano- materials: nanotubes, Chem. Rev. 114 (2014) 9385e9454, https://doi.org/ 10.1021/cr500061m..

[42] J.M. Macak, H. Tsuchiya, L. Taveira, A. Ghicov, P. Schmuki, Self-organized nanotubular oxide layers on Ti-6Al-7Nb and Ti-6Al-4V formed by anodization in NH4F solutions, J. Biomed. Mater. Res. A. 75 (2005) 928e933, https:// doi.org/10.1002/jbm.a.3050..

[43] Ch. J. Frandsen, K.S. Brammer, S. Jin, Variations to the nanotube surface for bone regeneration, Int. J. Biomater. 2013 (2013) 513680e513710, https:// doi.org/10.1155/2013/513680..

[44] K.M. Kummer, E.N. Taylor, N.G. Durmas, K.M. Tarquinio, B. Ercan, T.J. Webster, Effects of different sterilization techniques and varying anodized TiO2 nano- tube dimensions on bacteria growth, J. Biomed. Mater. Res. B Appl. Biomater. 101

(2013) 677e688..

[45] E.Beltran-Partida, B.Valdez-Salas,A.Escamilla,M.Curiel,E.Valdez-Salas,N.Nedev,J.M.Bastidas,Disinfection of titanium dioxide nanotubes using super-oxidized water decrease bacterial viability without disrupting osteo- blast behavior,Mater. Sci. Eng.(2016).

[46] E.Beltrán-Partida,B.Valdez-Salas,M.Curiel-Álvarez,S.Castillo-Uribe,A.Escamilla,N.Nedev,Enhanced antifungal activity by disinfected titanium dioxide nanotubes via reduced nano-adhesion bonds,Mater.Sci.Eng.C76(2017)59e65, https://doi.org/10.1016/j.msec.2017.

[47] A.Butt,A.Hamlekhan,S.Patel,D.Royhman,C.Sukotjo,M.T.Mathew,T.Shokuhfar,Ch. Takoudis,A novel investigation of the formation of Titanium oxide nanotubes on thermally formed oxide of Ti-6Al-4V,J.Oral Implantol.XLI(2015)523e531, https://doi.org/10.1563/AAID-JOI.

[48] V. Galstyan, E. Comini, G. Faglia, G. Sberveglieri, TiO2 nanotubes: recent advances in synthesis and gas sensing properties, Sensors 13 (2013) 14813e14838, https://doi.org/10.3390/s131114813..

[49] Y. LiXia, L. ShengLian, C. QingYun, Y. ShouZhuo, A review on TiO2 nanotube arrays: fabrication, properties, and sensing applications, Chin. Sci. Bull. 55 (2010) 331e338, https://doi.org/10.1007/s11434-009-0712-3..

[50] C.A.Grimes,K.G.Ong,O.K.Varghese,X.P.Yang,G.Mor,M.Paulose,E.C.Dickey,C.M. Ruan,M.V.Pishko,J.W.Kendig,A.J.Mason,A sentinel sensor network for hydrogen sensing, Sensors 3 (2003) 69e82, https://doi.org/10.3390/ s30300069..

[51] N. Kilinc, E. Sennik, Z.Z. Ozturk, Fabrication of TiO2 nanotubes by anodization of Ti thin films for VOC sensing, Thin Solid Films 520 (2011) 953e958..

[52] P. Roy, S. Berger, P. Schmuki, Tio2 nanotubes: synthesis and applications, Nanoscience 50 (2011) 2904–2939..

[53] Y.Iwasaki,T.Nakamiya,R.Kozai,F.Mitsugi,T.Ikegami,An image analysis algorithm.

[54] Caro-Gutiérrez, J., Peréz-Landeros, O. M., González-Navarro, F. F., Curiel-Álvarez, M. A., Valdez-Salas, B., & Radnev-Nedev, N. (2019). Data mining to predict the average outer diameter of vertically aligned TiO2 nanotubes.

Computational Materials Science.

[55] Fritz, J. (2008). Cantilever biosensors. analyst, 133(7), 855-863..

[56] Bietsch, A., Zhang, J., Hegner, M., Lang, H. P., & Gerber, C. (2004). Rapid functionalization of cantilever array sensors by inkjet printing. Nanotechnology, 15(8), 873..

[57] Sievilä, P., Rytkönen, V. P., Hahtela, O., Chekurov, N., Kauppinen, J., & Tittonen, I. (2007). Fabrication and characterization of an ultrasensitive acousto-optical cantilever. Journal of Micromechanics and Microengineering, 17(5), 852..

[58] Dufour, I., Josse, F., Heinrich, S., Lucat, C., Ayela, C., Ménil, F., & Brand, O. (2010). Unconventional uses of cantilevers for chemical sensing in gas and liquid environments. Procedia Engineering, 5, 1021-1026..

[59] Minne, S. C., Manalis, S. R., & Quate, C. F. (1995). Parallel atomic force microscopy using cantilevers with integrated piezoresistive sensors and integrated piezoelectric actuators. Applied Physics Letters, 67(26), 3918-3920..

[60] Lien, V., & Vollmer, F. (2007). Microfluidic flow rate detection based on integrated optical fiber cantilever. Lab on a Chip, 7(10), 1352-1356..

11 Lista de tablas y figuras.

11.1 Tablas.

11.2 Figuras.

12 Apéndices

Vacuum 157 (2018) 166–172

Contents lists available at ScienceDirect

Vacuum

journal homepage: www.elsevier.com/locate/vacuum

Gold, copper and gold/copper bimetallic nanoparticles obtained by focused ion beam sputter deposition and rapid thermal annealing

Oscar Perez Landeros[a,*], Nicola Nedev[a], Mario Curiel Alvarez[a], Benjamin Valdez Salas[a], Alejandro Barajas[a], David Mateos Anzaldo[a], Roumen Nedev[b], Abraham Arias Leon[c]

[a] Universidad Autónoma de Baja California, Instituto de Ingeniería, Mexico
[b] Universidad Politécnica de Baja California, Mexico
[c] Universidad Autónoma de Baja California, Facultad de Ingeniería, Mexico

ARTICLE INFO

Keywords:
Au
Cu
Au/Cu
Nanoparticles
FIB sputter deposition
RTA

ABSTRACT

Gold, copper and gold/copper thin layers were obtained in FIB/SEM system by Focused Ion Beam sputter deposition. Layers deposited on SiO_2/Si and quartz substrates were subjected to Rapid Thermal Annealing (RTA) in vacuum at 1100 °C. One minute annealing of 20 nm thick films leads to formation of nanoparticles with average size of ~20 nm but does not change the morphology of 170 nm Au and 180 nm Cu films. Implantation of Ga ions into SiO_2/Si substrate before deposition of ~20 nm Au layers has a strong effect on the nanostructures formed after 1 min annealing. Implantation at 30 kV for 1 and 2 min leads to formation of arbitrary shape nanoislands, which are much larger than the nanoparticles outside of the implanted region. Increase of the implantation time to 4 and 16 min leads to formation of large spheres, the size of which increases with the implantation time. The observed Ga effect is explained by the lower melting temperatures of Au/Ga and Cu/Ga binary alloys and by increased nanoparticle mobility, which favors the coalescence process. Gold nanoparticles with size of ~20 nm obtained by RTA on control quartz substrate showed local surface plasmon resonance at 535 nm.

1. Introduction

In the last decade Focused Ion Beam/Scanning Electron Microscope (FIB/SEM) systems have been used to deposit a variety of nanoscale materials. The depositions have been performed using metal-organic compounds obtained from gas, liquid or solid source, which can be heated. The precursor molecules are injected in the vacuum chamber close to the substrate surface by gas-injection systems, adsorbed on the surface and decomposed by electron or ion beam. The most common application of electron/ion beam deposition is surface protection by depositing a thin metal or insulator layer prior to etching trenches or nanopatterns. In addition, Focused Electron Beam Induced Deposition (FEBID) has been used to obtain various types of nanostructures by direct writing at the nanoscale, e.g. silicon nanodots [1], gold nanoscale tips [2], high aspect ratio ultra sharp carbon tips [3], plasmonic gold nanostructures [4] and spiral apertures for transmission electron microscopes [5]. FIB/SEM systems are considered among the instruments for fabrication and *in situ* imaging of materials in the emerging 3D nanofabrication/imaging technologies for future manufacturing of devices [6]. A drawback of the nanostructures obtained by FEBID is carbon contamination from the metal-organic precursors [7,8].

Another technique that can be applied to deposit thin films in FIB/SEM systems is Ion Beam Sputtering (IBS) [9]. Indeed, redeposition is one of the artefacts related to FIB milling [10]. However, when Ga ion beam is focused on a target material positioned close to a substrate it can be used to sputter atoms that will be deposited on the substrate. To the best of our knowledge such deposition has only been used to coat cantilever tips of atomic force microscope with magnetic materials [11]. An advantage of the focused ion beam sputter deposition (FIBSD) compared to electron/ion beam induced deposition is that various materials can be deposited avoiding the limitation of available gas injecting systems. Another advantage is that expensive materials can be deposited without the need to buy relatively large sputtering targets to prove a concept and optimize the properties of the deposited films [11].

In recent years, there is an increased interest in Au nanoparticles because of their electronic [12], catalytic [13], optical and thermal properties [8,14–17]. In particular, the thermal properties of noble metal nanoparticles have been extensively studied for potential application in plasmonic photothermal therapy [18,19]. Gold-copper bimetallic nanoparticles have been studied for optical [20] and catalytic [21,22] applications.

Various vacuum techniques have been used to obtain noble metal

* Corresponding author.
E-mail address: oscar.manuel.perez.landeros@uabc.edu.mx (O.P. Landeros).

https://doi.org/10.1016/j.vacuum.2018.08.033
Received 4 June 2018; Received in revised form 25 June 2018; Accepted 17 August 2018
Available online 18 August 2018
0042-207X/

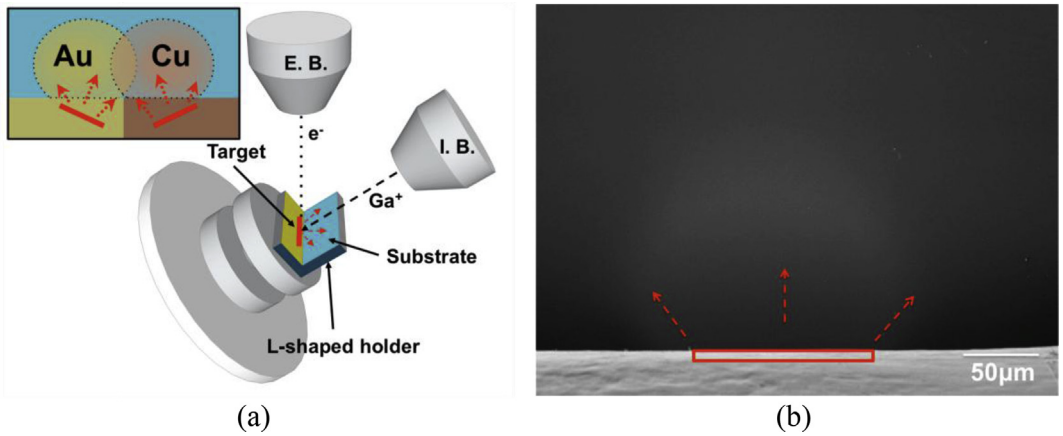

Fig. 1. (A) A schematic layout of the deposition process; E.B. - electron beam, I.B. - ion beam; (b) Schematic representation of a rectangle area on Cu target from which material was sputtered. The inset figure in (a) shows the geometry used in bilayer depositions and the region with overlapping films.

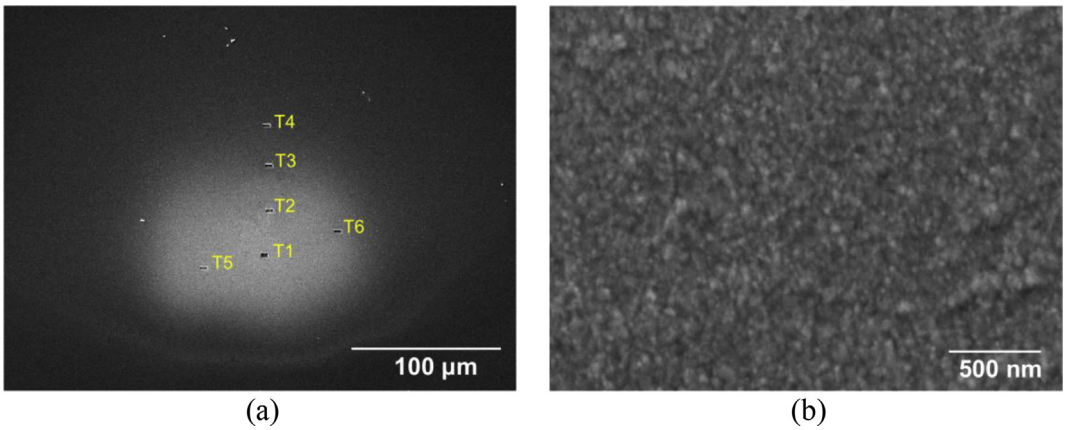

Fig. 2. (A) Full view of a Cu layer with trenches milled prior to annealing; (b) SEM image of a thick layer taken close to T1.

nanoparticles (NPs). Gold nanoparticles were formed in co-evaporated nanocomposite fullerene C70—Au by annealing in inert atmosphere [23]. Au NPs have been obtained on titanium surface from layers deposited by magnetron sputtering or electron cyclotron resonance ion source for application in implants [24].

Here, we present results for Au, Cu and Au/Cu thin metal layers obtained by sputter deposition in FIB/SEM system. After the deposition, the layers were subjected to rapid thermal annealing in vacuum in order to form Au, Cu and Au/Cu nanoparticles. The effect of Ga ions, implanted in SiO_2/Si substrates before Au layer deposition, on the size and morphology of the obtained nanostructures was studied. An advantage of the NPs obtained by the proposed method is that they do not contain carbon contaminations, which is essential for applications in the areas of plasmonics and metamaterials [4].

2. Materials and methods

The deposition was carried out in a dual beam FIB/SEM system TESCAN Lyra 3 XMU. The target and substrate were placed at 90° relative to each other on an L-shaped metal holder (Fig. 1 (a)). The target was positioned as close as possible to the substrate. During the deposition the platform was tilted at 55° relative to its horizontal position so that the Ga ion beam was perpendicular to the plane of the target holder and parallel to the substrate.

Quartz and thermally oxidized crystalline Si with a 25 nm SiO_2 on top were used as substrates. High purity Au and Cu wires were used as targets. The material to deposit was sputtered from rectangular areas with fixed width of 15 μm and variable length (Fig. 1 (b)). The film thickness was varied by using different milling times. The acceleration voltage, beam current and spot size were set to 30 kV, 1 nA, and 50 nm and the chamber pressure during the deposition was 3.5×10^{-2} Pa. To deposit Au/Cu bilayers gold and copper were consecutively sputtered from wires placed close together touching each other side by side. To obtain overlapping the milling was carried out from areas oriented at 35° to the wire edges (inset in Fig. 1 (a)). The film thicknesses were determined by milling trenches at various positions. An advantage of using FIB/SEM dual beam system is the possibility to monitor the ion beam sputter deposition process in real time.

After the deposition, the layers were subjected to a thermal annealing under vacuum of 6.7×10^{-3} Pa for 1 or 5 min. The annealing was carried out using electric current heated tungsten plate on which the samples were placed. The temperature of the plate during the annealing was 1100 °C.

The layer thicknesses of control samples with metal deposited on quartz substrates by thermal evaporation were measured by variable angle ellipsometer J. A. Woollam M-2000. Transmission spectra of layers on the quartz substrate were measured in the 185–1400 nm range using UV–Vis spectrometer Shimadzu 2600.

3. Results and discussion

Fig. 2 (a) shows SEM image of Cu layer deposited on SiO_2/Si substrate by milling of volume with dimensions of 60 × 15 × 0.3 μm. Because the target was positioned at 90° to the substrate, the layer thickness varies in direction perpendicular to the target. A variation in direction parallel to the target is also observed, in particular in regions close to the lateral edges of the thick film. The thickness measured at various distances from trench one (T1), positioned in the center of the

Table 1
Thickness of the deposited Cu layer.

Trench	T1	T2	T3	T4	T5	T6
Distance to T1 (μm)	0	30	60	90	40	50
Thickness (nm)	185	119	50	30	99	90

thick layer, is shown in Table 1. Fig. 2 (b) shows surface morphology close to T1 where the film thickness is ~180 nm. Similar granular morphology was observed for thicknesses in the 180-30 nm range. High temperature annealing for 1 and 5 min did not change the morphology of film with thickness in the above range. However, in areas where the thickness was less than 30 nm, the periphery of the image in Fig. 3 (a), the 1 min annealing leads to formation of nanoparticles with varying size and spatial density (Fig. 3 (b)). For example, in region 1 (R1), which is right out of the periphery of the continuous film nanoparticles with irregular shape and maximum size of ~400 nm were obtained (Fig. 3 (c)). With increase of the distance to R1 the size of the formed NPs decreases as a result of the smaller film thickness. Fig. 4 (a)-(c) shows nanoparticles formed at 30, 40 and 50 μm from R1. The largest nanoparticles in these regions are with size of 200, 150 and 70 nm, respectively. In addition, the nanoparticles change to more rounded shape with size decrease.

Similar results were obtained for Au deposited layers. As in the case of Cu high temperature annealing did not change the morphology of the thick layer (Fig. 5 (a)) and in a similar way leads to formation of nanoparticles in the periphery where the layer thickness was < 30 nm. An important difference was observed in the transition region between the thick film and the nanoparticle region where nanoislands with arbitrary shape were formed (Fig. 5 (b)). Fig. 5 (c) shows nanoparticles at a distance of 50 μm from the continuous film.

In contrast, films with thickness in the center of ~20 nm or less, obtained at shorter milling times, were flat and featureless for both, Au and Cu (not shown here). High temperature annealing for 1 min of ~20 nm thick Au and Cu films leads to formation of nanoparticles with almost spherical shape and average diameters of ~20 ± 2 and ~21 ± 2 nm, respectively (Fig. 6 (a), (b)). A second annealing of 1 min did not result in additional coalescence and increase of the average nanoparticle size; only the number of particles having a shape closer to a sphere increased.

Fig. 7 (a) shows SEM images of Au/Cu bimetallic nanoparticles obtained by 5 min annealing of Au/Cu bilayer. The NP size varies in a wide range, between 30 and 100 nm. Energy Dispersive X-ray Spectroscopy (EDS) revealed that the only elements in the nanoparticles are Au and Cu (Fig. 7 (b)). No Ga was detected. Areas with Cu residues between nanoparticles are also seen. The zones close around the NPs are almost free of residues.

Fig. 8 shows SEM image of an annealed Cu layer. Two regions with very few nanoparticles can be distinguished. Region 1 is around SiO_2 deposited by FEBID on a non-annealed Cu film in order to protect the metal surface before milling a trench. However, in this particular case no trench was etched. Although the deposition area was defined as 5 × 1 μm the region without nanoparticles is much larger, ~9 × 5 μm. The reason is deposition of silicon dioxide outside of the area intended to be protected and as a result the Cu layer was covered by SiO_2. This observation is in agreement with previous result reported for Pt contamination outside of the deposition area up to ~2 μm [25]. Region 2 is around a trench milled before the annealing process. Sparsely distributed particles are observed, some of them with size much larger than the nanoparticles outside of the region. Such effect of formation of larger metal nanoclusters was seen even in areas with very low Ga implantation dose, for example in areas used only to focus the ion beam on the surface. This finding motivated us to study in more details the implanted Ga^+ effect on the shape and size of the nanoclusters formed after high temperature annealing.

Ga ions were implanted into SiO_2/Si substrates for 1, 2, 4 and 16 min in FIB/SEM system under the following conditions: accelerating voltage of 30 kV, ion current of 1 pA and implantation area of 2 × 2 μm. Then, Au film with thickness of ~20 nm (determined ellipsometrically) was thermally evaporated on the implanted substrates as well as on a control sample of quartz. All metallized samples were annealed for 1 min. The obtained results for the control and the Ga-implanted samples are shown in Figs. 9 and 10. Gold nanoparticles with diameter of approximately 20 nm were formed on the quartz substrate (Fig. 9). For all Ga-implanted samples there is a significant difference in the size of the nanoclusters formed in the implanted area and outside of it (Fig. 10). It is worth noting that for 2 min or larger implantation time the implanted area shifts in the direction of electrical grounding due to charging of the SiO_2 surface (Fig. 10 (b) – (d)). For this reason the total dose was implanted only in the region where the initial and final areas overlap. Nanoislands with arbitrary shapes were formed on the surface of 1 and 2 min implanted substrates separated by large areas without gold or zones with Au residues (Fig. 10 (a), (b)). The nanoislands on the 2 min sample have on average slightly larger length and width than those on the 1 min. The nanoparticles outside of the implanted regions are with size of ~20 nm. Further increase of the implantation time to 4 min leads to formation of nanospheres with larger diameters than on quartz. Outside of the overlapping areas, where the implanted dose was smaller, the nanostructures in Fig. 10 (c) exhibit shape similar to the nanoislands in Fig. 10 (a), (b). On the surface of the 16 min implanted sample only few nanoparticles with diameter larger than 200 nm were formed (Fig. 10 (d)).

One of the possible reasons for the observed effect of Ga on formation of nanostructures is lowering of the melting temperatures (T_m) of the Au/Ga and Cu/Ga binary alloys [26,27]. The lowering of T_m depends on the Ga percentage and is more pronounced for the Au/Ga alloy. It may be assumed that for longer implantation time the Ga concentration in the metal, resulting from diffusion out of the SiO_2/Si substrate, is high enough to maintain the melting point below the sample temperature during the whole annealing process. Thus, the

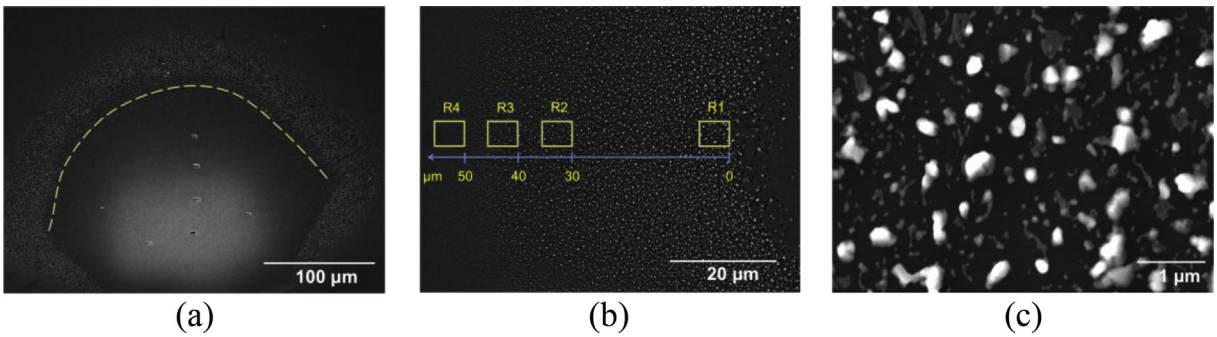

Fig. 3. (A) SEM image of a Cu layer after 1 min annealing; (b) nanoparticles with varying size and spatial density formed in areas where the film thickness was less than 30 nm. The regions R2, R3 and R4 are at 30, 40 and 50 μm from R1; (c) nanoparticles in R1.

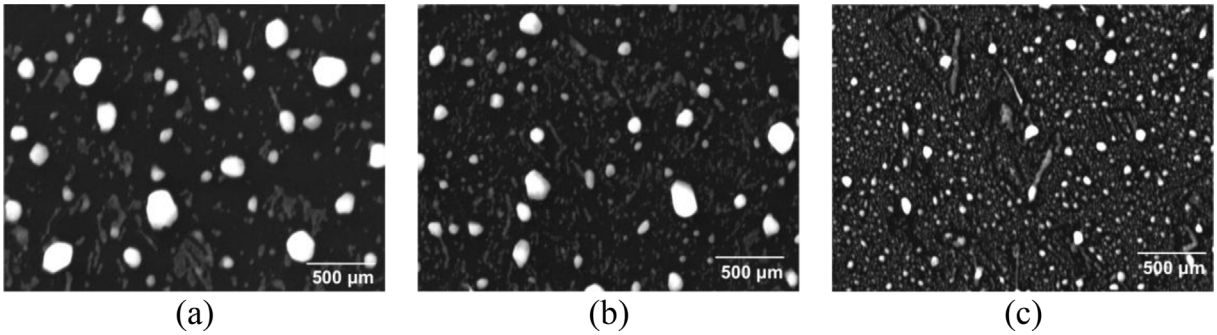

Fig. 4. Nanoparticles formed in regions R2 (a), R3 (b) and R4 (c); the images were obtained at 100 kx, while the image in Fig. 3 (c) (region R1) was obtained at 50 kx.

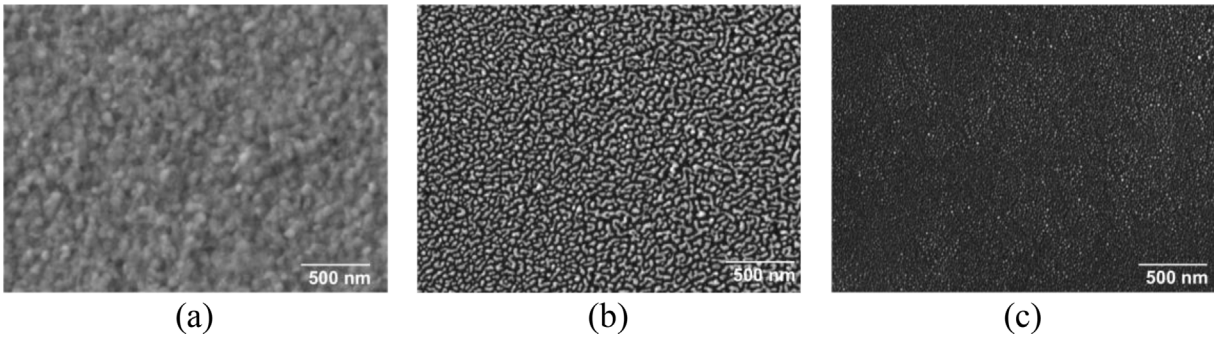

Fig. 5. SEM images of Au layer with thickness of ~170 nm deposited on SiO_2/Si substrate (a); region with arbitrary shape nanoislands formed in the transition area between thick film and nanoparticle region (b); nanoparticles at a distance of 50 μm from the continuous film (c).

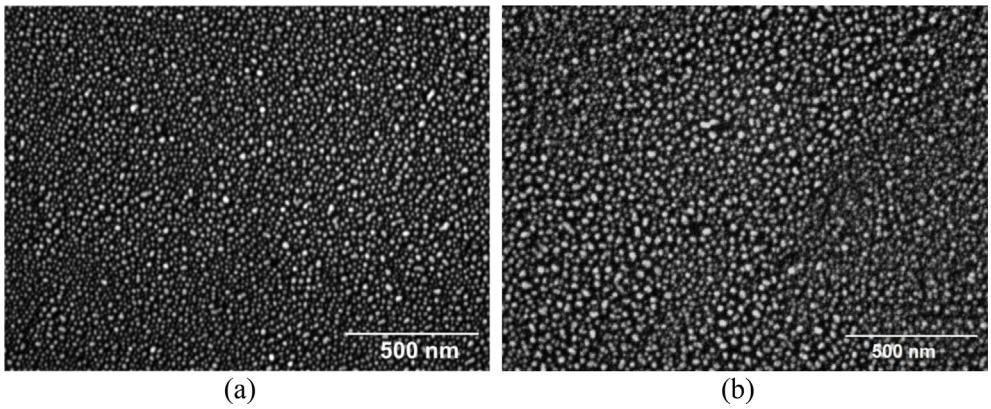

Fig. 6. SEM images of annealed for 1 min–20 nm thick Au (a) and Cu (b) layers.

formation of nanosphere and coalescence would occur at temperatures higher than T_m. EDS analysis taken after annealing confirmed the presence of Ga in the samples with larger implantation times. For example, the Ga concentration was > 12 atomic % in the Au nanospheres on the surface of 4 and 16 min implanted samples and less than 1 atomic % in nanostructures on the samples implanted for 1 and 2 min. It has been shown that the approach and coalescence of Au nanoparticles are enhanced by temperature and that when the annealing temperature is lower than T_m, the coalescence may lead to formation of different shapes including strip-type [28]. To test if the lowering of T_m is the only effect of Ga on the coalescence the following experiment was carried out. Samples without Ga^+ implantation and annealed for 1 min were additionally annealed up to 5 min in consecutive steps of 1 min. Some samples were annealed for 5 min in a single step. In none of these cases formation of nanoislands similar to those in Fig. 10 (a), (b) or large nanospheres like those in Fig. 10 (c), (d) was observed. It is well known that T_m of metal nanoparticles is lower than that of a thin film from the same material [29,30]. Thus, it could be expected that after 1 min annealing and formation of NPs with size of ~20 nm the subsequent annealing steps would lead to coalescence and formation of larger nanostructures. This was not observed, the only change was in the shape of the nanoparticles to a more spherical one. The obtained results indicate that the Ga effect is more complex than a simple lowering of the melting point of homogeneous Au/Ga alloy. It has been shown that deposition of Ga by molecular beam epitaxy leads to formation of isolated Ga nanoparticles [31–33] because Ga does not easily wet SiO_2 [34]. It may be assumed that high concentration of Ga in a region close to the Au/SiO_2 interface, due to Ga diffusion from the oxide into Au, modifies the surface and metal/SiO_2 interface energies leading to more favorable conditions for nanoparticle coalescence In addition, the lower melting temperature may lead to increased nanoparticle mobility. After optimization the observed effect of Ga on formation of nanostructures may be used to define patterns suitable for applications in nanodevices.

Fig. 11 shows UV–Vis spectra of ~20 nm thermally evaporated gold layer on quartz substrate without annealing and of layers annealed for 1 and 3 min (in three consecutive steps of 1 min). The annealed samples

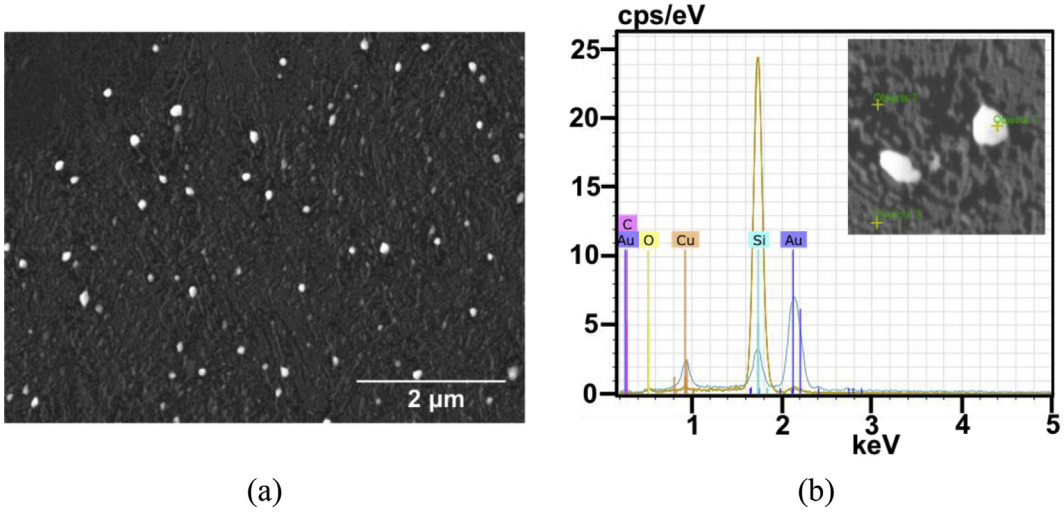

Fig. 7. (A) SEM images of Au/Cu bimetallic nanoparticles obtained by 5 min annealing of Au/Cu bilayer; (b) EDS results obtained on Au/Cu nanoparticle (Object 1) and on areas without (Object 2) and with (Object 3) metal residues.

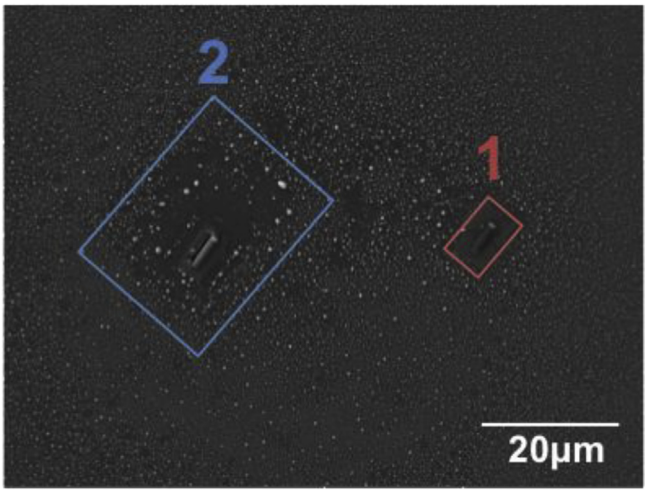

Fig. 8. SEM image of annealed Cu layer showing two regions with very few nanoparticles.

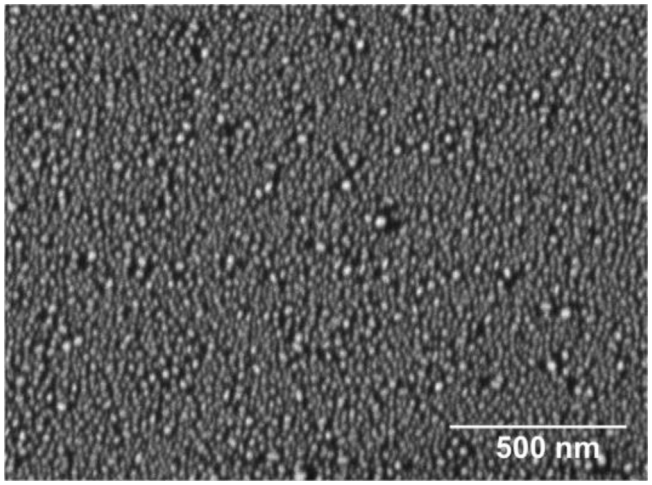

Fig. 9. Nanoparticles obtained on quartz substrate after thermal evaporation of ~20 nm Au layer and 1 min high temperature annealing.

display peaks at 557 and 535 nm due to localized surface plasmon resonance (LPSR) in Au nanoparticles. The peak maximum shifts towards shorter wavelengths with the increase of the annealing time because the nanoparticles change to a more spherical shape [35] as confirmed by SEM. The position of the LSPR maximum at 535 nm is slightly red-shifted compared to the LSPR peak of 18 ± 2 nm gold nanoparticles reported in Ref. [36] most likely because the NPs obtained here have a larger average size and the dielectric constant of the surrounding medium is different.

4. Conclusions

Thin Au, Cu and Au/Cu layers were successfully deposited by focused ion beam sputtering in FIB/SEM system. The obtained metal films do not contain carbon contamination, an important advantage for applications in the areas of plasmonics and metamaterials. EDS proved that Ga was not incorporated in the layers during the sputtering. Other advantage of the focused ion beam sputter deposition in FIB/SEM systems is the possibility to monitor the film formation in real time. FIBSD allows deposition of materials with high melting point and materials for which gas injecting systems are not integrated in the FIB/SEM. High temperature annealing for 1 min of Au, Cu and Au/Cu layers with thickness $\lesssim$ 25 nm leads to formation of nanoparticles but does not change essentially the morphology of thick films. It was found that implantation of Ga ions into SiO_2/Si substrates before deposition of ~20 nm Au layers enhances the nanoparticle coalescence during the annealing and leads to formation of larger nanostructures. The effect is more pronounced for higher implantation doses and above a given dose results in modification of the obtained nanostructures from predominantly strip-type to a spherical-type. The observed effect of Ga may be used to define nanoparticles arrays suitable for application in plasmonics after optimization of the implantation and annealing processes.

Data availability

The raw/processed data required to reproduce these findings cannot be shared at this time as the data also forms part of an ongoing study.

Acknowledgements

O.P.L. gratefully acknowledges fellowship support from the Consejo Nacional de Ciencia y Tecnología, Mexico (Grant No. 292624).

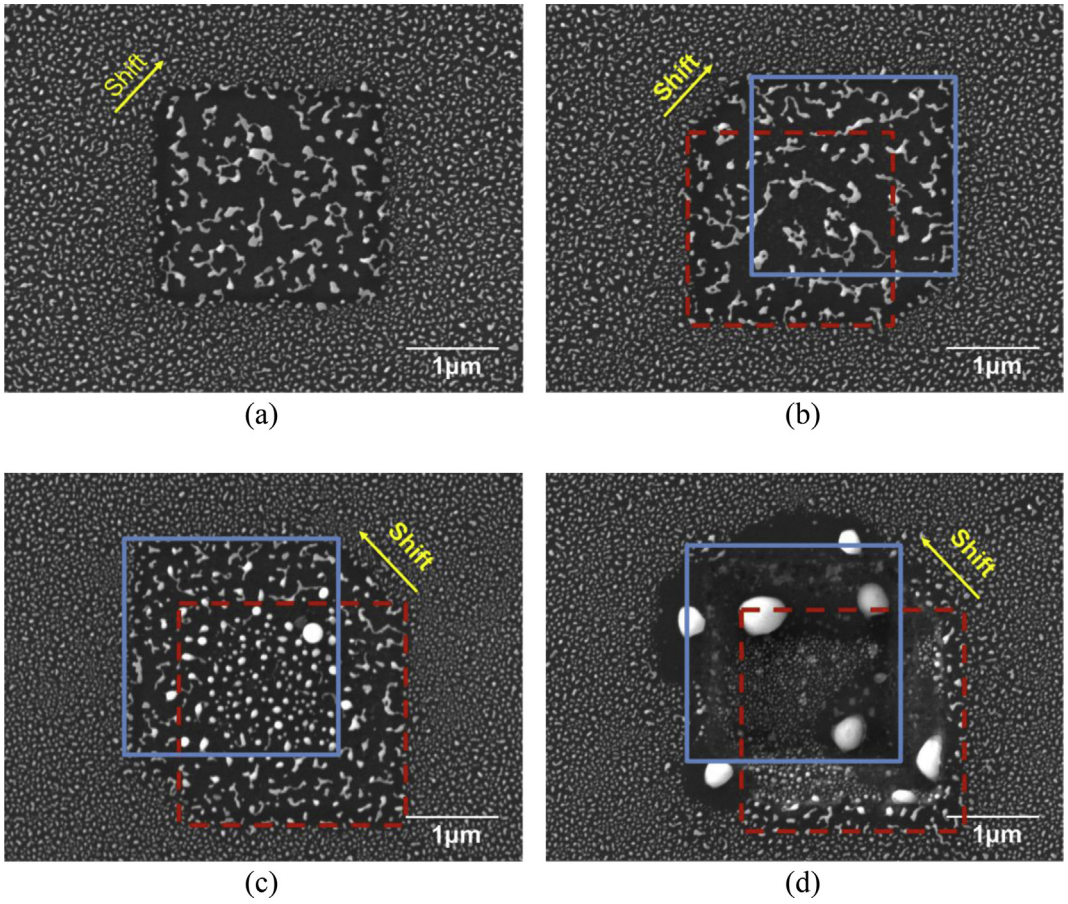

Fig. 10. SEM images of annealed Au layer deposited on SiO_2/Si substrate with implanted Ga ions for 1 (a), 2 (b), 4 (c) and 16 (d) min. Dashed (red) and solid (blue) squares show the initial and final area of implantation; the solid arrow shows the displacement direction. (For interpretation of the references to colour in this figure legend, the reader is referred to the Web version of this article.)

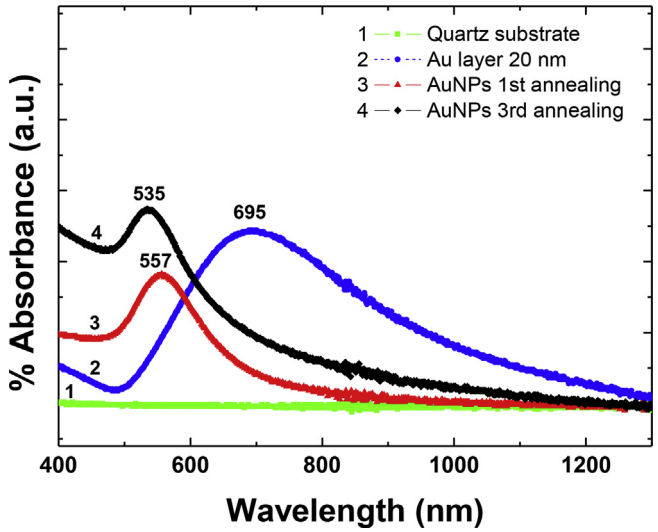

Fig. 11. UV–Vis spectra of samples on quartz substrate: curve 2–20 nm Au layer without annealing; curves 3 and 4 - annealed Au layers for 1 and 3 min, respectively. The absorbance of quartz substrate is also shown (curve 1).

References

[1] Y. Liu, X. Chen, K.W. Noh, S.J. Dillon, Electron beam induced deposition of silicon nanostructures from a liquid phase precursor, Nanotechnology 23 (38) (2012) 1–6.

[2] K. Mølhave, D.N. Madsen, A.M. Rasmussen, A. Carlsson, C.C. Appel, M. Brorson, C.J.H. Jacobsen, P. Bøggild, Solid gold nanostructures fabricated by electron beam deposition, Nano Lett. 3 (11) (2003) 1499–1503.

[3] J.A. Bieber, J.F. Pulecio, W.A. Moreno, Applications of electron beam induced deposition in nanofabrication, Devices, Circuits and Systems. (2008), ICCDCS (2008) 7th International Caribbean Conference on. IEEE, 2008.

[4] K. Höflich, R.B. Yang, A. Berger, G. Leuchs, S. Christiansen, The direct writing of plasmonic gold nanostructures by electron-beam-induced deposition, Adv. Mater. 23 (22-23) (2011) 2657–2661.

[5] A. Béchéa, R. Winkler, H. Plank, F. Hofer, J. Verbeecka, Focused electron beam induced deposition as a tool to create electron vortices, Micron 80 (2016) 34–38.

[6] G. Seniutinas, A. Balčytis, I. Reklaitis, F. Chen, J. Davis, C. David, S. Juodkazis, Tipping solutions: emerging 3D nano-fabrication/-imaging technologies, Nanophotonics 6 (5) (2017) 923–941.

[7] C. Haverkamp, K. Höflich, S. Jäckle, A. Manzoni1, S. Christiansen, Plasmonic gold helices for the visible range fabricated by oxygen plasma purification of electron beam induced deposits, Nanotechnology 28 (5) (2016) 1–8.

[8] P. Woźniak, K. Höflich, G. Brönstrup, P. Banzer, S. Christiansen, G. Leuchs, Unveiling the optical properties of a metamaterial synthesized by electron-beam-induced deposition, Nanotechnology 27 (2) (2015) 1–7.

[9] I.P. Jain, G. Agarwal, Ion beam induced surface and interface engineering, Surf. Sci. Rep. 66 (3–4) (2011) 771 – 172.

[10] K.A. Unocic, M.J. Mills, G.S. Daehn, Effect of gallium focused ion beam milling on preparation of aluminium thin foils, J. Microsc. (Oxf.) 240 (3) (2010) 227–238.

[11] C. Hyun, A.K.H. Lee, A. de Lozanne, Focused ion beam deposition of $Co^{71}Cr^{17}Pt^{12}$ and $Ni^{80}Fe^{20}$ on tips for magnetic force microscopy, Nanotechnology 17 (2006) 9211–9925.

[12] S.W. Boettcher, N.C. Strandwitz, M. Schierhorn, N. Lock, M.C. Lonergan, G.D. Stucky, Tunable electronic interfaces between bulk semiconductors and ligand-stabilized nanoparticle assemblies, Nat. Mater. 6 (8) (2007) 592–596.

[13] T. Zhang, H. Zhao, S. He, K. Liu, H. Liu, Y. Yin, C. Gao, Unconventional route to encapsulated ultrasmall gold nanoparticles for high-temperature catalysis, ACS Nano 8 (7) (2014) 7297–7304.

[14] B. Chen, M. Mokume, C. Liu, K. Hayashi, Structure and localized surface plasmon tuning of sputtered Au nano-islands through thermal annealing, Vacuum 110 (2014) 94–101.

[15] M. Fedoruk, M. Meixner, S. Carretero-Palacios, T. Lohmüller, J. Feldmann, Nanolithography by plasmonic heating and optical manipulation of gold nanoparticles, ACS Nano 7 (9) (2013) 7648–7653.

[16] K. R Berry Jr., A.G. Russell, P.A. Blake, D. Keith Roper, Gold nanoparticles reduced

in situ and dispersed in polymer thin films: optical and thermal properties, Nanotechnology 23 (2012) 1–11.
[17] A. Carattino, M. Caldarola, M. Orrit, Gold nanoparticles as absolute nanothermometers, Nano Lett. 18 (2018) 874–880.
[18] X. Huang, M.A. El-Sayed, Plasmonic photo-thermal therapy (PPTT), Alexandria J. Med. 47 (2011) 1–9.
[19] Z. Bao, X. Liu, Y. Liu, H. Liu, K. Zhao, Near-infrared light-responsive inorganic nanomaterials for photothermal therapy, Asian J. Pharmaceut. Sci. 11 (2016) 349–364.
[20] A.F. Alvarez-Paneque, B. Rodríguez-Gonzalez, I. Pastoriza-Santos, L.M. Liz-Marzań, Shape-templated growth of Au@Cu nanoparticles, J. Phys. Chem. C 117 (2013) 2474–2479.
[21] D. Kim, J. Resasco, Y. Yu, A.M. Asiri, Peidong Yang, Synergistic geometric and electronic effects for electrochemical reduction of carbon dioxide using gold–copper bimetallic nanoparticles, Nat. Commun. (2014) 1–8.
[22] H. Mistrya, R. Reskec, P. Strasser, B. Roldan Cuenya, Size-dependent reactivity of gold-copper bimetallic nanoparticles during CO_2 electroreduction, Catal. Today 288 (2017) 30–36.
[23] R. Singhal, R. Vishnoi, P. Sharma, G.D. Sharma, S. Chand, D. Kanjilal, J.C. Pivin, Synthesis, characterization and thermally induced structural transformation of Au-C70 nanocomposite thin films, Vacuum 142 (2017) 146–153.
[24] I. Csarnovics, P. Hajdu, S. Biri, Cs Hegedüs, S. Kökényesi, R. Rácz, A. Csik, Preliminary studies of creation of gold nanoparticles on titanium surface towards biomedical applications, Vacuum 126 (2016) 55–58.
[25] Y. Lan, W. Chang, Y. Chang, C. Chang, C. Chen, Effect of focused ion beam deposition induced contamination on the transport properties of nano devices, Nanotechnology 26 (2015) 1–5.
[26] T.B. Massalski, J.L. Murray, L.H. Bennett, H. Baker (Eds.), Binary Alloy Phase Diagrams, American Society for Metals, Metals Park, OH, 1986.
[27] B. Predel, Cu-Ga (Copper-Gallium), Cr-Cs – Cu-Zr, in: O. Madelung (Ed.), Phase Equilibria, Crystallographic and Thermodynamic Data of Binary Alloys, in Landolt-Börnstein - Group IV Physical Chemistry, vol. 5D, Springer, 1994, pp. 1–8.
[28] J. Wang, S. Chen, K. Cui, D. Li, D. Chen, Approach and coalescence of gold nanoparticles driven by surface thermodynamic fluctuations and atomic interaction forces, ACS Nano 10 (2016) 2893–2902.
[29] J. Lee, J. Lee, T. Tanaka, H. Mori, In situ atomic-scale observation of melting point suppression in nanometer-sized gold particles, Nanotechnology 20 (2009) 1–4.
[30] E.A. Olson, M.Y. Efremov, M. Zhang, Z. Zhang, L.H. Allen, Size-dependent melting of Bi nanoparticles, J. Appl. Phys. 97 (3) (2005) 1–9.
[31] P.C. Wu, T. Kim, A.S. Brown, M. Losurdo, G. Bruno, H.O. Everitt, Real-time plasmon resonance tuning of liquid Ga nanoparticles by in situ spectroscopic ellipsometry, Appl. Phys. Lett. 90 (10) (2007) 1–3.
[32] Y. Yang, J.M. Callahan, T. Kim, A.S. Brown, H.O. Everitt, Ultraviolet nanoplasmonics: a demonstration of surface-enhanced Raman spectroscopy, fluorescence, and photodegradation using gallium nanoparticles, Nano Lett. 13 (6) (2013) 2837–2841.
[33] Y. Yang, N. Akozbek, T. Kim, J.M. Sanz, F. Moreno, M. Losurdo, A.S. Brown, H.O. Everitt, Ultraviolet–visible plasmonic properties of gallium nanoparticles investigated by variable-angle spectroscopic and Mueller matrix ellipsometry, ACS Photonics 1 (7) (2014) 582–589.
[34] T. Zhang, Y. Wang, K. Appusamy, B. Huang, J. Wang, F. Liu, S. Blair, S. Guruswamy, A. Nahata, Gallium platinum alloys–a new material system for UV plasmonics, Opt. Mater. Express 7 (8) (2017) 2880–2887.
[35] C.L. Nehl, J.H. Hafner, Shape-dependent plasmon resonances of gold nanoparticles, J. Mater. Chem. 18 (21) (2008) 2415–2419.
[36] Q. Wang, Q. Li, X. Yang, K. Wang n, S. Du, H. Zhang, Y. Nie, Graphene oxide–gold nanoparticles hybrids-based surface plasmon resonance for sensitive detection of microRNA, Biosens. Bioelectron. 77 (2016) 1001–1007.

Journal of Alloys and Compounds 798 (2019) 394–402

Contents lists available at ScienceDirect

Journal of Alloys and Compounds

journal homepage: http://www.elsevier.com/locate/jalcom

Phase characterization and ethanol adsorption in TiO_2 nanotubes anodically grown on Ti6Al4V alloy substrates

Diana Nesheva [a, *], Tsvetanka Babeva [b], Marina Vasileva [b], Benjamin Valdez-Salas [c], Valeri Dzhurkov [a], Mirjana U. Grujić-Brojčin [d], Maja J. Šćepanović [d], Oscar Perez [c], Nikola Nedev [c], Mario Curiel [c], Tatjana Srećković [e]

[a] Georgi Nadjakov Institute of Solid State Physics, Bulgarian Academy of Sciences, Tzarigradsko Chaussee Blvd. 72, 1784, Sofia, Bulgaria
[b] Institute of Optical Materials and Technologies, Bulgarian Academy of Sciences, Acad.G. Bonchev Str., bl. 109, 1113, Sofia, Bulgaria
[c] Department of Corrosion and Materials, Engineering Institute, Autonomous University of Baja California, Blvd. Benito Juarez and Normal St., 21280, Mexicali, Baja California, Mexico
[d] Center for Solid State Physics and New Materials, Institute of Physics, University of Belgrade, Pregrevica 118, Belgrade, 11080, Serbia
[e] Institute for Multidisciplinary Research, University of Belgrade, Kneza Višeslava 1, 11030, Belgrade, Serbia

ARTICLE INFO

Article history:
Received 7 January 2019
Received in revised form
16 May 2019
Accepted 21 May 2019
Available online 23 May 2019

Keywords:
Nanostructured materials
Liquid-solid reactions
Oxide materials
Crystal structure
Microstructure
Optical properties

ABSTRACT

The anodic oxidation method is applied for preparation of TiO_2 nanotube (NT) arrays on Ti6Al4V alloy substrates. The NTs were of four different diameters (60, 65, 80 and 120 nm) and wall thicknesses in the range 8–14 nm. The as-prepared samples were characterized and then annealed at 450 °C in air for 2 h. The surface morphology of the samples is characterized by field emission scanning electron microscopy which reveals uniformly distributed nanotube arrays over the substrate. Raman scattering measurements show that the NTs in as-prepared samples are amorphous. In annealed samples rutile phase and a small amount of anatase phase are detected by both Raman scattering and X-ray diffraction methods. It is assumed that the rutile phase is related to a TiO_2 film with rutile structure formed during the annealing between NTs and alloy substrate. The retarded formation of anatase phase is connected with inclusion in the TiO_2 nanotubes of external atoms coming from the substrate. The amount and crystallinity of anatase phase decreases with decreasing nanotube diameter and/or wall thickness which is assigned to size-induced increase of the NT crystallization temperature. Investigations of the optical response of the samples to ethanol vapors at room temperature reveal relations between the NT size and their ethanol sensitivity. The response of as-prepared nanotube arrays increases with decreasing nanotube diameter while in the annealed samples an opposite trend is observed. The size dependence seen for as-prepared samples is related to an increase of the total adsorbing surface with decreasing NT diameter. The result obtained for the annealed samples is assigned to annealing induced changes in the morphology and composition of the internal surface of NTs.

1. Introduction

Titanium dioxide (TiO_2) nanotubes grown on Ti foil have high specific surface area, good ion-exchangeable ability, and photocatalytic properties. Therefore they are very actively investigated for various potential applications as catalysts, hydrogen generators, corrosion resistant and electro chromic materials, in solar cells, etc. [1–7]. NTs on Ti alloys, such as Ti6Al4V, Ti6Al7Nb, have also attracted much attention for application in the biomedical field [8–12].

Synthesis of quasi one-dimensional TiO_2 nanostructures may be achieved by various methods [1,2,7]. Among them the electrochemical oxidation of a metallic titanium substrate under a specific set of experimental conditions is most widely used since it results in fabrication of spectacular self-organized TiO_2 nanotube layers [13–16]. A good control of the NTs' diameter, length, wall thickness and spacing has been achieved [2,5–7,17,18]. Significant attention has also been given to the effects of thermal annealing on crystal phases (amorphous, anatase, rutile) in TiO_2 NTs prepared by electrolytic anodization [5,9,18]. The nanotubes obtained by

* Corresponding author.
E-mail address: nesheva@issp.bas.bg (D. Nesheva).

https://doi.org/10.1016/j.jallcom.2019.05.247
0925-8388/

anodization process are normally amorphous and by applying annealing at different temperatures one can obtain different proportions of anatase and rutile phase in NTs [19]. The annealing of TiO_2 nanotubes under oxidizing conditions results in the formation of anatase crystal structure in the temperature range of 300–500 °C, while at temperatures around 600 C, a mixture of anatase and rutile phase is detected in NTs [20]. Some authors reported that when the annealing is carried out at around 450 °C or higher temperatures a relatively thick TiO_2 rutile layer grows underneath the tube layers [18,20,21]. For various applications of anodically prepared TiO_2 NTs it is important to have information about the existence and thickness of such rutile layer since it affects the samples' resistivity. Formation of anatase and rutile TiO_2 layers on the surface of Ti6Al4V disks has also been reported upon thermal oxidation treatment at temperatures greater than 200 °C and 400 °C, respectively [22]. Important feature of TiO_2 NTs is the possibility to apply various approaches such as metal [2,18] and non-metal [23–25] doping, TiO_2 reduction [26,27], growth on Ti substrates of different crystallographic orientations [28], additional coating with secondary materials [29], etc. in order to modify properties of TiO_2 nanotube layers and thus to make them suitable for a particular type of application. An efficient way for TiO_2 NT doping is the anodization of Ti-alloys.

Undoped and doped TiO_2 nanostructured materials attract much attention as promising materials for sensor applications. It has been shown that the quasi one-dimensional TiO_2 structures with their large surface area and high porosity have better gas sensing performance in comparison with dense nanoparticle aggregates [30] and TiO_2 NT layers are actively studied for the fabrication of chemical sensors [30,31]. Resistance changes [30–33] have been mostly measured when investigating the nanotubes' chemical sensing properties. Metal-oxide-semiconductor structures * with TiO_2 nanotube arrays [34,35] have also been subject of investigations. The research and development in the optical sensor field is also attractive since optical sensors have some significant advantages compared to conventional resistive sensors, such as greater sensitivity, electrical passiveness, freedom from electromagnetic interference, multi-gas detection using differences in the intensity, wavelength, phase and polarization of the output light signals etc. [36]. Since TiO_2 nanotube arrays prepared by anodic oxidation have a large active surface area and better stability for wide pH range solutions than usually used label free interferometric biosensor from nanoporous silicon or silica they are intensively studied as interferometric biosensing materials [37–41]. The sensing principle is based on a change of the mean refractive index of the NT structure when molecular species are bonded in the inner part of the nanotubes and this leads to a wavelength shift in the interference pattern detected. Well defined optical interference patterns have been obtained in double-layer tube arrays formed by corrugated stacked TiO_2 nanotubes and a top-protective tube layer [38]. An advantage of using TiO_2 NT based interference stacks for sensing is that the photocatalytic properties of TiO_2 make the interferometric sensor reusable after a short UV treatment. To the best of our knowledge, the investigations on optical response of TiO_2 NTs arrays to chemical agents are quite limited. TiO_2 nanotube arrays have been used in photonic crystal based optical sensors and experiments on its sensing behavior have been carried out with different agents: air, deionized water, ethanol and isopropanol [42,43]. Changes in reflectance [42] or diffraction [43] spectra have been detected upon exposure to the chemical agent.

In this study, the anodic oxidation method is applied for the preparation of TiO_2 nanotube arrays of four different internal diameters and wall thicknesses on Ti6Al4V alloy substrates and the samples are further annealed at 450 °C in air. Ti-alloy is used to get NT doping during the growth and to study the effect of such doping on the phase composition and sensing properties of the samples. The morphology of the sample surfaces is characterized by field emission scanning electron microscopy (SEM), while the NT crystallinity and annealing induced changes are explored by Raman scattering and X-ray-diffraction (XRD) measurements. The optical response to ethanol vapors of as-prepared and annealed TiO_2 nanotube arrays is investigated at room temperature and size related sensitivity is observed.

2. Materials and methods

Discs of Ti6Al4V (ASTM F-136; Supra Alloys Inc., Camarillo, CA, USA) with a 1.5 cm^2 surface area were polished using SiC emery paper (120–1500 grit) and 50 nm alumina for finishing. Mirror finish disc substrates were mounted on a special flat 125 mL cell and electrochemically anodized using Microdacyn 60® superoxidized water (SOW) (Oculus Technologies, Guadalajara, JAL, Mexico), ammonium fluoride (NH_4F) (Sigma-Aldrich, USA) and ethylene glycol. TiO_2 nanotubes with different diameters and thicknesses were grown by varying the ethylene glycol/superoxidized water ratio, anodization time and potential. The samples were obtained using two types of solutions (Table 1) under the conditions given in Table 2. Voltages of 10 V and 20 V were used for each solution. The process was carried out at room temperature. Finally, the discs were cleaned in an ultrasonic bath with distilled water for 5 min to eliminate residues of fluoride salts [44], rinsed with isopropyl alcohol and dried in a desiccator for 12 h. After the characterization of as-prepared NTs, the samples were furnace annealed at 450 °C for 2 h in air. A slow sample's heating (heating rate of around 4 °C/min) up to 450 °C and cooling down to room temperature was applied in order to preserve the order of the NT arrays.

The morphology of the sample surfaces was analyzed by scanning electron microscopy using a field-emission scanning electron microscope (FE-SEM) Tescan LYRA 3, Brno, Czech Republic. The elemental composition of the nanotubes was determined by Energy Dispersive X-ray Spectroscopy (EDS). To eliminate the Al and V contribution from the Ti6Al4V substrate nanotubes were peeled off from the substrate using scotch tape and placed on carbon tape and Cu foil. The copper foil ensures that no contribution from the Al stage of the microscope is included in the measured spectra. Similar values for the Al concentration were obtained in both types of measurements.

XRD and Raman scattering measurements were carried out to get information about the phase composition of the nanotubes. The X-ray analysis of samples was accomplished using Cu Kα radiation at room temperature. Both glancing incidence (GI) mode at an angle of incidence $\alpha = 0.5°$ and the Bragg–Brentano (BB) mode were applied via the step method at 0.2° steps (2θ, θ – diffraction angle) by means of PANalytical Empyrean and Bruker D8 Advance X-ray diffractometer, respectively. The Raman measurements were performed at room temperature in air with a spectral resolution of 2.0 cm^{-1}. Jobin-Yvon T64000 triple spectrometer equipped with a confocal microscope and a N_2-cooled CCD detector in backscattering geometry was used. The samples were excited by VerdiTM G-Series optically pumped semiconductor laser operating at

Table 1
Electrolytic solutions used in the anodization process.

Solution	NH_4F [g]	Ethylene glycol [ml]	SOW [ml]
1	0.5	25	75
2	0.5	50	50

Table 2
Experimental conditions used for growing of nanotubes.

Sample	Solution	Voltage [V]	Time [min]
1	1	10	20
2	1	20	20
3	2	10	5
4	2	20	15

532 ± 2 nm, with output laser power less than 20 mW to minimize local heating effects due to irradiation.

The sensing behavior of samples was studied by reflectance measurements prior to and after exposure to ethanol vapors. Accordingly the samples were placed in a quartz cell and reflectance spectra were recorded by a UV-VIS-NIR spectrophotometer (Cary 5E, Varian) at one and the same spot of the sample when air and ethanol vapors were alternatively purged into the cell. The ethanol vapors were generated by a home-made bubbler system described in details elsewhere [45].

3. Results and discussion

3.1. Surface morphology and phase characterization

SEM micrographs of the surface of four as-prepared samples produced under the conditions given in Table 2 and the cross-sections of these samples are shown in Fig. 1. The micrographs reveal presence of uniform nanotube arrays distributed over the alloy substrate, which are open at the top surface. The average values of internal diameter, wall thickness and NT layer thickness of the four types of samples are given in Table 3. The NT diameters and layer thicknesses depend on the electrolyte solution and increase with the anodization potential. The wall thickness also shows a slight increase with the NT diameter. Our SEM investigations have shown that the order of NT array was not appreciably affected by an annealing in air at 450 °C for 2 h, which is in agreement with the results known from the literature [2].

EDS spectra were collected from all types of nanotubes on carbon tape. Peaks indicating presence of Ti, O, Al, C and Si have been observed while vanadium was not detected (see the Supplementary data, Fig. S1.1.). The obtained concentrations in weight percent are given in Table 4. No substantial variation of the Al concentration is observed in nanotubes grown under different anodization conditions. The C and Si signals in the spectrum resulted from the carbon tape. The obtained result may be explained taking into account that the ammonium fluoride dissolves the Al_2O_3 formed during the anodization and leads to a smaller Al concentration in

Table 3
Average values of internal diameter, wall thickness and NT layer thickness of the four types of samples.

Sample	Diameter [nm]	Thickness [nm]	Wall thickness [min]
1	60	338	8–9
2	65	481	8–12.5
3	80	373	10–13
4	120	497	12–14.5

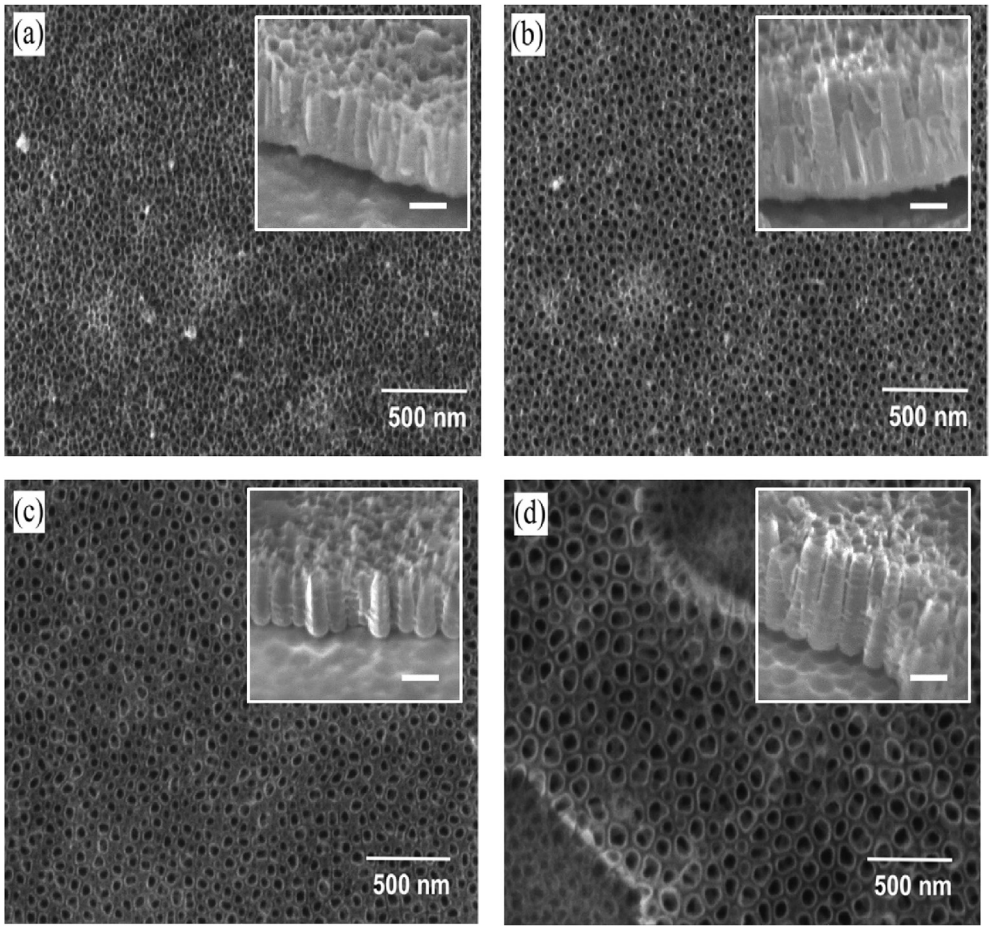

Fig. 1. SEM images of top view of the four types of as-prepared TiO_2 NT samples; the insets show their cross-sections. The scale bar in the insets is 200 nm.

Table 4
Concentration of the different elements for all types of samples obtained from EDS results.

No	NT diameter	Ti	O	Al	C	Si
1	60	48.5	38.8	1.9	10.5	0.3
2	65	49.4	32.2	3.3	14.4	0.7
3	80	48	39	3	8	1.6
4	120	47.6	38.4	1.9	11.5	0.6

the NTs than in the Ti6Al4V alloy substrates. One can assume that the vanadium disaggregates from the alloy and was eliminated during the anodization and sonication.

Fig. 2(a) and (b) show XRD patterns of the NT samples after annealing in air at 450 °C, measured in GI and BB, respectively. The three diffraction peaks seen in the 2θ range 35°- 41° and the peak at 53.3° correspond to diffraction from the not anodized part of the Ti6Al4V discs. These bands are slightly shifted to higher angles with respect to the positions of pure titanium but their disposal perfectly coincide with that reported for commercial Ti6Al4V [46]. Two weak peaks are also seen in Fig. 2(a) at $2\theta \approx 25°$ and 27.5° which reveal existence of anatase and rutile phase, respectively. The peak at 27.5° is better resolved while that at 25°, assigned to anatase phase, is hardly seen which indicates existence of quite small amount of anatase phase. A peak at $2\theta = 54.4°$ is also observed which can be due to both anatase and rutile phases but in Fig. 2(a) its center corresponds to XRD from rutile TiO_2. The irradiated volume in the BB mode is higher than that in the GI mode [47]. Therefore in the patterns collected in BB mode (Fig. 2(b)) the bands corresponding to the bulk Ti6Al4V alloy are significantly stronger than those in Fig. 2(a) and the band at $2\theta = 54.4°$ is not resolved, but the bands at around 25° and 27.5° are better noticeable. A number of research groups have reported that during annealing of TiO_2 NTs anodically grown on Ti substrates at temperatures higher than 450 °C a TiO_2 layer with rutile structure is formed at the nanotube-metal interface [18,20,21,48]. One can relate the slight intensity increase of the band at 27.5° observed in BB mode to more effective X-ray diffraction from such a layer.

Why the amount of anatase phase in NTs of all diameters/wall thicknesses is small? Results reported by many authors for NTs TiO_2 anodically grown on pure titanium plates have indicated that the annealing of NTs at temperatures in the range 400 °C-500 °C normally leads to significant NT crystallization and growth of TiO_2 nanocrystals with anatase structure located in the NT walls. Rutile phase appears in the NTs at temperatures higher than 500 °C [2]. The nanotubes doping with Nb, Al, Ni, Ga, Ta, and W retards the growth of anatase and rutile crystallites and delays the anatase-to-rutile phase transformation while Mn, Fe, Cu, and Zn are generally believed to promote the phase transformation [2 and references therein]. The rather small amount of anatase phase detected by the XRD measurements in the samples annealed at 450 °C can be related to the inclusion of aluminium atoms from the substrate during the NT growth. Most likely, because of the difference in the Al^{3+} and Ti^{4+} ionic radii the Al inclusion causes a disorder increase [49] which retards crystallization and causes an increase of the crystallization temperature.

Raman scattering spectroscopy allows to explore the phases in TiO_2 NTs with a better sensitivity than XRD one. Observation of Raman scattering bands at around 144 cm^{-1} (E_g mode), 197 cm^{-1} (E_g mode), 395 cm^{-1} (B_{1g} mode), 516 cm^{-1} (A_{1g} + B_{1g} mode), 639 cm^{-1} (E_g mode) is expected for the TiO_2 anatase phase, while the bands characteristic for the rutile phase appear at around 447 cm^{-1} (E_g mode) and 615 cm^{-1} (A_{1g} mode). Fig. 3 shows characteristic Raman spectra of samples with all NT diameters taken before (Fig. 3(a)) and after (Fig. 3(b)) annealing. The spectra obtained before annealing are structureless; the result is in agreement with the observations of other authors and indicates that NTs in all as-prepared samples are amorphous [50–52].

Optical images of the surface of annealed samples, taken by the Raman system, revealed regions of different colors (see the Supplementary data, Fig. S2.1) and therefore the Raman measurements were carried out at spots of different colors. Obtained spectra reveal that in the sample with the smallest nanotube diameter, 60 nm, only rutile TiO_2 phase is registered at almost all measurement locations. The most intensive anatase E_g Raman mode, measured at all locations (see the Supplementary data, Fig. S2.2) is significantly blue shifted in comparison to the corresponding bulk value and their position is influence by the surface color. This influence could be related to more or less pronounced nonstoichiometry.

In the Raman spectra recorded on the other three samples modes characteristic for both anatase and rutile phases are regularly detected. It can be clearly seen from Fig. 3(b) that the intensities of anatase modes increase, whereas the intensities of rutile modes, not only relative, but also absolute, lightly decrease with increasing NT diameter and wall thickness. The increase of anatase Raman modes intensity indicates the improvement of anatase crystallinity with increasing NT diameter and wall thickness, but the behavior of rutile modes is not entirely clear. Namely, in contrast to the rutile Raman modes, the XRD patterns do not show significant change in the intensity of diffraction peaks related

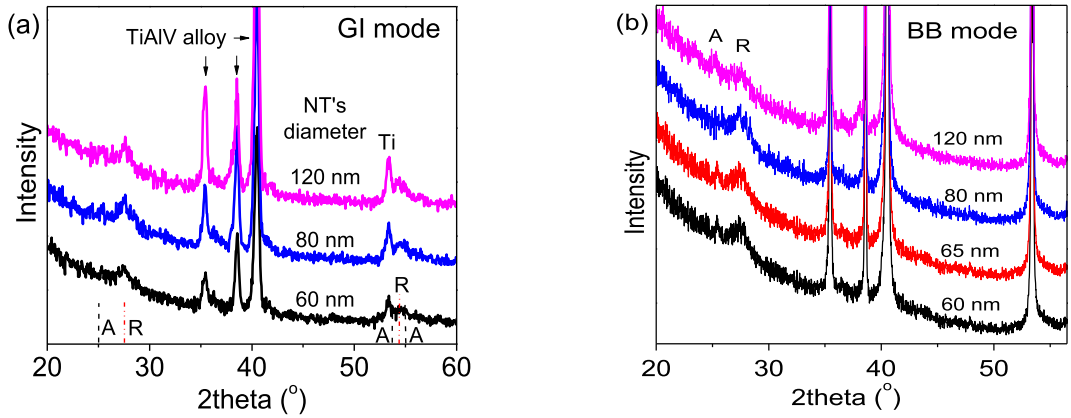

Fig. 2. XRD patterns of TiO_2 NT samples annealed at 450 °C for 2 h with diameters denoted in the figures. The patterns were registered in: (a) GI mode and (b) BB mode. The XRD pattern in both figures are shown in the same *y*-scale and patterns are vertically shifted upwards for clarity. The dashed lines in (a) mark positions of XRD peaks related to diffraction from anatase phase (A), whereas the dash-dot-dot lines mark peak positions corresponding to rutile phase (R).

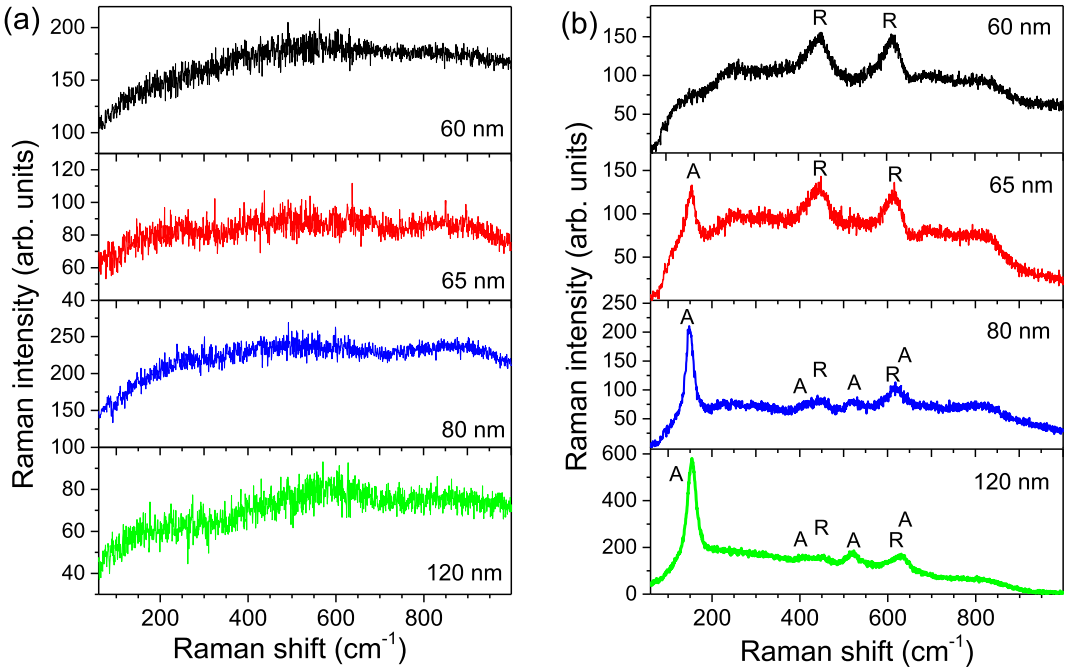

Fig. 3. Raman scattering spectra of as-prepared (a) and annealed (b) TiO_2 NTs with four diameters and wall thicknesses, which were anodically grown on Ti6Al4V discs.

to rutile phase with the NTs diameters. The decrease of Raman intensity of rutile modes with increasing NTs diameter could be the consequence of higher absorption of visible light in NTs with larger diameters, possibly due to larger amount and better crystallinity of anatase phase in those NTs [53] (see also the Supplementary data, Fig. S3.1 and S3.2). This implies that rutile phase may rather be located at the Ti6Al4V substrate/NT interface than in the NTs walls.

Literature data on the influence of NTs diameter and/or wall thickness on the structure of TiO_2 nanotubes is quite limited and controversial. Diameter dependent anatase/rutile stabilization has been studied on TiO_2 nanotubes grown on pure titanium foils [54]. Upon NT annealing at 450 °C the formation of rutile was observed for tube diameters <30 nm, whereas for larger diameters anatase was formed. This effect has been related to the presence of the metallic substrate; in its absence formation of anatase phase was observed in tubes with all diameters. Other authors have reported that they convert amorphous nanotubes with diameters in the range 21–95 nm grown on pure Ti substrates to anatase nanotube layers by applying an annealing at 400 °C for 1 h in air [55]. Also, it has been registered that the increase of anodization potential, followed by the increase of NTs diameter, promotes formation of anatase crystalline structure after annealing at 500 °C for 2 h [56]. Namely, it has been found that the samples with NT diameter of 80 nm consisted of anatase phase only, rutile appeared in NTs with <80 nm, whereas in 20 nm NTs there was no indication of anatase phase. Our conclusion that after annealing the crystallinity of anatase structures in the walls of Al-doped NTs is improving with the increase of the NT diameter, whereas the rutile phase is located inside the layer at the interface between NTs and metal substrate could be in agreement with some of the findings for undoped NTs. As mentioned previously, anatase phase has been hardly detected by Raman scattering measurements of NTs with diameter of 60 nm (at very few measurement locations). The difficulties in detecting modes related to anatase phase in Raman spectra of annealed NT with diameter of 60 nm and wall thickness estimated about 8–9 nm, may indicate lower crystallinity of anatase in this sample in comparison to the NTs with the larger diameters and wall thicknesses 9–14 nm (see section 3.1). This could point to the possibility that, beside NT diameter, its wall thickness may also have some influence to anatase crystallization in the NTs.

Crystallization (nucleation and crystal growth) of amorphous films is a complicated process. A number of factors can affect the crystallization temperature of an amorphous thin film: thickness, interfacial energy effects, stress (which normally increases with decreasing film thickness and inhibits further crystallization [57]), crystallization kinetics, substrate lattice parameter, structure, cleanness, ambient of annealing, etc. The thickness-dependent crystallization behavior of an amorphous thin film cladded between different layers can be modelled thermodynamically and such modeling has been used to explain the observed effect of the layer thickness on the crystallization temperature, T_c, of nanolayers in amorphous multilayers [58]. It has been shown for the crystallization process in amorphous multilayers consisting of two consecutively deposited amorphous semiconductors [59] that the layer thickness and the interface energies together with the crystallization temperature of the thick amorphous layer are key factors for determining the crystallization temperature of nanosized layer. A T_c increase by approximately 300 K has been reported for multilayers with amorphous Si when the Si layer thickness was reduced to 2 nm [60]. Similarly an increase of the crystallization temperature of amorphous a-Ge films in a-Ge based multilayers has been observed with decreasing layer thickness [61]. In order to explain the improvement of the crystallinity of anatase phase with increasing wall thickness we adopt the idea that during annealing anatase nanocrystals grow in the walls of as-prepared amorphous TiO_2 NTs which could be considered as cylindrical layers separated by the contact interface regions (with different properties from the layers). The wall thickness of NTs may affect their crystallization temperature for similar reasons as in amorphous multilayers.

Knowing that the nanocrystals cannot grow larger than the NT wall thickness during the annealing process (at least in radial direction otherwise the NT order would be destroyed) the phonon confinement effects in anatase nanocrystals should be taken into account in the analysis of their Raman spectra. The phonon

confinement in anatase TiO_2 nanocrystals causes a blue shift of its most intensive E_g mode, as well as asymmetric broadening in comparison to the bulk TiO_2 [62]. In Fig. 4 typical experimentally obtained Raman feature ascribed to the most intensive anatase E_g mode (centred at 154 cm^{-1}) is compared with modes simulated by phonon confinement model for anatase nanocrystals with uniform particle size (6–50 nm) without lattice strain and oxygen non-stoichiometry included in the calculations. It can be seen that this feature is strongly shifted even in comparison to mode calculated for uniform particle size of 6 nm (supposedly smaller than the thinnest NT wall) and broadened, but with the shape more symmetric than expected for the influence of pure phonon confinement. Based on this comparison, as well as our previous research [62,63], Raman shift, broadening and shape of E_g mode in experimental Raman spectra of NTs could also be influenced by anatase lattice strain and nonstoichiometry, as well as the anharmonicity due to possible local heating during the measurement. In this research certain variations of the E_g Raman shift and linewidth in the spectra were measured at different locations of the same sample, which may be correlated to different shades of blue color of the sample surface [64] (see the Supplementary materials). This could indicate that the blue color originates from oxygen deficiency (nonstoichiometry) in anatase phase [65] and such deficiency may be one of the reasons for relatively great blue shift of E_g mode. Note also that more appropriate simulation of experimental Raman data could be obtained by the phonon confinement model which includes the influence of lattice strain due to nonuniform particle size distribution of anatase nanocrystals in NT wall.

In order to investigate whether applied laser irradiation during the measurements produce local heating of the sample, with influence on Raman spectra of anatase, the experiments with various output laser powers in the range 3 mW–60 mW were carried out. No significant shift and broadening of the most intensive anatase E_g mode due to the laser heating effect have been registered at output laser power less or equal to 20 mW, whereas at laser power of 60 mW an additional blue shift of ~2 cm^{-1} as well as slight broadening of E_g anatase mode occurred.

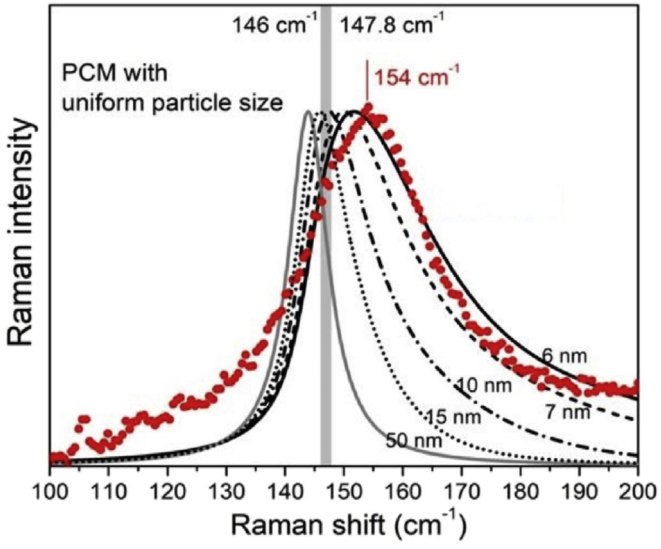

Fig. 4. The part of the experimental Raman spectrum (dotted line) of NT with diameter of 120 nm compared to the most intensive E_g Raman mode simulated by phonon confinement model for chosen uniform nanoparticles between 6 and 50 nm.

3.2. Optical sensing of ethanol vapors

Typical reflectance spectra of the NT samples are shown in Fig. 5. They were consecutively measured in air, argon atmosphere (99%), ethanol vapors in Ar, argon atmosphere and again upon exposure to ethanol vapors. All curves do not show any features which indicates that the samples' surface is smooth. The curves taken in air and argon practically coincide. The exposure to ethanol vapors causes a reflectance decrease in the wavelength range 450–650 nm. For each sample the relative difference $\Delta R = (R_{air} - R_{eth})/R_{air})$ between the measured reflectance in air (R_{air}) and ethanol (R_{eth}) is taken at the wavelength where this difference is the largest. Thus for the sample with average tube diameter of 60 nm, presented in Fig. 5, the wavelength is 510 nm. For samples with tube diameters of 65 nm, 80 nm and 120 nm the selected wavelengths are 502 nm, 626 nm and 600 nm, respectively.

Fig. 6 shows relative change of reflection coefficient for as-prepared (amorphous) TiO_2 NT samples as a function of the diameter of nanotubes for two cycles of exposure to ethanol vapors. A clear size dependence is seen; the sample sensitivity increases with decreasing NT diameter. The observed changes of the film reflectance are related to the amount of the ethanol molecules adsorbed on the active surface of the nanotubes, which is much higher than the geometric sample surface. Taking into account that the 'active surface'- to -'geometric surface' ratio increases with decreasing NT diameter, as well as that NTs with all diameters are amorphous, one can explain the size dependence seen in Fig. 6 with the size-related increase of the active NT surface.

It is seen from Fig. 6 that for all samples, except that with the smallest NT's diameter, the response is nearly the same for the two measured cycles. However, the sensitivity for the second cycle of the sample with NT's diameter of 60 nm is slightly smaller as compared to that in the first cycle. Therefore a seven cycles experiment was carried out on the sample with the highest sensitivity and the result is depicted in Fig. 7. It is seen that equilibrium is reached after the third cycle and no further sensitivity decrease occurs which makes these samples suitable for optical ethanol sensors.

Fig. 8 shows relative change of reflection coefficient for TiO_2 NT samples annealed at 450 °C for 2 h in air as a function of the diameter of nanotubes for exposure to ethanol vapors. A comparison with Fig. 6 indicates that: (i) the sensitivity of the annealed

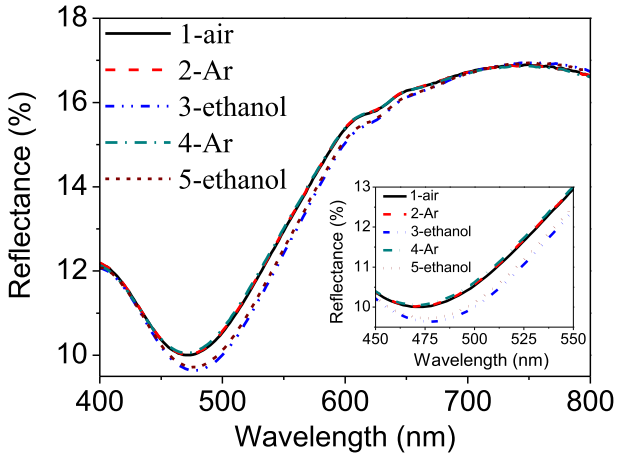

Fig. 5. Reflectance spectra of TiO_2 NT as-prepared samples with nanotubes diameter of 60 nm measured consecutively in various atmospheres noted in the figure. The magnified part of the figure around the largest changes is shown as an inset. The first measurement (curve 1) is in air, the last one (curve 5) is the second measurement in ethanol vapors. Curves 1, 2 and 4 practically coincide.

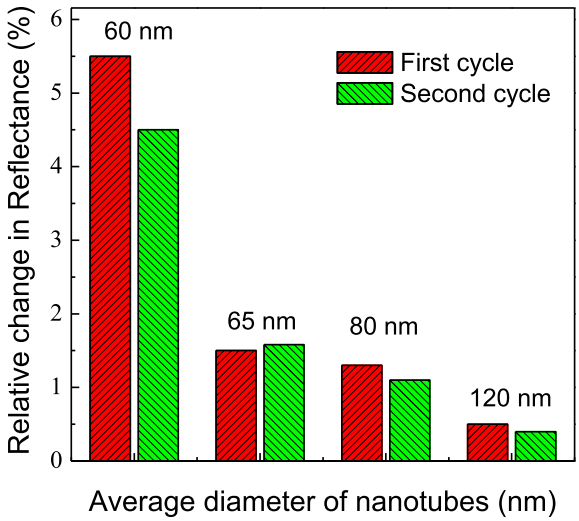

Fig. 6. Relative change of reflection coefficient for TiO_2 NT as-prepared samples versus diameter of nanotubes (taken from SEM images) for two cycles of exposure to ethanol vapors.

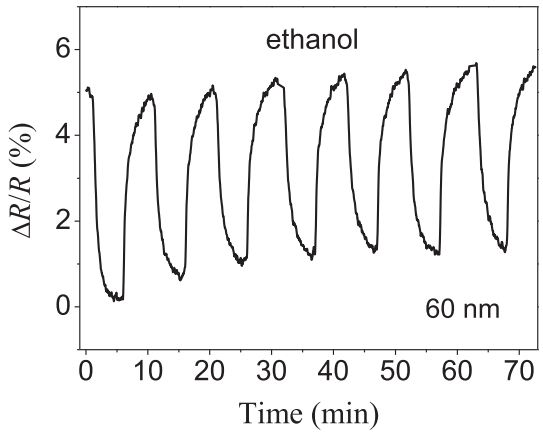

Fig. 7. Relative changes of reflection coefficient for as-prepared TiO_2 NT with diameter of 60 nm for seven cycles of exposure to ethanol vapors.

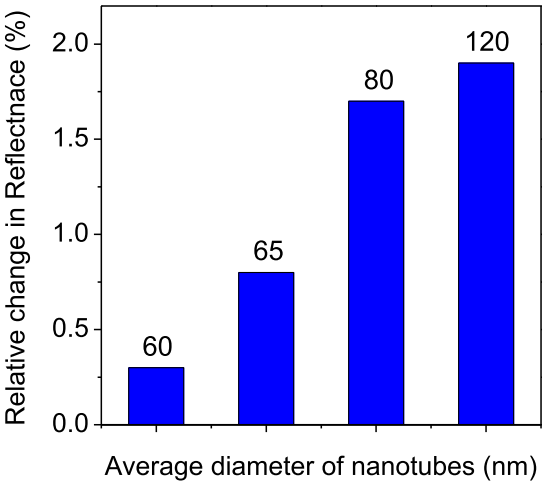

Fig. 8. Relative change of reflection coefficient for TiO_2 NT samples annealed at 450 °C for 2 h in air versus diameter of nanotubes over one cycle of exposure to ethanol vapors.

samples with diameter of 60 nm and 65 nm is significantly lower than the sensitivity of the as-prepared ones and (ii) a size dependence of the sensitivity is also observed but it is opposite to that observed in Fig. 6 for the as-prepared samples. Since the SEM results have not shown appreciable deterioration of the NT quality by the annealing, one can expect that the real NT surface was not significantly changed. In addition, the Raman scattering data have indicated variations of anatase crystal structure with NTs diameter/wall thickness, as well as variation in nonstoichiometry (due to oxygen deficiency) within each sample, which may also influence the morphology of internal surface of the nanotubes. The size dependence seen in Fig. 8 i.e. the higher sensitivity of the samples with NTs of larger diameters, can be related to observed increase of the amount and/or crystallinity of anatase phase with increasing NTs diameter. The decrease of sensitivity of nanotubes with diameter of 60 nm and 65 nm induced by the annealing might be the consequence of formation of oxygen vacancies and other compositional changes at the surface of TiO_2 NTs taking place upon annealing due to presence of incorporated aluminum atoms. For example the Al—O bond dissociation energy (501.9 kJ/mol) is smaller than the Ti—O bond dissociation energy (666.5 kJ/mol) [66]. If the Al atoms occupy positions of Ti atoms in the TiO_2 crystal lattice the annealing at 450 °C may result in formation of oxygen vacancies which do not exist in the as-grown NTs.

4. Conclusions

Arrays of TiO_2 nanotubes with four different internal diameters (60, 65, 80 and 120 nm) have been grown on Ti6Al4V alloy substrates by anodic oxidation. FE-SEM investigation of the surface morphology of as-prepared samples has shown that nanotubes are uniformly distributed over the Ti6Al4V surface and open on the top. Raman scattering results have revealed that TiO_2 NTs in as-prepared samples are amorphous. The X-ray diffraction and Raman scattering data obtained from annealed NT samples have detected rutile phase and quite small amount of anatase phase. It has been concluded that the detected rutile phase is mainly related to formation of TiO_2 layer with rutile structure during samples annealing; the layer is located at the interface between NTs and Ti6Al4V alloy substrate. The retarded NT crystallization and formation of rather small amount of anatase phase in NTs has been ascribed to incorporation of Al atoms in the NTs during their growth, which causes a disorder increase and an increase of the crystallization temperature T_c. A decrease of the crystallinity and/or amount of anatase phase with NTs diameters and wall thicknesses decreasing has been observed and related to size induced increase of the crystallization temperature, which is similar to the T_c increase observed in amorphous superlattices.

The optical response to ethanol vapors of as-prepared and annealed samples investigated at room temperature have revealed an effect of NT diameter in both groups of samples. The response of the as-prepared (amorphous) nanotube arrays increases with decreasing nanotube diameter which has been related to an increase of the real NT surface. It has been shown that after the third cycle of exposure to ethanol vapors the sensitivity of these samples keeps constant which makes them suitable for ethanol optical sensing. In the group of annealed sample the sensitivity increases when the nanotube diameter increases and this observation has been assigned to annealing induced changes in the NTs surface morphology and the crystallinity of anatase phase inside the NT walls.

Declarations of interest

None.

Acknowledgements

This work was partially supported by the European Regional Development Fund within the OP "Science and Education for Smart Growth 2014 - 2020", project № BG05M2OP001-1.001-0008-C01, under a grant within a bilateral project between the Bulgarian Academy of Sciences and Serbian Academy of Sciences and Arts, as well as under Project III45018 of the Ministry of Education, Science, and Technological Development of Republic of Serbia.

Appendix A. Supplementary data

Supplementary data to this article can be found online at https://doi.org/10.1016/j.jallcom.2019.05.247.

References

[1] T. Sekino, Synthesis and applications of Titanium oxide nanotubes, in: T. Kijima (Ed.), Inorganic and Metallic Nanotubular Materials. Topics in Applied Physics (2010), vol. 117, Springer-Verlag, Berlin Heidelberg, 2010, pp. 17–32, https://doi.org/10.1007/978-3-642-03622-4 2.

[2] P. Roy, S. Berger, P. Schmuki, TiO_2 nanotubes: synthesis and applications, Angew. Chem. Int. Ed. 50 (2011) 2904–2939.

[3] M. Pelaez, N. Nolan, S. Pillai, M. Seery, P. Falaras, A.G. Kontos, P.S.M. Dunlop, J.W.J. Hamiltone, J.A. Byrne, K. O'Shea, M.H. Entezari, D.D. Dionysiou, A Review on the visible light active Titanium dioxide photocatalysts for environmental applications, Appl. Catal. B Environ. 125 (2012) 331–349, https://doi.org/10.1016/j.apcatb.2012.05.036.

[4] S. Bhardwaj, T. Rana, P. Laha, A. Barman, S. Biswas, Study of Titanium dioxide nanotube array for the application in dye-sensitized solar cells, Int. J. Mach. Mach. Mater. 2 (2014) 47–50.

[5] V. Galstyan, A. Vomiero, I. Concina, A. Braga, M. Brisotto, E. Bontempi, G. Faglia, G. Sberveglieri, Vertically aligned TiO_2 nanotubes on plastic substrates for flexible solar cells, Small 7 (2011) 2437–2442, https://doi.org/10.1002/smll.201101356.

[6] I. Paramasivam, H. Jha, N. Liu, P. Schmuki, A review of photocatalysis using self-organized TiO_2 nanotubes and other ordered oxide nanostructures, Small 8 (2012) 3073–3103, https://doi.org/10.1002/smll.201200564. Epub 2012 Sep. 10.

[7] K. Lee, A. Mazare, P. Schmuki, One-dimensional titanium dioxide nanomaterials: nanotubes, Chem. Rev. 114 (2014) 9385–9454, https://doi.org/10.1021/cr500061m.

[8] J.M. Macak, H. Tsuchiya, L. Taveira, A. Ghicov, P. Schmuki, Self-organized nanotubular oxide layers on Ti-6Al-7Nb and Ti-6Al-4V formed by anodization in NH4F solutions, J. Biomed. Mater. Res. A. 75 (2005) 928–933, https://doi.org/10.1002/jbm.a.3050.

[9] Ch. J. Frandsen, K.S. Brammer, S. Jin, Variations to the nanotube surface for bone regeneration, Int. J. Biomater. 2013 (2013) 513680–513710, https://doi.org/10.1155/2013/513680.

[10] K.M. Kummer, E.N. Taylor, N.G. Durmas, K.M. Tarquinio, B. Ercan, T.J. Webster, Effects of different sterilization techniques and varying anodized TiO_2 nanotube dimensions on bacteria growth, J. Biomed. Mater. Res. B Appl. Biomater. 101 (2013) 677–688. https://doi.org/10.1002/jbm.b.32870.

[11] E. Beltrán-Partida, B. Valdez-Salas, A. Escamilla, M. Curiel, E. Valdez-Salas, N. Nedev, J.M. Bastidas, Disinfection of titanium dioxide nanotubes using super-oxidized water decrease bacterial viability without disrupting osteoblast behavior, Mater. Sci. Eng. C 60 (2016) 239–245, https://doi.org/10.1016/j.msec.2015.11.042.

[12] E. Beltrán-Partida, B. Valdez-Salas, M. Curiel-Álvarez, S. Castillo-Uribe, A. Escamilla, N. Nedev, Enhanced antifungal activity by disinfected titanium dioxide nanotubes via reduced nano-adhesion bonds, Mater. Sci. Eng. C 76 (2017) 59–65, https://doi.org/10.1016/j.msec.2017.02.153.

[13] J.M. Macak, H. Tsuchiya, A. Ghicov, K. Yasuda, R. Hahn, S. Bauer, P. Schmuki, TiO_2 nanotubes: self-organized electrochemical formation, properties and applications, Curr. Opin. Solid State Mater. Sci. 11 (2007) 3–18, https://doi.org/10.1016/j.cossms.2007.08.004.

[14] A. Ghicov, P. Schmuki, Self-ordering electrochemistry: a review on growth and functionality of TiO_2 nanotubes and other self-aligned MO_x structures, Chem. Commun. 0 (issue 20) (2009) 2791–2808, https://doi.org/10.1039/B822726H.

[15] S. Ozkan, A. Mazare, P. Schmuki, Critical parameters and factors in the formation of spaced TiO_2 nanotubes by self-organizing anodization, Electrochim. Acta 268 (2018) 435–447. https://doi.org/10.1016/j.electacta.2018.02.120.

[16] C.A. Grimes, Synthesis and application of highly ordered arrays of TiO_2 nanotubes, J. Mater. Chem. 17 (2007) 1451–1457, https://doi.org/10.1039/B701168G.

[17] S. Ozkan, N.T. Nguyen, A. Mazare, I. Cerri, P. Schmuki, Controlled spacing of self-organized anodic TiO2 nanotubes, Electrochem. Commun. 69 (2016) 76–79, https://doi.org/10.1016/j.elecom.2016.06.004.

[18] F. Riboni, N.T. Nguyen, S. So, P. Schmuki, Aligned metal oxide nanotube arrays: key-aspects of anodic TiO_2 nanotube formation and properties, Nanoscale Horiz. 1 (2016) 445–466, https://doi.org/10.1039/C6NH00054A.

[19] D. Regonini, A. Jaroenworaluck, R. Stevens, C.R. Bowen, Effect of heat treatment on the properties and structure of TiO_2 nanotubes: phase composition and chemical composition, Surf. Interface Anal. 42 (2010) 139–144, https://doi.org/10.1002/sia.3183.

[20] S. Das, R. Zazpe, J. Prikryl, P. Knotek, M. Krbala, H. Sopha, V. Podzemna, J.M. Macak, Influence of annealing temperatures on the properties of low aspect-ratio TiO_2 nanotube layers, Electrochim. Acta 213 (2016) 452–459, https://doi.org/10.1016/j.electacta.2016.07.135.

[21] S.P. Albu, H. Tsuchiya, Sh. Fujimoto, P. Schmuki, TiO_2 nanotubes – annealing affects on detailed morphology and structure, Ber. Dtsch. Chem. Ges. Spec. Issue One Two-Dimens. Inorg. Nanomater. 2010 (Cluster Issue) (2010) 4351–4356, https://doi.org/10.1002/ejic.201000608.

[22] A. Butt, A. Hamlekhan, S. Patel, D. Royhman, C. Sukotjo, M.T. Mathew, T. Shokuhfar, Ch. Takoudis, A novel investigation of the formation of Titanium oxide nanotubes on thermally formed oxide of Ti-6Al-4V, J. Oral Implantol. XLI (2015) 523–531, https://doi.org/10.1563/AAID-JOI-D-13-00340.

[23] G. Wu, T. Nishikawa, B. Ohtani, A. Chen, Synthesis and characterization of Carbon-doped TiO_2 nanostructures with enhanced visible light response, Chem. Mater. 19 (2007) 4530–4537, https://doi.org/10.1021/cm071244m.

[24] X. Tang, D. Li, Sulfur-doped highly ordered TiO_2 nanotubular arrays with visible light response, J. Phys. Chem. C 112 (2008) 5405–5409, https://doi.org/10.1021/jp710468a.

[25] T.N.Q. Trang, L.T.N. Tu, C.L.T. Tuyen, T.V. Man, V.T.H. Thu, Surface modification of titanium dioxide nanotubes with sulfur for highly efficient photocatalytic performance under visible light irradiation, Sci. Technol. Dev. J. 21 (2018) 98–105, https://doi.org/10.32508/stdj.v21i3.694.

[26] A. Ghicov, H. Tsuchiya, R. Hahn, J.M. Macak, A.G. Muñoz, P.k Schmuki, TiO_2 nanotubes: H^+ insertion and strong electrochromic effects, Electrochem. Commun. 8 (2006) 528–532, https://doi.org/10.1016/j.elecom.2006.01.015.

[27] X. Chen, L. Liu, P.Y. Yu, S.S. Mao, Increasing solar absorption for photocatalysis with black hydrogenated Titanium dioxide nanocrystals, Science 331 (2011) 746–750, https://doi.org/10.1126/science.1200448.

[28] M. Krbal, H. Sopha, D. Pohl, L. Benes, Ch. Damm, B. Rellinghaus, J. Kupčík, P. Bezdička, J. Šubrt, J.M. Macak, Self-organized TiO_2 nanotubes grown on Ti substrates with different crystallographic preferential orientations: local structure of TiO_2 nanotubes vs. photo-electrochemical response, Electrochim. Acta 264 (2018) 393–399, https://doi.org/10.1016/j.electacta.2018.01.113.

[29] F. Dvorak, R. Zazpe, M. Krbal, H. Sopha, J. Prikryl, S. Ng, L. Hromadko, F. Bures, J.M. Macak, One-dimensional anodic TiO_2 nanotubes coated by atomic layer deposition: towards advanced applications, Appl. Mater. Today 14 (2019) 1–20, https://doi.org/10.1016/j.apmt.2018.11.005.

[30] V. Galstyan, E. Comini, G. Faglia, G. Sberveglieri, TiO_2 nanotubes: recent advances in synthesis and gas sensing properties, Sensors 13 (2013) 14813–14838, https://doi.org/10.3390/s131114813.

[31] Y. LiXia, L. ShengLian, C. QingYun, Y. ShouZhuo, A review on TiO_2 nanotube arrays: fabrication, properties, and sensing applications, Chin. Sci. Bull. 55 (2010) 331–338, https://doi.org/10.1007/s11434-009-0712-3.

[32] C.A. Grimes, K.G. Ong, O.K. Varghese, X.P. Yang, G. Mor, M. Paulose, E.C. Dickey, C.M. Ruan, M.V. Pishko, J.W. Kendig, A.J. Mason, A sentinel sensor network for hydrogen sensing, Sensors 3 (2003) 69–82, https://doi.org/10.3390/s30300069.

[33] N. Kilinc, E. Sennik, Z.Z. Ozturk, Fabrication of TiO_2 nanotubes by anodization of Ti thin films for VOC sensing, Thin Solid Films 520 (2011) 953–958.

[34] W.-T. Kim, I.-H. Kim, W.-Y. Choi, Fabrication of TiO_2 nanotube arrays and their application to a gas sensor, J. Nanosci. Nanotechnol. 15 (2015) 8161–8165, https://doi.org/10.1166/jnn.2015.11278.

[35] I. Kim, W.-Y. Choi, Hybrid gas sensor having TiO_2 nanotube arrays and SnO_2 nanoparticles, Int. J. Nanotechnol. 14 (2017) 155–165, https://doi.org/10.1504/IJNT.2017.082459.

[36] D. Ahuja, D. Parande, Optical sensors and their applications, J. Sci. Res. Rev. 1 (2012) 60–68. ISSN 2277 0690, http://www.wudpeckerresearchjournals.org.

[37] K.-Sh. Mun, S.D. Alvarez, W.-Y. Choi, M.J. Sailor, A stable, label-free optical interferometric biosensor based on TiO_2 nanotube arrays, ACS Nano 4 (2010) 2070–2076, https://doi.org/10.1021/nn901312f.

[38] Y.-Y. Song, P. Schmuki, Modulated TiO_2 nanotube stacks and their use in interference sensors, Electrochem. Commun. 12 (2010) 579–582, https://doi.org/10.1016/j.elecom.2010.02.004.

[39] T. Kumeria, D. Losic, Controlling interferometric properties of nanoporous anodic aluminium oxide, Nanoscale Res. Lett. 7 (2012), https://doi.org/10.1186/1556-276X-7-88, 88-10.

[40] W.T. Kim, W.Y. Choi, Interferometric biosensor using TiO_2 nanotube arrays, Appl. Mech. Mater. 864 (2017) 212–217, https://doi.org/10.4028/www.scientific.net/AMM.864.212.

[41] W.-T. Kim, W.-Y. Choi, Optical interference of TiO_2 nanotube arrays for drug elution sensing, Sci. Adv. Mater. 10 (2018) 283–287. https://doi.org/10.1166/sam.2018.2971.

[42] J.-W. Cheng, Ch. K. Tsang, H. Cheng, F. Liang, Y.Y. Li, Anodic TiO_2-based porous photonic films, Phys. Status Solidi (a) 208 (2011) 1389–1393.

[43] W.-T. Kim, W.-Y. Choi, Fabrication of TiO_2 photonic crystal by anodic oxidation and their optical sensing properties, Sensor. Actuators A 260 (2017) 178–184, https://doi.org/10.1016/j.sna.2017.04.039.

[44] C. Yao, E.B. Slamovich, T.J. Webster, Enhanced osteoblast functions on anodized titanium with nanotube-like structures, J. Biomed. Mater. Res. A 85

(2008) 157–166, https://doi.org/10.1002/jbm.a.31551.
[45] K. Lazarova, H. Awala, S. Thomas, M. Vasileva, S. Mintova, T. Babeva, Sensors 14 (2014) 12207–12218, https://doi.org/10.3390/s140712207.
[46] S.L.R. da Silva, L.O. Kerber, L. Amaral, C.A. dos Santos, X-ray diffraction measurements of plasma-nitrided Ti–6Al–4V, Surf. Coating. Technol. 116–119 (1999) 342–346.
[47] M. Bouroushian, T. Kosanovic, Characterization of thin films by low incidence X-Ray diffraction, Cryst. Struct. Theor. Appl. 1 (2012) 35–39.
[48] G.K. Mor, O.K. Varghese, M. Paulose, C.A. Grimes, Transparent highly ordered TiO_2 nanotube arrays via anodization of titanium thin films, Adv. Funct. Mater. 15 (2005) 1291–1296.
[49] D.Y. Lee, M.H. Lee, B.Y. Kim, N.I. Cho, Crystal structure and photocatalytic activity of Al-doped TiO_2 nanofibers for methylene blue dye degradation, J. Nanosci. Nanotechnol. 16 (2016) 5341–5344.
[50] Ch.W. Lai, S. Sreekantan, Photoelectrochemical performance of smooth TiO_2 nanotube arrays: effect of anodization temperature and cleaning methods, Int. J. Photoenergy 2012 (2012) 356943–357011.
[51] Q. Zhang, L. Ma, M. Shao, J. Huang, M. Ding, X. Deng, X. Wei, X. Xu, Anodic oxidation synthesis of one-dimensional TiO_2 nanostructures for photocatalytic and field emission properties, J. Nanomater. (2014) (2014) 831752–831814.
[52] K.A. Smith, A.I. Savva, Ch. Deng, J.P. Wharry, S. Hwang, D. Su, Y. Wang, J. Gong, T. Xu, D.P. Butt, H. Xiong, Effects of proton irradiation on structural and electrochemical charge storage properties of TiO_2 nanotube electrode for lithium-ion batteries, J. Mater. Chem. 5 (2017) 11815–11824.
[53] H.-Y. Liu, Y.-L. Hsu, H.-Y. Su, R.-Ch. Huang, F.-Y. Hou, G.-Ch. Tu, W.-H. Liu, A comparative study of amorphous, anatase, rutile, and mixed phase TiO_2 films by mist chemical vapor deposition an ultraviolet photodetectors applications, IEEE Sens. J. 18 (2018) 4022–4029.
[54] S. Bauer, A. Pittrof, H. Tsuchiya, P. Schmuki, Size-effects in TiO_2 nanotubes: diameter dependent anatase/rutile stabilization, Electrochem. Commun. 13 (2011) 538–541.
[55] M. Krbal, H. Sopha, V. Podzemna, S. Das, J. Prikryl, J.M. Macak, TiO_2 nanotube/chalcogenide - based photoelectrochemical cell: nanotube diameter dependence study, J. Phys. Chem. C 121 (2017) 6065–6071, https://doi.org/10.1021/acs.jpcc.6b11283.
[56] B. Ercan, E. Taylor, E. Alpasl an, T.J. Webster, Diameter of titanium nanotubes influences anti-bacterial efficacy, Nanotechnology 22 (11pp) (2011) 295102, https://doi.org/10.1088/0957-4484/22/29/295102.
[57] R. Kuzel, L. Nichtova, Z. Matej, T. Brunatova, Temperature evolution of microstructure of TiO_2 thin films and powders studied by X-ray diffraction. http://nanocon2014.tanger.cz/files/proceedings/nanocon_10/lists/papers/598.pdf.
[58] D. Nesheva, Nanoparticle layers in multilayers, in: H.S. Nalwa (Ed.), Encyclopedia of Nanoscience and Nanotechnology vol. 7, American Scientific Publishers, Stevenson Ranch, California, USA, 2004, pp. 105–123.
[59] A. Asana, T. Ichimura, M. Ohsawa, H. Sakai, Y. Uchida, Characterization of a-Si1-xCx:H/a-Si:H and a-SiNX:H/a-Si:H heterojunctions by photothermal deflection spectroscopy, J. Non-Cryst. Solids 97–98 (1987) 971–974. https://doi.org/10.1016/0022-3093(87)90234-1.
[60] Z.H. Lu, D.J. Lockwood, J.-M. Baribeau, Quantum confinement and light emission in SiO_2/Si superlattices, Nature 378 (1995) 258, https://doi.org/10.1038/378258a0.
[61] G.V.M. Willams, A. Bittar, H.J. Trodahl, Crystallization and diffusion in progressively annealed a-Ge/SiO_x superlattices, J. Appl. Phys. 67 (1990) 1874–1878, https://doi.org/10.1063/1.345616.
[62] M. Grujic-Brojcin, M.J. Scepanovic, Z.D. Dohcevic-Mitrovic, Z.V. Popovic, Use of phonon confinement model in simulation of Raman spectra of nanostructured materials, Acta Phys. Pol., A 116 (2009) 51–54, https://doi.org/10.12693/APhysPolA.116.51.
[63] M.J. Šćepanović, M. Grujić-Brojčin, Z.D. Dohčevic-Mitrović, Z.V. Popović, Temperature dependence of the lowest frequency E_g Raman mode in laser-synthesized anatase TiO_2 nanopowder, Appl. Phys. A 86 (2007) 365–371, https://doi.org/10.1007/s00339-006-3775-x.
[64] M.U. Grujić-Brojčin, M.J. Šćepanović, D. Nesheva, V. Dzhurkov, B. Valdes-Salas, O. Perez, N. Nedev, M. Curiel, Z.V. Popović, Raman spectroscopy studies of annealed TiO2 nanotubes anodically grown on Ti6Al4V alloy substrates, in: 19th International Workshop on Nanoscience and Nanotechnology NANO 2017, November 24-25, 2017, https://doi.org/10.13140/RG.2.2.25485.03045. Sofia Bulgaria.
[65] J.C. Parker, R.W. Siegel, Calibration of the Raman spectrum to the oxygen stoichiometry of nanophase TiO_2, Appl. Phys. Lett. 57 (1990) 943–945, https://doi.org/10.1063/1.104274.
[66] Y.-R. Luo, Bond Dissociation Energies, http://staff.ustc.edu.cn/~luo971/2010-91-CRC-BDEs-Tables.pdf.

Computational Materials Science 162 (2019) 82–87

Contents lists available at ScienceDirect

Computational Materials Science

journal homepage: www.elsevier.com/locate/commatsci

Data mining to predict the average outer diameter of vertically aligned TiO_2 nanotubes

Jesús Caro-Gutiérrez, Oscar M. Peréz-Landeros, Félix F. González-Navarro*, Mario A. Curiel-Álvarez, Benjamín Valdez-Salas, Nicola Radnev-Nedev

Engineering Institute, Autonomous University of Baja California, Mexicali, Mexico

ARTICLE INFO

Keywords:
Data mining
Outer diameter measurement
Vertically aligned nanotubes
Ellipsometry

ABSTRACT

Nowadays, the development of new technology is strongly based on nanomaterials studies, such as vertically aligned TiO_2 nanotubes (TONTs), which are widely used in different fields of industry. Physical properties of these materials depend on their size (inner and outer diameters) and shape, for this reason they must be measured accurately. Inner and outer diameter measurement is performed manually on images obtained by means of scanning electron microscopy. Time-consuming image analysis, subjective and low-representative readings are some disadvantages found in this process. This paper proposes a model to predict the average outer diameter of TONTs using Data Mining and Ellipsometry, because they have the potential to overcome disadvantages mentioned above. The diameter with measurements of light reflection intensity and ellipsometric parameters is modelled using different techniques. A model that shows a very low prediction error using linear support vector machines for regression is reported.

1. Introduction

In 1999, the feasibility of growing vertically aligned TiO_2 nanotubes (TONTs) was probed, since then these nanostructures have been widely studied in materials science. Due to their properties they are used in biomedical, photochemical, electrical, and environmental applications [1]. The properties of TONTs depend strongly on their size (diameters and length) and shape, for example the diameters (inner and outer) have a huge effect on the physical properties. For this reason, they must be measured accurately [2].

Inner and outer diameter measurement of each nanotube and their averages in a sample is generally performed through semiautomatic routines on images obtained by scanning electron microscope (SEM), which brings certain disadvantages. This measurement is manual and can be a very time-consuming activity. Also, it may be not representative because only a fraction of nanotubes is considered for calculation (see Fig. 1). Moreover, since it is carried out by human observers, it is exposed to subjectivity. And in addition to this, the prolonged use of the SEM can damage the sample and incur in higher costs.

To face these disadvantages new methods are being developed. In this paper, it is proposed to predict the average outer diameter of TONTs using ellipsometry. This technique measures changes in light polarization to determine primarily film thickness and optical constants. However, it is also applied to other material characteristics because it is non-destructive, highly accurate and very sensitive [3]. Ellipsometry provides a large amount of measurements which could be analyzed with data mining to build and adjust models that predict nanotubes properties.

Data mining in conjunction with ellipsometry have the potential to overcome the disadvantages mentioned above. First, the average outer diameter measurement would be automatic which reduces the time required for this activity. Second, it would be representative because data from the entire sample of nanotubes can be analyzed. Thirdly, it does not require the observer's intervention, and therefore the subjectivity problem is overcome because the same parameters and algorithms are used in each sample. Finally, ellipsometry does not damage the sample and it is a more economical technique.

The objectives of this paper are: 1) to propose a model for predicting the average outer diameter of TONTs using data mining in conjunction with ellipsometry; 2) to assess the correlation between real measurements and those estimated by the model; 3) and to present the proportions that have different variables in the model. The rest of this paper is organized as follows: Section 2 describes the materials and methods used in the experiments, Section 3 shows the results and their discussion, and some conclusions are given in Section 4.

* Corresponding author.
E-mail address: fernando.gonzalez@uabc.edu.mx (F.F. González-Navarro).

https://doi.org/10.1016/j.commatsci.2019.02.041
Received 4 January 2019; Received in revised form 22 February 2019; Accepted 26 February 2019

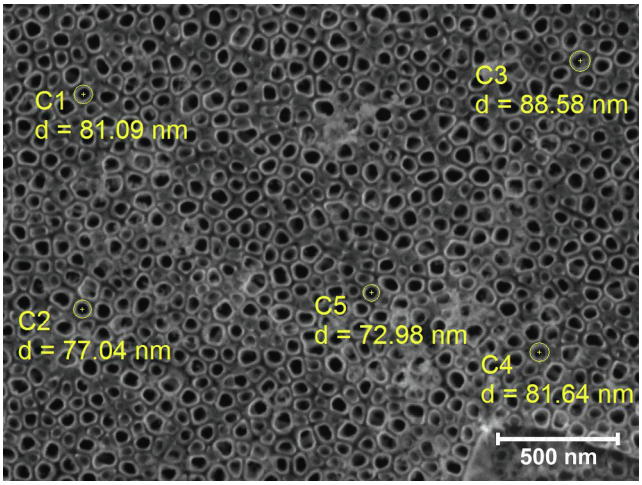

Fig. 1. Outer diameters measurement of vertically aligned TiO_2 nanotubes through semiautomatic routines.

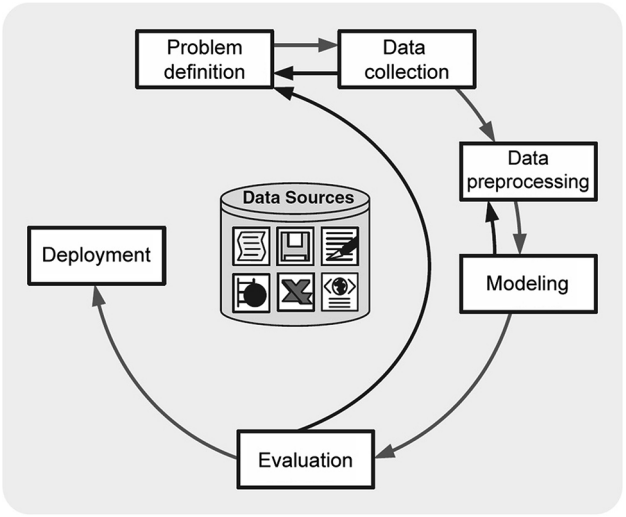

Fig. 2. Stages of the data mining process.

2. Materials and methods

Materials (software and hardware) used in experimental stage are described, as well as the methodology followed in this research.

2.1. Software and hardware

Software programming was carried out by using the MATLAB R2017b with Windows 7 (64 bit) operating system. A personal computer with an Intel Core i7-3770 CPU @ 3.4 GHz processor and 8 GB RAM memory was used to run the experiments.

2.2. Methodology

The methodology proposed in Fig. 2 was applied, which corresponds to a data mining process. The activities carried out in some stages are detailed in the next subsections.

2.2.1. Data collection

18 vertically aligned TiO_2 nanotubes samples were used. Their average outer diameters varied between 20 and 100 nm. Data were acquired by means of a Woollam Vase ellipsometer with rotating analyzer (model M-2000U). Measurements were the light reflection intensity (I) and the ellipsometric parameters Ψ and Δ taken at five different angles of incidence (θ = 45, 55, 65, 75 and 85°) over the spectral range from 245 to 1000 nm in steps of 1.58 nm, altogether 478 wavelengths (λ). From these measurements a 478 × 15 matrix was obtained per sample. To create the data set for mining, it was necessary to reshape these matrices into row vectors, concatenate them vertically and add the corresponding diameters, resulting in an 18 × 7171 data matrix, as can be seen in Fig. 3.

$$\begin{array}{c} \\ sample_1 \\ sample_2 \\ \vdots \\ sample_{18} \end{array} \begin{array}{c} \begin{array}{cccc} \multicolumn{3}{c}{measurements} & & diameter \end{array} \\ \begin{pmatrix} x_{1,1} & x_{1,2} & \cdots & x_{1,7170} & y_{1,7171} \\ x_{2,1} & x_{2,2} & \cdots & x_{2,7170} & y_{2,7171} \\ \vdots & \vdots & & \vdots & \vdots \\ x_{18,1} & x_{18,2} & \cdots & x_{18,7170} & y_{18,7171} \end{pmatrix} \end{array}$$

Fig. 3. Data matrix (18 × 7171) for mining created from measurements.

2.2.2. Data preprocessing

This is an important stage in the data mining process, which tries to solve issues such as missing values, noisy, irrelevance and redundancy [4]. In our case, a first inspection of the data showed that it was complete, therefore it was not necessary to apply methods for handling missing measurements. Also, as already mentioned, the ellipsometry is highly accurate, so neither noise reduction techniques were considered. Ultimately, the preprocessing consisted of a data transformation and a feature selection to eliminate irrelevance.

Data transformation. It was made by means of a z-score normalization that converts all measurements (features) to a common scale with an average of zero and standard deviation of one. This transformation can be represented with the equation:

$$Z_x = \frac{X_i - \overline{X}}{S_x} \tag{1}$$

where X_i is the original feature and Z_x the new one, $\overline{X}$ and S_x are the mean and the standard deviation respectively of original feature. The z-score normalization was chosen because it may improve the accuracy and efficiency of the modeling techniques used in later stages [5].

Feature selection. Feature selection is the process of identifying and eliminating irrelevant and redundant features from the data, which do not contribute to the accuracy of the model. This reduces the complexity of the data and final model, and makes it easier to understand. It also allows modeling techniques to operate faster and more effectively [6].

In this work, the feature selection was performed using Backward Elimination [7], as shown in the Algorithm 1. It starts with all the features and progressively eliminate the least important ones which improves the performance of the models. This is repeated until no improvement is observed on removal of features [8]. Finally, the set of features of the model with the best performance is selected. Model was constructed using a support vector machine because it has revealed a great ability in the process of feature selection, especially in the context of multidimensional data [9]. Performance of the models was determined by estimating their mean square error (MSE) in a cross-validation.

Algorithm 1 Backward elimination for feature selection

Input: $P^0 = \phi$, $P^1 = \{allfeatures\}$, $R = \phi$, $i = 1$
Output: Best subset P^i
1: **procedure** BACKWARDELIMINATION()
2: **while** $P^i \neg = P^{i-1}$ **do**
3: **for** each $v \in P^i$ **do**
4: set $P' \leftarrow P^i \setminus v$;
5: train the SVM with P' and get the
6: validation performance $F(P')$;
7: **if** $F(P') \geqslant F(P^i)$ **then**
8: $R \leftarrow R \cup \{v\}$;
9: **end if**
10: **end for**
11: $P^{i+1} \leftarrow P^i \setminus R$;
12: $i++$;
13: $R = \phi$;
14: **end while**
15: return P^i;
16: **end procedure**

2.3. Modeling

Once the relevant features have been selected the next step is to construct a model that performs with the lowest MSE error using these selected features [10]; in the context of this paper to predict the average outer diameter from ellipsometric measurements. At this step, a comparison of different modeling techniques to choose the best one based on their performance was made. The techniques selected were: linear model (LM), k-nearest neighbor (KNN), neural network (NN) and support vector machine (SVM). Some models requires what is called parameter tunning e.g. the number of neighbors in kNN. Hence a grid search [11] was used to this purpose – see Table 1. In the next subsections a short description of each techniques is given.

2.3.1. Linear model

Linear regression is used to predict the value of a response variable Y based on one or more predictor variables $X_1, X_2, ...,X_n$. The aim is to establish a linear relationship (a mathematical model) between the predictor variables and the response variable, so that, this formula can be used to estimate the value of the response Y, when only the predictors values are known. This mathematical model can be generalized as follows:

$$Y = \beta_0 + \sum_{i=1}^{n} \beta_i X_i \tag{2}$$

where β are the coefficients that indicate the contribution of the predictor variables. The objective is to find these coefficients by means of some fit criterion. The most common method for fitting a linear regression model is the Least Squares method [12].

Table 1
Optimal parameters of modeling techniques.

Technique	Parameter	Value
LM	Model type	PLS
KNN	K	5
	Distance	Euclidean
NN	Hidden	10
	Training	Levenberg-Marquardt
	Performance	MSE
SVM	SVM type	Nu-SVR
	Kernel type	Linear
	Epsilon	0.001
	Cost	1
	Nu	0.5

2.3.2. K-nearest neighbor

K-nearest Neighbor is a simple technique to predict the value of an response variable based on a similarity measure (distance function). An implementation of KNN regression is to calculate the average value of the response variable of the k-nearest neighbors [13]. Another approach uses an inverse distance weighted average of the k-nearest neighbors. In this work, the second approach with an euclidean distance function was used as follows:

$$D = \sqrt{\sum_{i=1}^{n} (X_i - Y_i)^2} \tag{3}$$

where D is the distance between two samples (observations), X_i and Y_i the values of their predictor variables. In general, a large k value is more precise as it reduces the noise.

2.3.3. Neural network

Artificial Neural Networks are inspired by the biological process of brain and are used to create mathematical models of the data processed by neurons. They consist of units (artificial neurons) connected with each other in a certain architecture. A well-known architecture is the feed-forward configuration, which builds a model of the form:

$$Y = g\left(\sum_{j=1}^{m} w_j \phi\left(x; v_j\right) + b\right) \tag{4}$$

where g is a non-linear activation function (or the identity in regression), w_j the vector of linear weights, x the vector of predictor variables, v_j the vector of non-linear weights and b the bias. Neural networks use optimization strategies to fit the weights and improve the prediction of

Table 2
Selected features using backward elimination.

#	Feature		
	Measurement	Angle of incidence (θ)	Wavelength (λ)
1	I	45°	304
2			305
3			307
4			369
5			370
6		55°	361
7		65°	305
8			351
9			353
10		75°	444
11			445
12			447
13			456
14			459
15			461
16	Ψ	45°	350
17		75°	261
18			266
19	Δ	45°	332
20			436
21			784
22		65°	405
23			409
24			410
25			938
26		75°	474
27			477
28			478
29			480
30			507
31			515
32			520
33			585
34			586
35		85°	766

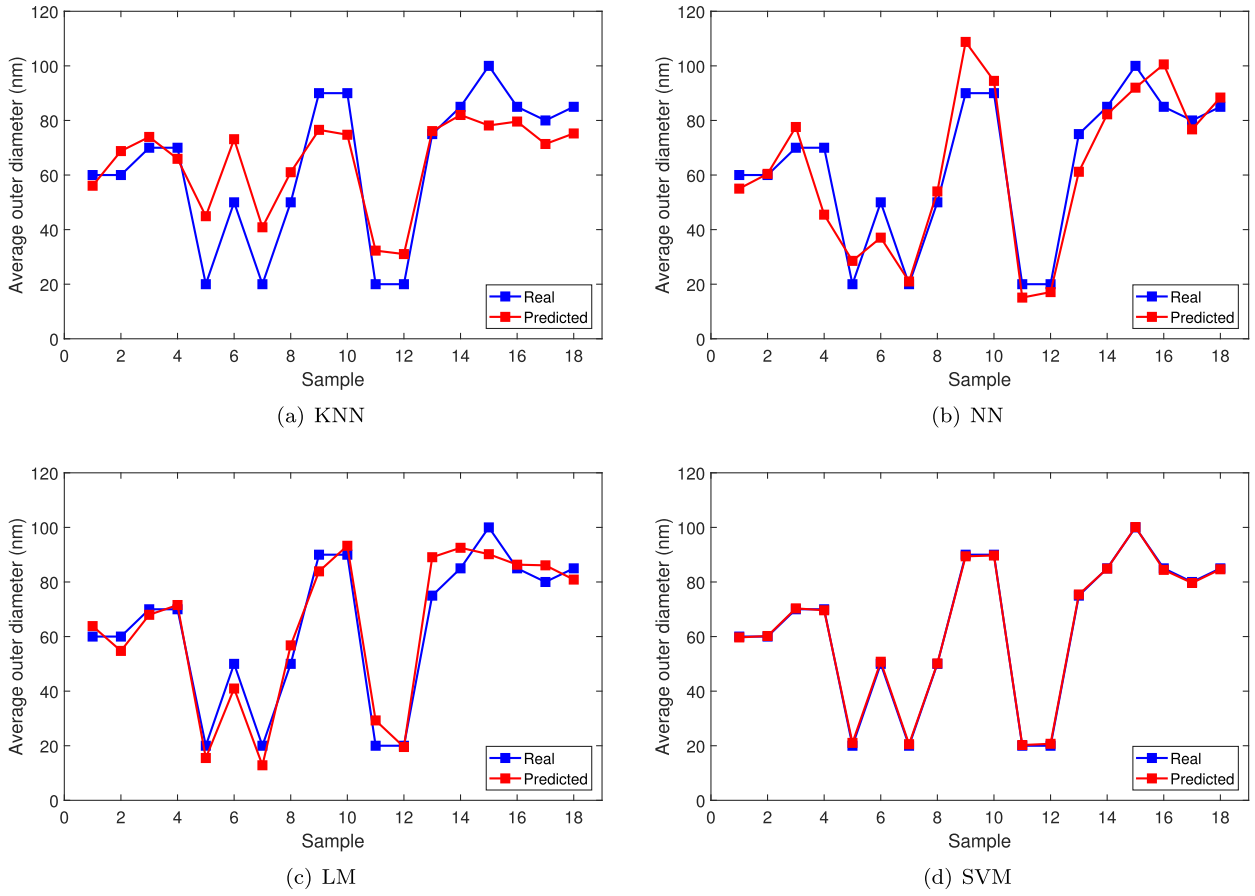

Fig. 4. Prediction of average outer diameter by modeling techniques.

the response variable [14]. In our case, we use a Levenberg–Marquardt method.

2.3.4. Support vector machine

Support Vector Machines model was developed to solve classification and regression problems in machine learning. In the second case, the goal is to find a model from the input feature space, which predicts a target variable. SVM can be used for linear regression by the introduction of a loss function, and for non-linear regression by a mapping of the original data into a high dimensional feature space through a kernel function [15]. In the experiments, a linear kernel function was selected as follows:

$$K(x_i, x_j) = x_i^T x_j \tag{5}$$

where x_i and x_j are input vectors. There are several kernel functions but the most used are: linear, polynomial, radial basis and sigmoidal.

2.4. Evaluation

Evaluation is a necessary part of Model Development because it helps to find the best model that represents the data and how well this will work with new samples. Evaluation of model's performance with data used for its creation (training) is not acceptable in data mining because it generates overfitted models [16]. There are two methods to assess performance and avoid overfitting, both use a test set not seen by the model, hold-out and cross-validation.

We use the second in the experiments, specifically leave-one-out (LOOCV) since it has proved to be superior when a limited amount of data is available [17]. In this method, all of the data except one sample is used for training and one sample is used for testing. This process is repeated for N times if there are N samples. The advantage is that entire data is used for training and testing. The model error is average of the error in all experiments.

3. Results and discussion

This section presents the experimental results obtained in some stages of the data mining process, as well as their discussion.

Table 2 shows the selected features subset by means of the backward elimination algorithm, which consists of only 35 features out of 7170 in the data matrix. In other words, 99.51% of irrelevant features were eliminated from the data, thus achieving a drastic reduction of dimensionality that made the problem more tractable.

If the selected features are reviewed in more detail, certain proportions of interest can be obtained. For example, the percentage of features belongs to measurement or angle of incidence. According to this, the following observations are done from Table 2. In the case of measurements, most of the selected features belong to Δ and I with 48.57% and 42.85%, respectively. For the situation of the incidence angles, majority of the selected features were taken at $\theta = 75°$ with 48.57%, followed by 45° and 65° with 25.71% and 20%, respectively. Finally, the measurement Ψ and the incidence angles $\theta = 55°$ and 85° were less representative than the previous ones. In the context of

Table 3
MSE of the modeling techniques in a LOOCV.

Modeling technique	MSE
KNN	178.2803
NN	103.996
LM	43.8536
SVM	0.2343

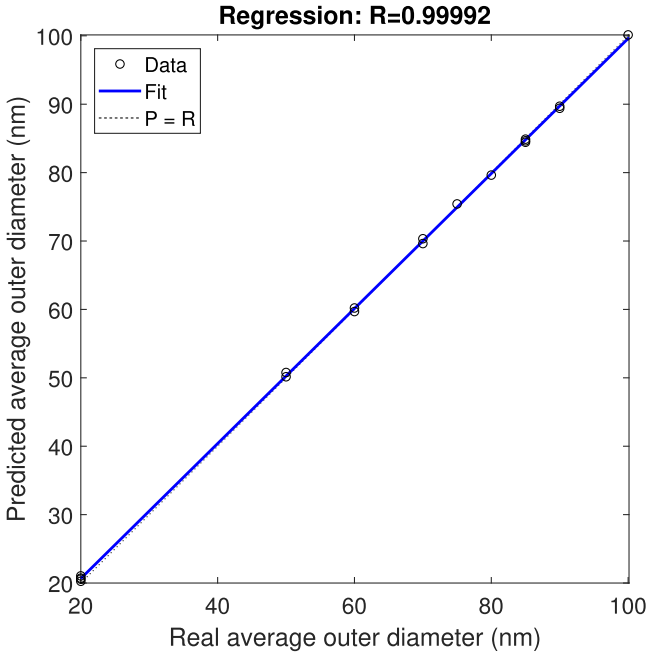

Fig. 5. Linear regression between real and predicted average outer diameters.

measuring the average outer diameter of TONTs using ellipsometry, data representation in a low dimension may be important, helping researchers to get a better understanding of this area.

Fig. 4 presents the prediction of average outer diameter by the different modeling techniques. When making a comparison of these, it is clearly seen that the SVM model outperformed the rest of the models (KNN, NN and LM) because it achieved an almost identical regression plot to the one formed by the real diameters. To further support this result, Table 3 shows the performances of the models determined by their MSE in a LOOCV. As can be observed, the MSE of the SVM model was 0.2343, which is by far the smallest value. Getting a good MSE is important when measuring material characteristics through ellipsometry. In the literature a MSE in the range of 1–20 is usually aceptable [18], it depends on the complexity of the sample. It should be noted that the MSE obtained by the SVM model was even less than 1, for this reason it is chosen as the best.

Eq. (6) represents the mathematical model found by the SVM technique; where *AOD* is the average outer diameter, I_θ^λ the light reflection intensity, Ψ_θ^λ and Δ_θ^λ the ellipsometric parameters taken at a certain angle of incidence θ and wavelength λ. As it can be seen, the relationship between the variables of interest was determined by fitting a linear equation. Fig. 5 plots the regression between real AODs and those predicted by the equation. Also shows its correlation coefficient *R* which measures how well the model can predict the data (falls between 0 and 1). The higher the value of R, the better the model is at predicting the data. R-value obtained was 0.99992, which means that the model obtained predicts the average outer diameter of TONTs with very low error.

$$\begin{aligned} AOD = &- 1.25I_{\theta=45^\circ}^{\lambda=304} - 1.23I_{\theta=45^\circ}^{\lambda=305} - 1.22I_{\theta=45^\circ}^{\lambda=307} - 1.25I_{\theta=45^\circ}^{\lambda=369} \\ &- 1.32I_{\theta=45^\circ}^{\lambda=370} - 1.34I_{\theta=55^\circ}^{\lambda=361} - 1.63I_{\theta=65^\circ}^{\lambda=305} - 1.47I_{\theta=65^\circ}^{\lambda=351} \\ &- 1.55I_{\theta=65^\circ}^{\lambda=353} - 1.86I_{\theta=75^\circ}^{\lambda=444} - 1.93I_{\theta=75^\circ}^{\lambda=445} - 1.99I_{\theta=75^\circ}^{\lambda=447} \\ &- 2.18I_{\theta=75^\circ}^{\lambda=456} - 2.17I_{\theta=75^\circ}^{\lambda=459} - 2.16I_{\theta=75^\circ}^{\lambda=461} - 1.60\Psi_{\theta=45^\circ}^{\lambda=350} \\ &+ 0.95\Psi_{\theta=75^\circ}^{\lambda=261} + 0.91\Psi_{\theta=75^\circ}^{\lambda=266} - 2.50\Delta_{\theta=45^\circ}^{\lambda=332} + 0.84\Delta_{\theta=45^\circ}^{\lambda=436} \\ &+ 1.46\Delta_{\theta=45^\circ}^{\lambda=784} + 1.10\Delta_{\theta=65^\circ}^{\lambda=405} + 1.12\Delta_{\theta=65^\circ}^{\lambda=409} + 0.84\Delta_{\theta=65^\circ}^{\lambda=410} \\ &- 2.16\Delta_{\theta=65^\circ}^{\lambda=938} - 2.64\Delta_{\theta=75^\circ}^{\lambda=474} - 2.44\Delta_{\theta=75^\circ}^{\lambda=477} - 2.22\Delta_{\theta=75^\circ}^{\lambda=478} \\ &- 1.84\Delta_{\theta=75^\circ}^{\lambda=480} + 2.28\Delta_{\theta=75^\circ}^{\lambda=507} + 2.60\Delta_{\theta=75^\circ}^{\lambda=515} + 1.79\Delta_{\theta=75^\circ}^{\lambda=520} \\ &- 1.09\Delta_{\theta=75^\circ}^{\lambda=585} - 1.13\Delta_{\theta=75^\circ}^{\lambda=586} - 1.47\Delta_{\theta=85^\circ}^{\lambda=766} - 62.80 \end{aligned} \quad (6)$$

4. Conclusions

This paper presented a proposal to measure the average outer diameter of vertically aligned TiO_2 nanotubes using data mining in conjunction with ellipsometry. It was established the advantage of this approach over the manual measurement, which is performed through semiautomatic routines on scanning electron microscopy images. Automatic, representative and objective measurements are properties added to this approach; besides being more economical and not damaging the samples. A disadvantage was the limited amount of samples available for experimentation, which affected the generalization of the models.

Different modeling techniques were used to predict the average outer diameter of vertically aligned TiO_2 nanotubes. The experimental results showed that most of the selected features belong to the light reflection intensity *I*, the ellipsometric parameter Δ with the incidence angle $\theta = 75°$. It was also demonstrated a very low prediction error when using support vector machines for regression (even below the range handled in the literature) and that the relationship between the predictor variables and the diameter was linear. Therefore, a linear SVM (Type = Nu-SVR, Epsilon = 0.001, Cost = 1 and Nu = 0.5) is recommended as a good model of the diameter.

Future work will include the creation of a larger samples set to further evaluate the effectiveness of the proposal presented and its application to measure other important properties of TONTs e.g. the length.

CRediT authorship contribution statement

Jesús Caro-Gutiérrez: Conceptualization, Methodology, Software, Validation, Formal analysis, Investigation, Writing - original draft, Writing - review & editing, Visualization, Project administration. **Oscar M. Peréz-Landeros:** Conceptualization, Methodology, Validation, Investigation, Resources. **Félix F. González-Navarro:** Conceptualization, Methodology, Validation, Investigation, Writing - original draft, Writing - review & editing, Supervision. **Mario A. Curiel-Álvarez:** Conceptualization, Investigation, Resources. **Benjamín Valdez-Salas:** Conceptualization, Investigation, Resources. **Nicola Radnev-Nedev:** Conceptualization, Investigation, Resources.

Acknowledgments

The authors thank the National Council on Science and Technology of Mexico (CONACYT) and the Engineering Institute of the Autonomous University of Baja California for its support in the development of this work.

Competing interests

The authors declare no potential competing interests.

Funding source declaration

This research is partially funded by the National Council on Science and Technology of Mexico (CONACYT). This research is also partially funded by the Engineering Institute of the Autonomous University of Baja California.

Data availability

The raw data required to reproduce these findings cannot be shared at this time due to legal or ethical reasons.

Appendix A. Supplementary data

Supplementary data associated with this article can be found, in the online version, athttps://doi.org/10.1016/j.commatsci.2019.02.041.

References

[1] P. Roy, S. Berger, P. Schmuki, Tio_2 nanotubes: synthesis and applications, Nanoscience 50 (2011) 2904–2939.
[2] Y. Iwasaki, T. Nakamiya, R. Kozai, F. Mitsugi, T. Ikegami, An image analysis algorithm to measure the diameters of carbon nanotubes, Prz. Elektrotechniczny 87 (2011) 25–29.
[3] R. Kohli, Methods for monitoring and measuring cleanliness of surfaces. developments in surface contamination and cleaning: detection, characterization, and analysis of contaminants, Developments in Surface Contamination and Cleaning, 2012, pp. 107–178.
[4] S. Garcia, J. Luengo, F. Herrera, Data Preprocessing in Data Mining, Springer, New York, 2015.
[5] L. Shalabi, Z. Shaaban, Normalization as a preprocessing engine for data mining and the approach of preference matrix, International Conference on Dependability of Computer Systems, 2006, pp. 207–214.
[6] V. Kumar, S. Minz, Feature selection: a literature review, Smart Comput. Rev. 4 (3) (2014) 211–229.
[7] X. Lei, F. Zhong-Hua, F. Wei, Pitch-density-based features and an svm binary tree approach for multi-class audio classification in broadcast news, Multimedia Syst. 17 (2011) 101–112.
[8] T. Guyon, A. Elisseeff, An introduction to feature extraction, in: I. Guyon, M. Nikravesh, S. Gunn, L. Zadeh (Eds.), Studies in Fuzziness and Soft Computing, Springer, Berlin, Heidelberg, 2006.
[9] S. El Ferchichi, K. Laabidi, S. Zidi, S. Maouche, Feature selection using an svm learning machine, Signals, Circuits and Systems (SCS), 2009 3rd International Conference on, 2009, pp. 1–6.
[10] M. Kantardzic, Data Mining: Concepts, Models, Methods, and Algorithms, Wiley, New Jersey, 2011.
[11] H. Chih-Wei, C. Chih-Chung, L. Chih-Jen, A practical guide to support vector classification.
[12] D.C. Montgomery, E.A. Peck, G.G. Vining, Introduction to Linear Regression Analysis, Wiley, New Jersey, 2012.
[13] B. Nguyen, C. Morell, B. De-Baets, Large-scale distance metric learning for k-nearest neighbors regression, Neurocomputing 214 (2016) 805–814.
[14] F. Gonzalez-Navarro, M. Stilianova-Stoytcheva, L.B.-M.L. Renteria-Gutierrez, B. Flores-Rios, J. Ibarra-Esquer, Glucose oxidase biosensor modeling and predictors optimization by machine learning methods, Sensors 16 (1483).
[15] W. Flores-Fuentes, M. Rivas-Lopez, O. Srgiyenko, F. Gonzalez-Navarro, J. Rivera-Castillo, D. Hernandez-Balbuena, Machine vision supported by artificial intelligence applied to rotary mirror scanners, Proceedings of the 2014 IEEE 23th International Symposium on Industrial Electronics, 2014, pp. 1949–1954 Istambul, Turkey.
[16] S. Sayad, Real time data mining, Self-Help (2011).
[17] G. Cawley, N. Talbot, Efficient leave-one-out cross-validation of kernel fisher discriminant classifiers, Pattern Recogn. 36 (11) (2003) 2585–2592.
[18] CompleteEASE Data Analysis Manual, J.A. Woollam Co., Inc, Lincoln, 2011.

Ceramics International 45 (2019) 11403–11407

Contents lists available at ScienceDirect

Ceramics International

journal homepage: www.elsevier.com/locate/ceramint

Synthesis of high purity nickel oxide by a modified sol-gel method

D. Mateos[a,*], B. Valdez[a], J.R. Castillo[a], N. Nedev[a], M. Curiel[a], O. Perez[a], A. Arias[b], H. Tiznado[c]

[a] Instituto de Ingeniería, Universidad Autónoma de Baja California, Blvd. Benito Juárez s/n, C.P. 21280, Mexicali, B.C., Mexico
[b] Facultad de Ingeniería, Universidad Autónoma de Baja California, Blvd. Benito Juárez s/n, C.P. 21280, Mexicali, B.C., Mexico
[c] Centro de Nanociencias y Nanotecnología, Universidad Nacional Autónoma de México, Apdo. Postal 14, C.P. 22800, Ensenada, B.C., Mexico

ARTICLE INFO

Keywords:
Nickel oxide
Sol-gel
Nickel acetate
Citric acid

ABSTRACT

Nickel oxide (NiO) powder was synthesized by a modified sol-gel method using nickel acetate, citric acid and ethylene glycol as precursors. The synthesized material was thermally annealed at 250 °C for 2 h (pre-calcination step) and at 800 °C for 1 h (calcination). Scanning electron microscopy shows formation of particles with sizes of up to 50 μm after pre-calcination and of ≲ 10 μm after calcination. Nickel, oxygen and carbon were detected by energy dispersive X-ray spectroscopy (EDS) in the pre-calcined material, while only Ni and O were found after the calcination process. X-ray photoelectron spectroscopy (XPS) indicates that the composition of the synthesized nickel oxide is close to stoichiometric. Raman and Fourier transform infrared spectra show only characteristic peaks of nickel oxide. The calcined particles have cubic crystalline structure of NiO as proved by X-ray diffraction (XRD). EDS, XPS, XRD, Raman and FTIR confirmed that high purity nickel oxide was obtained by the proposed low-cost and highly effective method.

1. Introduction

Nickel oxide (NiO) is a transparent p-type conductive oxide that has recently attracted much attention because of its electrical and optical properties and excellent chemical stability [1–4]. Its band gap is between 3.4 and 4.3 eV depending on the preparation technique and the p-type conductivity is associated with non-stoichiometric defects such as Ni vacancies and O interstitials [5–7]. Non-stoichiometric nickel oxide (NiO_x) has been used in thin film transistors [8,9], electrochromic devices [10–12], batteries and gas sensors [13–18]. It is also a promising material for UV photodetectors [19] and organic/inorganic solar cells [20].

There are several methods to obtain NiO_x. However, most of them use expensive techniques such as reactive magnetron sputtering [21,22] or metal organic chemical vapor deposition [23]. Another way to obtain NiO_x is by sol-gel method. Thin films can be obtained from sol-gel solutions by various techniques such as spin coating, spraying, electrodeposition, dip coating, etc. Sol-gel spin coating is a low-temperature damage free process, which is simple, safe, cost effective and allows deposition of high purity homogenous films [1,5]. Jiao et al. [11] have synthesized NiO using $NiCl_2 \cdot 6H_2O$ and citric acid as precursors applying thermal treatments in two different steps for a total time of 29 h at 90 °C. In the synthesis route proposed in [12] one of the precursors is hydrochloric acid.

In this work, we present results for synthesis that is green, facile, versatile and low-cost. NiO_x was synthesized using the modified sol-gel method, in which salts are used as precursors of metal ions, citric acid as a chelating agent and polyethylene glycol as a crosslinking agent [24]. It is a sequential process, which is based on the ability of α-hydroxycarboxylic acids, such as citric acid, to chelate metal ions. These chelates are subjected to a polyesterification with polyfunctional alcohols, such as ethylene glycol, resulting in formation of a polymeric resin [25]. The resin is calcined at an appropriate temperature that allows elimination of the organic matrix and impurities and formation of fine particles of the desired oxide.

An important advantage of the modified sol-gel method is the adequate formation of metallic complexes, which are stabilized by chelate agents at appropriate pH, thus allowing synthesis of complex oxides [26]. Other advantages, which are result from using solid state precursors, are high purity and homogeneity of the synthesized oxide, precise control of stoichiometry and the possibility to obtain thin films, fibers and nano-sized powders within a few hours at appropriate temperature [27].

* Corresponding author.
E-mail address: david.mateos@uabc.edu.mx (D. Mateos).

https://doi.org/10.1016/j.ceramint.2019.03.005
Received 17 December 2018; Received in revised form 22 February 2019; Accepted 1 March 2019
Available online 07 March 2019

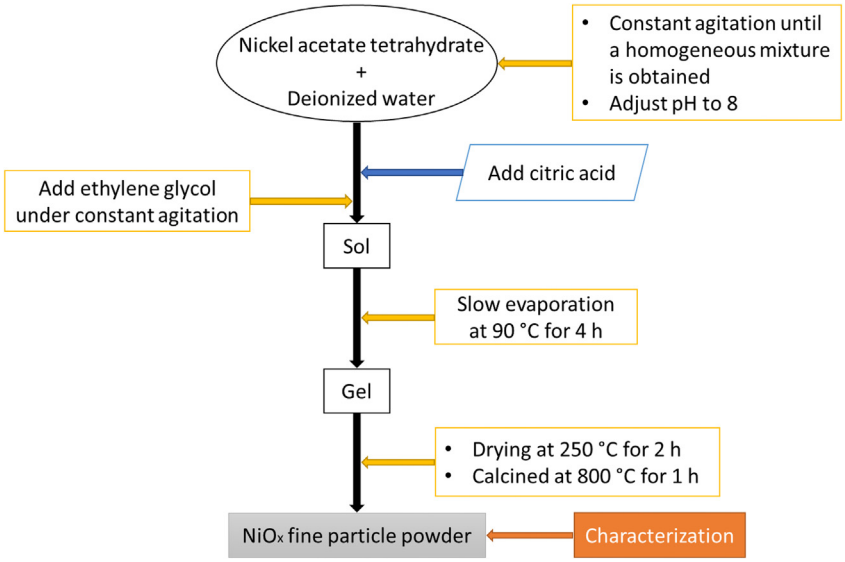

Fig. 1. Flowchart of the NiO_x synthesis method.

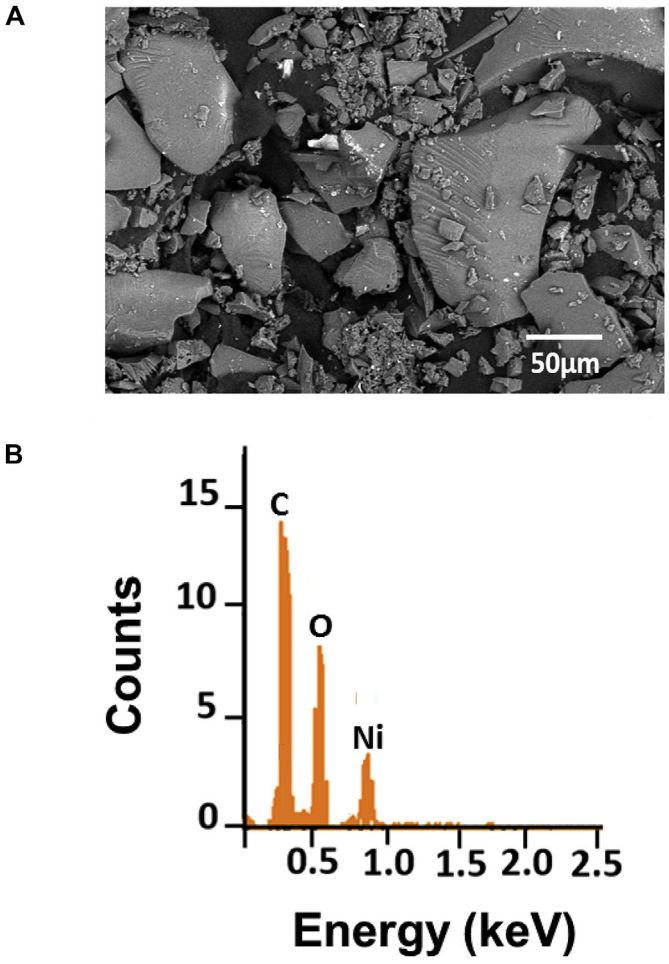

Fig. 2. SEM image (a) and EDS spectrum (b) of NiO_x annealed at 250 °C.

2. Experimental details

2.1. Synthesis

Precursor solution of 0.1 M Ni^{2+} was prepared by dissolving 2.54 g of nickel acetate tetrahydrate [Ni $(CH_3COO)_2 \cdot 4H_2O$] (Sigma Aldrich) of 98% purity in 100 mL of deionized water. Then, 1 mL of 1 M aqueous solution of citric acid and 10 mL of ethylene glycol were added. The pH was adjusted to 8 with 30% ammonium hydroxide (NH_4OH). The solution was evaporated for 4 h at 90 °C with constant agitation, which favors the reactions of hydrolysis, esterification, polyesterification and gel formation. Afterwards, the gel was heated at 250 °C for 2 h at atmospheric pressure (pre-calcined step). As a result, a black carbonaceous resin was obtained. Finally, the resin was calcined at 800 °C for 1 h to obtain NiO_x. Fig. 1 shows the flowchart of the NiO_x synthesis.

2.2. Characterization

The shape, surface morphology and elemental composition of the synthesized material were studied using scanning electron microscope JEOL JSM-6010LA equipped with an energy dispersive X-ray detector. Photoelectron core-level spectra of NiO_x were obtained using an X-ray photoelectron spectroscopy (XPS) system Specs, equipped with a monochromatic Al Kα X-ray source (1487 eV) with a 400 µm spot size. The base pressure of the system was 6×10^{-10} Torr. Powder samples were mounted on double-sided carbon tape. Special scans at 10 eV were collected for Ni $2p_{3/2}$. The Ni $2p_{3/2}$ raw data were fitted with parameters determined in [28] where the main Ni^{2+} peak of NiO was composed of 4 satellites with given relative intensities and positions. Since the Ni 2p peaks of nickel hydroxide and other nickel chemical species are broad and close in binding energy, they were grouped in a single peak (and a satellite). The O 1s data were fitted taking into account the results in [29,30] where thorough study for interpretation of the XPS spectrum of different nickel compounds was carried out. The fittings presented in this work combine Gaussian-Lorentzian (70%–30%) curves and Shirley-type background.

Raman scattering spectra were obtained at room temperature using Perkin Elmer Raman Station 400F with a 785 nm laser. Infrared spectra were measured in the 400–4000 cm^{-1} range using Perkin Elmer Frontier FTIR instrument.

X-ray diffraction (XRD) analysis was carried out using a Bruker D8 Advance diffractometer with Cu K_α source operated at 30 kV and 30 mA. In order to obtain information on the crystallographic structure of the synthesized material the samples were scanned from 20° to 90° (2θ).

3. Results and discussions

Fig. 2 shows a scanning electron microscopy (SEM) image and

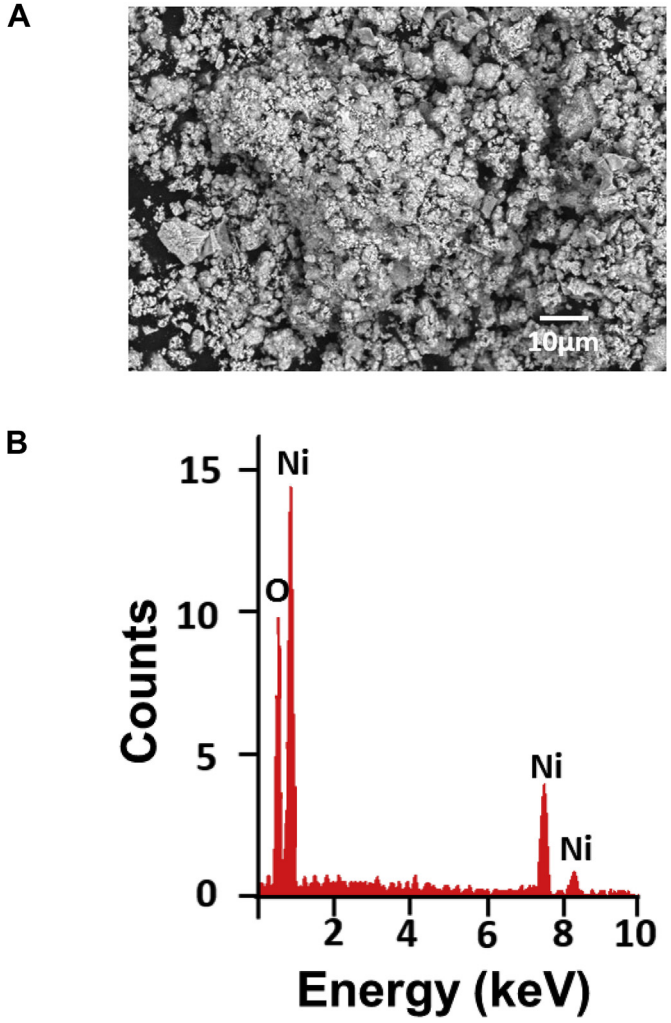

Fig. 3. SEM image (a) and EDS spectrum (b) of NiO_x annealed at 800 °C.

Energy Dispersive X-ray Spectroscopy (EDS) results of a sample annealed at 250 °C. The image exhibits a large number of particles with dimensions $\lesssim$ 10 μm and some particles with sizes of about 50 μm and more. These particles were obtained as a result of the pre-calcination process and are mixture of carbonaceous resin with NiO_x.

The EDS analysis revealed Ni, O and C in the synthesized material. The presence of carbon atoms can be attributed to the formation of polymeric carbonaceous resin. The result indicates that the pre-calcination temperature is not high enough to eliminate the organic matter present in the material.

However, the EDS spectrum of calcined resin shows only Ni and O (Fig. 3(b)) indicating that the thermal process at 800 °C is crucial for the elimination of the carbon impurities. As a result, a material with high degree of purity was obtained. The EDS results for the weight percentages of Ni, O and C in pre-calcined and calcined material are shown in Table 1. The SEM image of calcined sample (Fig. 3(a)) exhibits NiO_x crystals with size of the order of micrometers.

Table 1
Ni, O and C weight percentage in pre-calcined and calcined samples.

Element	Wt %	
	250 °C	800 °C
Ni	18.49	81.14
O	27.49	18.86
C	54.02	–
Total	**100.0**	**100.0**

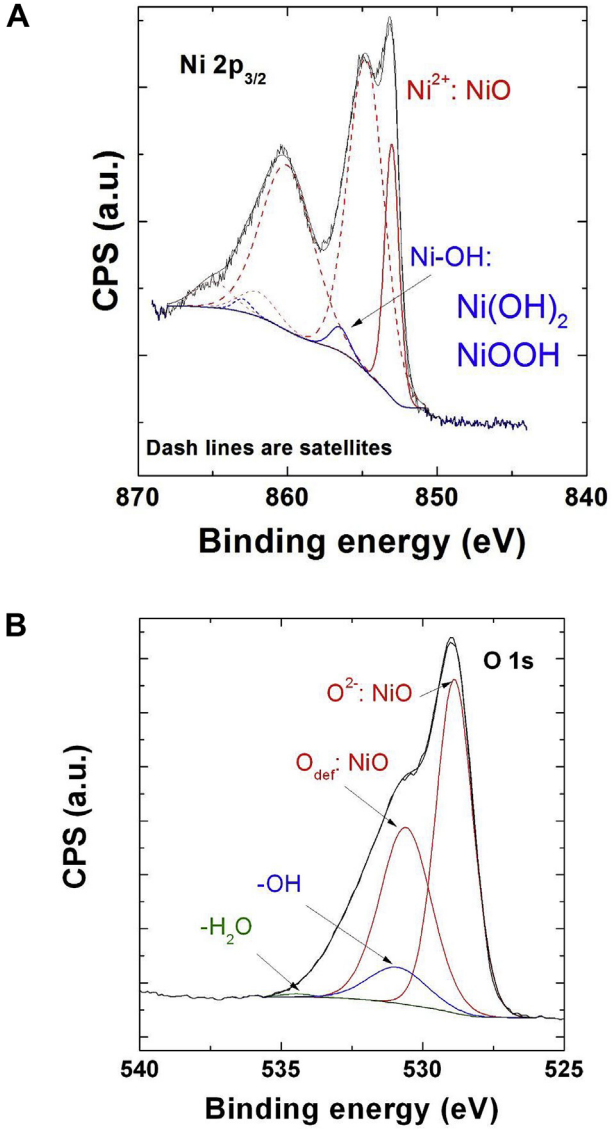

Fig. 4. High resolution XPS spectra of Ni $2p_{3/2}$ (a) and O 1s (b) of a sample annealed at 800 °C.

Fig. 4(a) and (b) show the Ni $2p_{3/2}$ and O 1s spectra, respectively. Ni $2p_{3/2}$ was fitted with a main peak at 853.0 eV for Ni^{2+} in NiO [31]. A small peak of nickel hydroxide compounds, such as $Ni(OH)_2$ and/or NiOOH (labeled as Ni—OH), is also seen at 856.5 eV. The area of the nickel hydroxide peak is much smaller than that of the NiO peak indicating that Ni is mainly bonded to oxygen in NiO. The O 1s region was fitted with two peaks related to NiO, at 528.9 and 530.6 eV [32,33]. The first one was assigned to oxygen within the oxide crystal (O^{2-}) and the second one to oxygen adjacent to Ni vacancies (O_{def}). A relatively small peak at 530.9 eV was assigned to —OH groups, which correlates with the nickel hydroxide peak found at 856.5 eV in Fig. 4(a).

The FTIR and Raman results additionally confirmed the formation of nickel oxide. The FTIR spectrum (Fig. 5(a)) displays two characteristic peaks at ~ 405 cm^{-1} and ~1041 cm^{-1}, which correspond to Ni—O stretching vibrational modes [34]. The Raman spectrum in Fig. 5(b) exhibits a non-symmetric peak at ~ 510 cm^{-1} characteristic for Ni—O stretching mode, a result in agreement with previously published data [34–36].

Fig. 6(a) and (b) show diffractograms of samples annealed at 250

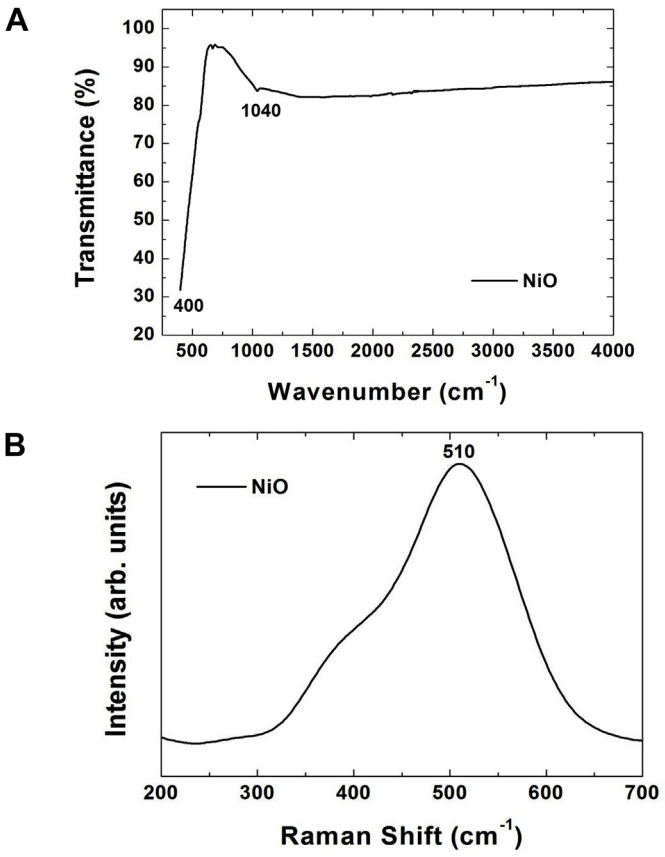

Fig. 5. FTIR (a) and Raman (b) spectra of NiO annealed at 800 °C.

and 800 °C, respectively. The diffractogram of the pre-calcined sample (Fig. 6(a)), which contains carbonaceous resin and NiO particles, exhibits wide and relatively low intensity peaks at 37.2°, 43.1°, 62.8°, 75.41° and 79.4° corresponding to (1 1 1), (2 0 0), (2 2 0), (3 1 1) and (2 2 2) lattice planes of crystalline NiO. The peaks at 44.4°, 51.8° and 76.3° correspond to (1 1 1), (2 0 0) and (2 2 0) lattice planes of metallic Ni [33,37–41]. The X-ray diffraction pattern of the calcined sample (Fig. 6(b)) exhibits intense and sharp peaks at 2θ values of 37.2°, 43.3°, 62.8°, 75.4° and 79.3°, characteristic of nickel oxide with cubic crystalline structure [34,42–45]. The higher peak intensities in Fig. 6(b) indicate densification and increase of crystallite sizes after annealing at 800 °C.

4. Conclusion

High purity nickel oxide was synthesized by the proposed modified sol-gel method using nickel acetate, citric acid and ethylene glycol as precursors. The size of the obtained NiO crystals was of the order of micrometers. In the calcined at 800 °C resin only Ni and O were detected by EDS, while in the pre-calcined material ~54 weight % of carbon was found. The XRD diffraction revealed cubic crystalline structure of NiO. In addition, the XPS data indicated that the obtained nickel oxide is with composition close to stoichiometric but with defects related to Ni vacancies. Raman and FTIR measurements displayed only peaks characteristic of NiO. The proposed method has several advantages, such as green synthesis, short reaction times and low-cost that make it attractive for potential applications in electronic and optoelectronic devices.

Conflict of interest

The authors declare that they have no conflicts of interest.

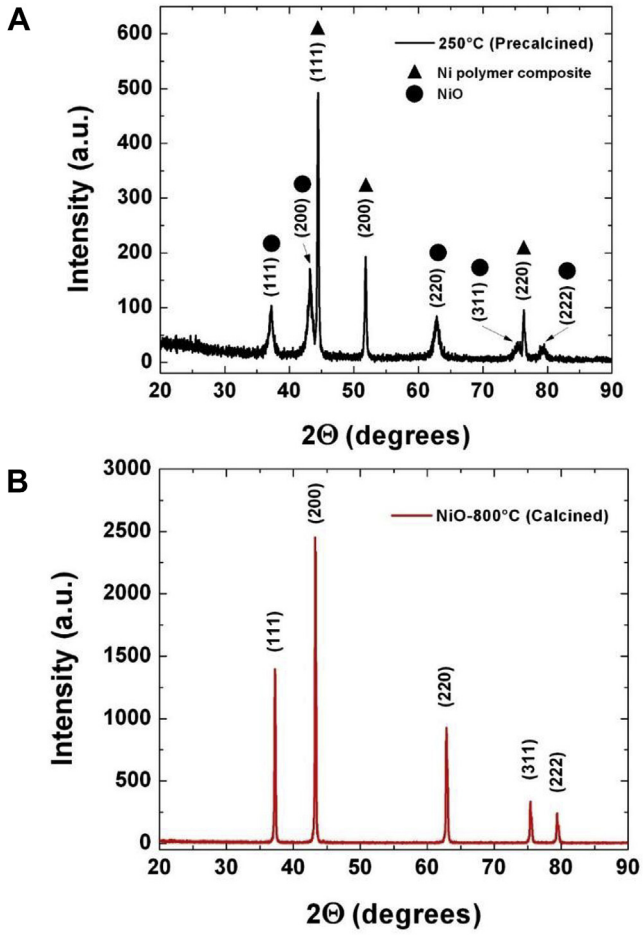

Fig. 6. X-ray diffraction patterns of NiO after annealing at 250 °C (a) and 800 °C (b).

Acknowledgments

The authors would like to thank David Dominguez for the XPS data support and gratefully acknowledge the financial support of the Universidad Autónoma de Baja California (20va Convocatoria Interna: 111/6/N/82/20) and the UNAM projects PAPIIT IN110018, IN112117 and IA101018 and PAPIME PE100318 and PE101317.

References

[1] F. Shan, A. Liu, H. Zhu, W. Kong, J. Liu, B. Shin, E. Fortunato, R. Martins, G. Liu, High-mobility p-type NiOx thin-film transistors processed at low temperatures with Al2O3 high-k dielectric, J. Mater. Chem. C 4 (2016) 9439–9444.
[2] R. Paulose, R. Mohan, V. Parihar, Nanostructured nickel oxide and its electrochemical behaviour—a brief review, Nano-Structures & Nano-Objects 11 (2017) 102–111.
[3] L.G. Teoh, K.D. Li, Synthesis and characterization of NiO nanoparticles by sol–gel method, Mater. Trans. 53 (12) (2012) 2135–2140.
[4] D. Adler, J. Feinleib, Electrical and optical properties of narrow-band materials, Phys. Rev. B 2 (8) (1970) 3112.
[5] M. Jlassi, I. Sta, M. Hajji, H. Ezzaouia, Optical and electrical properties of nickel oxide thin films synthesized by sol–gel spin coating, Mater. Sci. Semicond. Process. 21 (2014) 7–13.
[6] Y. Zhao, H. Wang, C. Wu, Z.F. Shi, F.B. Gao, W.C. Li, G.T. Du, Structures, electrical and optical properties of nickel oxide films by radio frequency magnetron sputtering, Vacuum 103 (2014) 14–16.
[7] H. Sato, T. Minami, S. Takata, T. Yamada, Transparent conducting p-type NiO thin films prepared by magnetron sputtering, Thin Solid Films 236 (1–2) (1993) 27–31.
[8] B. Sasi, K.G. Gopchandran, Nanostructured mesoporous nickel oxide thin films, Nanotechnology 18 (2007) 115613.
[9] T. Lin, X. Li, J. Jang, High performance p-type NiOx thin-film transistor by Sn doping, Appl. Phys. Lett. 108 (23) (2016) 233503.
[10] E. Avendan, L. Berggren, G.A. Niklasson, C.G. Granqvist, A. Azens, Electrochromic materials and devices: brief survey and new data on optical absorption in tungsten

oxide and nickel oxide films, Thin Solid Films 496 (2006) 30–36.
[11] Z. Jiao, M. Wu, Z. Qin, H. Xu, The electrochromic characteristics of sol–gel-prepared NiO thin film, Nanotechnology 14 (4) (2003) 458.
[12] D.S. Dalavi, R.S. Devan, R.S. Patil, Y.R. Ma, P.S. Patil, Electrochromic performance of sol–gel deposited NiO thin film, Mater. Lett. 90 (2013) 60–63.
[13] S.H. Park, S.H. Kang, C.S. Johnson, K. Amine, M.M. Thackeray, Lithium–manganese–nickel-oxide electrodes with integrated layered–spinel structures for lithium batteries, Electrochem. Commun. 9 (2007) 262–268.
[14] I. Hotovy, J. Huran, L. Spiess, S. Hascik, V. Rehacek, Preparation of nickel oxide thin films for gas sensors applications, Sens. Actuators, B 57 (1999) 147–152.
[15] G. Eranna, B.C. Joshi, D.P. Runthala, R.P. Gupta, Oxide materials for development of integrated gas sensors—a comprehensive review, Crit. Rev. Solid State Mater. Sci. 29 (3–4) (2004) 111–188.
[16] I. Hotovy, J. Huran, L. Spiess, R. Capkovic, S. Hascik, Preparation and characterization of NiO thin films for gas sensor applications, Vacuum 58 (2–3) (2000) 300–307.
[17] I. Hotovy, J. Huran, P. Siciliano, S. Capone, L. Spiess, V. Rehacek, The influences of preparation parameters on NiO thin film properties for gas-sensing application, Sensor. Actuator. B Chem. 78 (1–3) (2001) 126–132.
[18] C. Luyo, R. Ionescu, L.F. Reyes, Z. Topalian, W. Estrada, E. Llobet, C.G. Granqvist, P. Heszler, Gas sensing response of NiO nanoparticle films made by reactive gas deposition, Sensor. Actuator. B Chem. 138 (1) (2009) 14–20.
[19] S. Hufner, Electronic structure of NiO and related 3d-transition-metal compounds, Adv. Phys. 43 (1994) 183–356.
[20] D. Zhang, S. Nozaki, K. Uchida, NiO/Si heterostructures formed by UV oxidation of nickel deposited on Si substrates, J. Vac. Sci. Technol., B 32 (2014) 031202.
[21] H. Sun, S.C. Chen, S.W. Hsu, C.K. Wen, T.H. Chuang, X. Wang, Microstructures and optoelectronic properties of nickel oxide films deposited by reactive magnetron sputtering at various working pressures of pure oxygen environment, Ceram. Int. 43 (2017) 369–375.
[22] J. Keraudy, B. Delfour-Peyrethon, A. Ferrec, J. Garcia-Molleja, M. Richard-Plouet, C. Payen, J. Hamon, B. Corraze, A. Goullet, P.-Y. Jouan, Process- and optoelectronic-control of NiOx thin films deposited by reactive high power impulse magnetron sputtering, J. Appl. Phys. 121 (2017) 171916.
[23] R. LoNigro, S. Battiato, G. Greco, P. Fiorenza, F. Roccaforte, G. Malandrino, Metal Organic Chemical Vapor Deposition of nickel oxide thin films for wide band gap device technology, Thin Solid Films 563 (2014) 50–55.
[24] Y. Wu, X. Wang, Preparation and characterization of single-phase α-Fe2O3 nanopowders by Pechini sol–gel method, Mater. Lett. 65 (13) (2011) 2062–2065.
[25] Pechini MP, U.S. Patent 3,330,697, July 11, 1967.
[26] P.A. Lessing, Ceram. Bull. 68 (1989) 1002.
[27] W. Schafer, A. Koch, U. Herold-Shmidt, D. Stolten, Materials, interfaces and production techniques for planar solid oxide fuel cells, Solid State Ionics 86–88 (1996) 1235–1239.
[28] M.C. Biesinger, B.P. Payne, L.W.M. Lau, A. Gerson, R.S.C. Smart, X-ray photoelectron spectroscopic chemical state quantification of mixed nickel metal, oxide and hydroxide systems, Surf. Interface Anal. 41 (4) (2009) 324–332.
[29] A.P. Grosvenor, M.C. Biesinger, R.S.C. Smart, N.S. Mc Intyre, New interpretations of XPS spectra of nickel metal and oxides, Surf. Sci. 600 (9) (2006) 1771–1779.
[30] B.P. Payne, M.C. Biesinger, N.S. McIntyre, The study of polycrystalline nickel metal oxidation by water vapour, J. Electron. Spectrosc. Relat. Phenom. 175 (1–3) (2009) 55–65.
[31] L.A. García-Cerda, L.E. Romo-Mendoza, M.A. Quevedo-López, Synthesis and characterization of NiO nanoparticles and their PMMA nanocomposites obtained by in situ bulk polymerization, J. Mater. Sci. 44 (2009) 4553–4556.
[32] D. Dong, W. Wang, G. Dong, F. Zhang, Y. He, Y. Hang, F. Liu, M. Wang, X. Diao, Electrochromic properties and performance of NiO_x films and their corresponding all-thin-film flexible devices prepared by reactive DC magnetron sputtering, Appl. Surf. Sci. 383 (2016) 49–56.
[33] M. Salavati-Niasari, F. Davar, Z. Fereshteh, Synthesis of nickel and nickel oxide nanoparticles via heat-treatment of simple octanoate precursor, J. Alloy. Comp. 493 (2010) 410–414.
[34] N. Dharmaraj, P. Prabu, S. Nagarajan, C.H. Kim, J.H. Park, H.Y. Kim, Synthesis of nickel oxide nanoparticles using nickel acetate and poly(vinyl acetate) precursor, Mater. Sci. Eng., A 128 (2006) 111–114.
[35] M.P. Browne, H. Nolan, N.C. Berner, G.S. Duesberg, P.E. Colavita, M.E.G. Lyons, Electrochromic nickel oxide films for smart window applications, Int. J. Electrochem Sci. 11 (2016) 6636–6647.
[36] O. Diaz-Morales, D. Ferrus-Suspedra, M.T.M. Koper, The importance of nickel oxyhydroxide deprotonation on its activity towards electrochemical water oxidation, Chem. Sci. 7 (2016) 2639.
[37] Y. Sahoo, Y. He, M.T. Swihart, S. Wang, H. Luo, M.T. Furlani, P.N. Prasad, An aerosol-mediated magnetic colloid: study of nickel nanoparticles, J. Appl. Phys. 98 (2005) 054308.
[38] A.S. Danial, M.M. Saleh, S.A. Salih, M.I. Awad, On the synthesis of nickel oxide nanoparticles by sol–gel technique and its electrocatalytic oxidation of glucose, J. Power Sources 293 (2015) 101–108.
[39] L.A. Garcia-Cerda, L.E. Romo-Mendoza, M.A. Quevedo-Lopez, Synthesis and characterization of NiO nanoparticles and their PMMA nanocomposites obtained by in situ bulk polymerization, J. Mater. Sci. 44 (17) (2009) 4553–4556.
[40] E.V. Gopalan, K.A. Malini, G. Santhoshkumar, T.N. Narayanan, P.A. Joy, I.A. Al-Omari, M.R. Anantharaman, Template-assisted synthesis and characterization of passivated nickel nanoparticles, Nanoscale Res. Lett. 5 (5) (2010) 889.
[41] Y. Hou, H. Kondoh, T. Ohta, S. Gao, Size-controlled synthesis of nickel nanoparticles, Appl. Surf. Sci. 241 (1–2) (2005) 218–222.
[42] L.G. Teoh, K.D. Li, Synthesis and characterization of NiO nanoparticles by sol–gel method, Mater. Trans. 12 (2012) 2135–2140.
[43] M. Alagiri, S. Ponnusamy, C. Muthamizhchelvan, Synthesis and characterization of NiO nanoparticles by sol–gel method, J. Mater. Sci. Mater. Electron. 23 (2012) 728–732.
[44] K.W. Nam, W.S. Yoon, K.B. Kim, X-ray absorption spectroscopy studies of nickel oxide thin film electrodes for supercapacitors, Electrochim. Acta 47 (2002) 3201–3209.
[45] M. Salavati-Niasari, N. Mir, F. Davar, A novel precursor in preparation and characterization of nickel oxide nanoparticles via thermal decomposition approach, J. Alloy. Comp. 493 (2009) 163–168.

sensors

MDPI

Article

UV Sensitivity of MOS Structures with Silicon Nanoclusters

Mario Curiel [1], Nicola Nedev [1,*], Judith Paz [1], Oscar Perez [1], Benjamin Valdez [1], David Mateos [1], Abraham Arias [2], Diana Nesheva [3], Emil Manolov [3], Roumen Nedev [4] and Valeri Dzhurkov [3]

1 Universidad Autónoma de Baja California, Instituto de Ingeniería, Benito Juárez Blvd., s/n, 21280 Mexicali, Baja California, México; mcuriel@uabc.edu.mx (M.C.); judith.paz@uabc.edu.mx (J.P.); oscar.manuel.perez.landeros@uabc.edu.mx (O.P.); benval@uabc.edu.mx (B.V.); david.mateos@uabc.edu.mx (D.M.)

2 Universidad Autónoma de Baja California, Facultad de Ingeniería, Benito Juárez Blvd., s/n, 21280 Mexicali, Baja California, México; arias.abraham@uabc.edu.mx

3 Institute of Solid State Physics, Bulgarian Academy of Sciences,72 Tzarigradsko Chaussee Blvd,1784 Sofia, Bulgaria; nesheva@issp.bas.bg (D.N.); e.manolov1@gmail.com (E.M.); valeri.dzhurkov@gmail.com (V.D.)

4 Universidad Politécnica de Baja California, Calle de la Claridad s/n, 21376 Mexicali, Baja California, México; rnikolovn@upbc.edu.mx

* Correspondence: nicolan@uabc.edu.mx

Received: 31 March 2019; Accepted: 26 April 2019; Published: 17 May 2019

Abstract: Selective UV sensitivity was observed in Metal-Oxide-Semiconductor structures with Si nanoclusters. Si nanocrystals and amorphous Si nanoparticles (a-Si NPs) were obtained by furnace annealing of SiO_x films with x = 1.15 for 60 min in N_2 at 1000 and 700 °C, respectively. XPS and TEM analysis prove phase separation and formation of Si nanocrystals in SiO_2, while the a-Si NPs are formed in $SiO_{1.7}$ matrix. Both types of structures show selective sensitivity to UV light; the effect is more pronounced in the structure with nanocrystals. The responsivity of the nanocrystal structure to 365 nm UV light is ~ 4 times higher than that to green light at 4 V applied to the top contact. The observed effect is explained by assuming that only short wavelength radiation generates photocarriers in the amorphous and crystalline nanoclusters.

Keywords: UV; selective sensitivity; MOS; Si nanoclusters

1. Introduction

Metal-Oxide-Semiconductor (MOS) structures with silicon nanocrystals have been actively studied for electronic and optoelectronic applications in the past decades [1–4]. The processes of formation of silicon nanoclusters (Si NCs) in MOS structures are compatible with today's microelectronic technology, which make them applicable in floating gate non-volatile memory devices [1,4], Si based light emitters [5,6] and "third generation" solar cells [7]. Thin SiO_x films containing amorphous and/or crystalline Si nanoclusters are promising for application in optoelectronic devices, because of quantum effects in the NCs. The electrical and optoelectronic properties of MIS structures with NCs depend strongly on the Si nanoparticle size, as well as on the structural and dielectric properties of the surrounding medium.

Semiconductor diodes have been widely used as sensors of ultraviolet (UV) light. UV enhanced silicon photodiodes are well-established devices for UV detection [8], although they have the drawback to respond to low energy radiation. Since the Si bandgap is ~1.1 eV these photodiodes require filters to block out the visible and infrared photons. Sheng et al. have published results for a visible blind Si based UV detector that uses down-shifting luminophore, which absorbs in the 250–360 nm range and

emits at ~610 nm [9]. Recently, various wide gap semiconductors (E_g > 3.1 eV) have been studied for visible blind UV detectors. Some materials of interest are $Al_xGa_{1-x}N$ with composition varying between GaN and AlN [10,11], ZnO, NiO [12–14] and Ga_2O_3 [15]. The combination of p-NiO and n-ZnO has been used for fabrication of transparent photodiodes [13,14]. ZnO nanoparticles uniformly distributed on diatomite surface have shown strong enhancement of absorption and scattering coefficients in the 300–450 nm wavelength range [16,17]. Ga_2O_3 has a band gap close to 5 eV, which makes this material suitable for a solar-blind detector, with a cut-off below 280 nm [18–20].

Photoresponse of Metal-Oxide-Semiconductor structures with silicon nanoclusters has also been studied [21–23]. MOS photodiodes are attractive because they can be fabricated using standard processes for microelectronics. However, when considered for UV detection the MOS diodes suffer an important limitation, the main response is from visible light. In this work we present results for MOS structures with Si nanoclusters in the gate oxide with main response in the UV region, which depends on the nanocluster size.

2. Materials and Methods

Silicon oxide (SiO_x) layers with x = 1.15 and nominal thickness of 40 nm were deposited on 4–6 Ω cm (100) n-type Si wafers by thermal evaporation of silicon monoxide. The evaporation was carried out at room temperature and a vacuum of 1×10^{-3} Pa. The film thickness and deposition rate were monitored using a quartz microbalance. Before the film depositions the silicon wafers were chemically cleaned using a standard procedure for the microelectronics industry. Three groups of samples were prepared: Annealed at 250 °C for 30 min in Ar (control samples); annealed at 700 °C to form amorphous silicon nanoclusters and annealed at 1000 °C to grow Si nanocrystals in the SiO_x layer [24,25]. The high temperature annealing was carried out in nitrogen for 60 min.

TEM analysis was performed using a Jeol JEM-2010 microscope operating at 200 kV. Samples for cross-sectional view micrographs were prepared by gluing two samples film to film and then ground and milled from both sides to electron transparency. XPS spectra were measured by SPECS high resolution spectrometer using Al Kα X-ray source (1486.6 eV).

MOS capacitors were formed for electrical characterization by evaporation through a mask of Al top and back contacts. The top contacts were with diameter of 0.5 mm, thickness of ~0.5 μm and distance between the centers of two circles of 1 mm. Current-Voltage (I-V) characteristics were measured using Semiconductor Characterization System Keithley 4200-SCS. The I-V dependencies were measured in dark and under illumination with red, green, blue, UV and warm light LED diodes. According to the specifications, the UV spectrum is centered at 365 nm, while the warm light LED spectrum is similar to black body radiation at 3000 K, which does not emit in the UV range. The optical power at the sample position was measured by Thorlabs S120C Standard Photodiode Power Sensor connected to PM100USB Optical Power and Energy Meter. The obtained values for the red, green, blue, UV and warm light LEDs were 2.23, 1.9, 2.4, 0.225 and 0.81 mW/cm^2 respectively.

3. Results and Discussion

3.1. Compositional Characterization

Figure 1 a–c show XPS spectra of the Si 2p core level of SiO_x films annealed at 250, 700 and 1000 °C, respectively. The control film spectrum (Figure 1a) shows contribution of the four oxidation states of Si, according to fitting with four Gaussians curves with maximums at 100.7 eV (Si^+), 101.7 eV (Si^{2+}), 102.8 eV (Si^{3+}) and 103.8 eV (Si^{4+}). The main contribution in the suboxide matrix is from Si_2O_3 and not from the stoichiometric one, SiO_2. The XPS spectrum of the 700 °C annealed film (Figure 1b) differs from that of the control sample. The amount of excess Si atoms bonded to O in suboxides decreases significantly. A detailed observation of the 96–102 eV interval of binding energies reveals a small contribution of pure Si phase (inset). In the 1000 °C annealed sample (Figure 1c) only clearly separated peaks corresponding to stoichiometric SiO_2 and pure Si phase are observed. The doublet Si 2p 3/2, Si 2p

1/2 with binding energies of 99.4 and 99.8 eV is also observed using Gaussian fitting of the pure Si peak. The XPS measurements indicate that the matrix in which the nanoclusters are formed is stoichiometric SiO_2 and SiO_x with x = 1.7 after 1000 and 700 °C annealing, respectively.

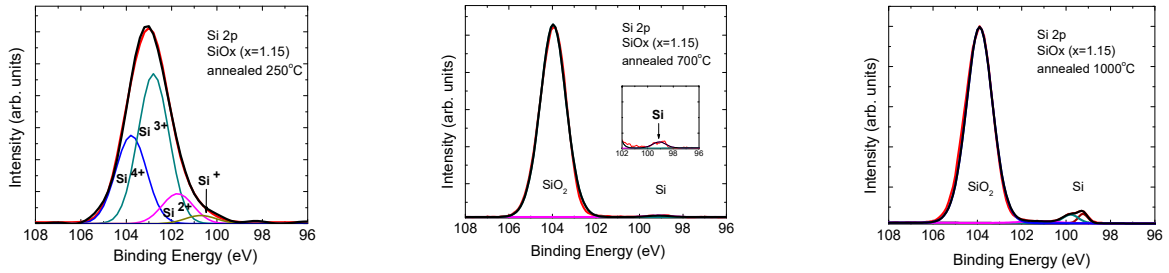

(**a**) (**b**) (**c**)

Figure 1. Si 2p core level spectra of a control SiO_x film (**a**) and of films annealed at 700 °C (**b**) and 1000 °C (**c**). The notations Si^+, Si^{2+}, Si^{3+} and Si^{4+} are used for the four oxidation states.

3.2. Structural Characterization

Figure 2a–c show cross-sectional TEM (XTEM) images of a control SiO_x film, SiO_x films annealed at 700 °C and 1000 °C, respectively. The control structure shows a homogeneous contrast of SiO_x film (Figure 2a), while the 700 °C structure image exhibits a slight contrast variation related to the amorphous nature of the Si nanoclusters (Figure 2b). The 1000 °C structure shows dark clusters resulting from silicon aggregation (Figure 2c). High resolution TEM imaging on a single dark spot reveals a crystalline nature of the cluster (left inset in Figure 2c); a Fast Fourier Transform of the high resolution TEM (HR-TEM) image reveals a periodic arrangement inside the clusters (right inset in Figure 2c). The nanocrystal diameters are in the ~4–6 nm range; the nanocrystals are randomly distributed in an amorphous matrix all along the film thickness. This observation is in good agreement with previously reported results [24,25]. In the samples with high temperature annealing a thin SiO_2 film (free of nanoclusters) of ~5 nm is seen at the film surface, most likely produced by air exposure, as has been previously reported [24].

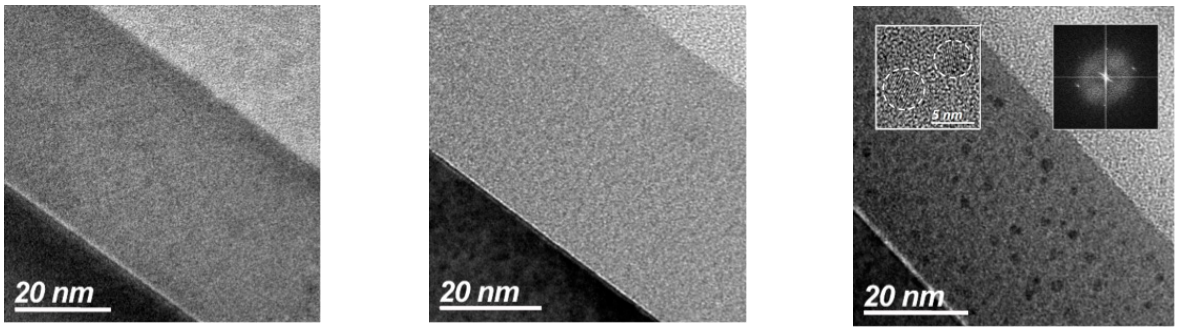

(**a**) (**b**) (**c**)

Figure 2. Cross-sectional TEM (XTEM) images of a SiO_x (1.15) control sample (**a**), and annealed at 700 °C (**b**) and 1000 °C (**c**) samples. The insets show a HR-TEM image of two crystals (left) and a Fast Fourier Transform of selected Si nanocrystal area (right).

3.3. Electrical Characterization

Figure 3a,b display I-V dependencies of c-Si/SiO_x/Al structures annealed at 700 and 1000 °C, respectively. The characteristics were measured in dark and under illumination with red, green, blue and UV light. The dark current at positive voltages is due to electrons injected from the Si substrate in the oxide, which then tunnel between neighboring nanoclusters towards the Al electrode. Almost

symmetric characteristics were measured on the structure with a-Si nanoparticles (inset in Figure 3a), while in the structure with nanocrystals the current increases faster at positive voltages (inset in Figure 3b). However, the ratio of currents flowing under forward bias (positive voltage V_g on the top electrode for n-type Si substrate) and reverse bias at $V_g = \pm 4$ V is about one order of magnitude. This is an important difference between the nanocrystal structures studied here and the ones reported in [21,22] where the current in forward direction is much higher than in reverse direction, about two orders of magnitude or more. Another difference between the dark current dependences in the insets in Figure 3 is the voltage at which exponential current increase occurs. For the structure with a-Si particles it is about 2 V, while for the nanocrystal structure it is higher, ~3 and −3.5 V forward and reverse biases, respectively. This observation is in agreement with the XPS results, which show complete phase separation and formation of Si phase in stoichiometric SiO_2 after annealing at 1000 °C. For both types of structures, the UV and blue lights cause significant increase of the current, while the green and red light lead to very small changes. It should be pointed out that the optical power of the blue LED is ~10.6 times higher than that of the UV LED, i.e., even the photoresponse to blue light is small compared to the UV response. An important difference between the I-V characteristics in Figure 3a,b is the higher current under red and green light illumination of the structure annealed at 1000 °C. The observed difference may be explained assuming that light generates photocarriers in nanoclusters outside of the top contact area, which contribute to the current through the dielectric. Part of the photogenerated carriers diffuse under the top contact due to concentration gradient and/or are driven below the contact by the electric field from distances outside the contact periphery, comparable to the layer thickness, ~40 nm. Further, these carriers are separated by the electric field and tunnel between neighboring clusters leading to an increase of the current through the MOS structure. The optical bandgap of the amorphous Si nanoclusters obtained after 700 °C annealing was estimated to be ~2.6 eV [26]. It may be assumed that the gap of the nanocrystals is ≤ 1.8 eV according to results published in [27] for nanocrystals with similar size. Thus, in amorphous nanoclusters light with wavelength (λ) close to or smaller than 480 nm can generate photocarriers, while for nanocrystals the value of λ is ≤ 690 nm.

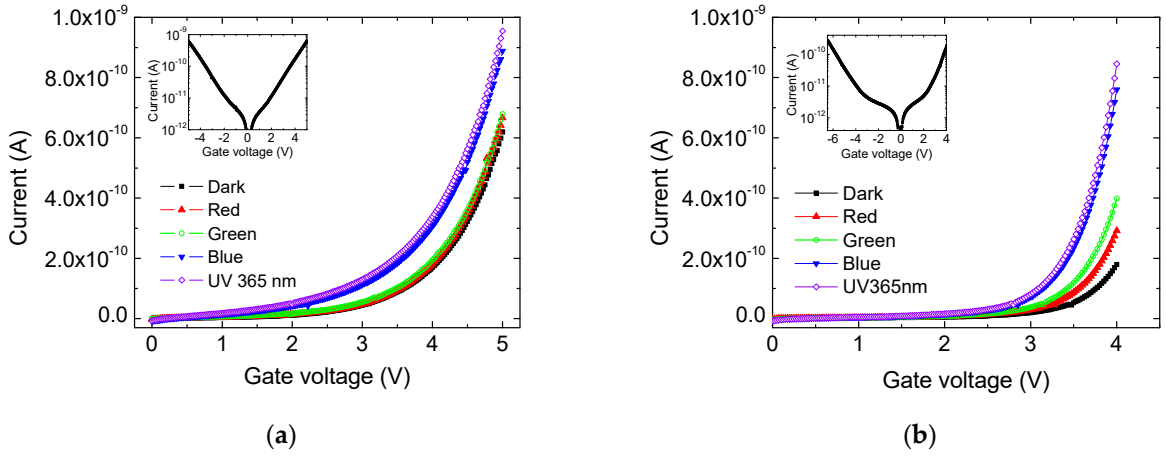

Figure 3. I-V dependencies of c-Si/SiO_x/Al structures annealed at 700 (**a**) and 1000 °C (**b**) in dark and under illumination with red, green, blue and UV light. The inset figures show dark I-V characteristics in semi-logarithmic scale measured in both directions.

The responsivity of the two types of structures at 4 V applied on the top contact is shown in Figure 4. It is clearly seen that the structure with nanocrystals show higher responsivity to UV light and is much more appropriate for application in UV sensors, though its response to green and red wavelengths is also higher. It should be pointed out that the real responsivity probably is higher than that in Figure 4, which was calculated using the top Al contact as active area. Since the Al contact is thick, the light does not penetrate below it. More likely the active area is much smaller, approximately 2πr ×film thickness, where r is the radius of the top contact. The obtained responsivity is much

smaller than the observed giant UV photoresponse in GaN nanowire photodetector decorated with Pt nanoparticles [28], as well as of the GaN based photodiodes [10]. However, the proposed structure has the advantage to be based on Si technology, i.e., uses very well developed processes which result in devices with high reliability and allow large scale production at low cost. Other advantages of the studied MOS devices compared to similar nanocrystal structures are: Higher ratio between responses in the UV and the visible range, lower dark current, especially in forward direction and lower trap density in the layer with nanoclusters, especially for holes, in contrast to results in [21]. Trapped charge carriers may cause shift of the I-V characteristics in consecutive measurements.

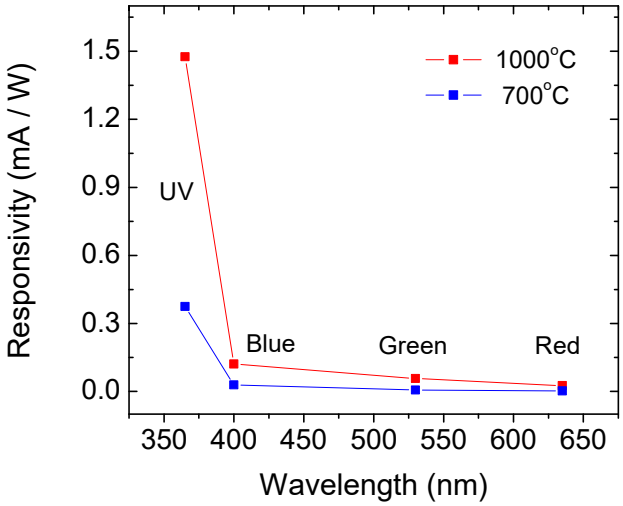

Figure 4. Responsivities at 4 V of structures with Si nanocrystals (red curve) and amorphous Si nanoparticles (blue curve).

Figure 5a,b shows I-V dependencies in dark and under warm light and UV illumination measured in lateral configuration, i.e., between two top contacts, on samples annealed at 700 and 1000 °C. In this configuration the current flows from the negatively biased Al contact through the SiO_x layer, the Si substrate and again through SiO_x to the positively biased contact. The results in Figure 5 indicates that the effect of selective UV sensitivity also exists when electrons are injected from the top metal electrode into the SiO_x at negative gate voltage, as well as from the Si substrate at positive voltage (Figure 3). Further increase of responsivity may be obtained by optimization of the MOS structure design. For example, in transversal sensor the top electrode has to be semitransparent, while in lateral structure, in addition, comb-like contacts are more appropriate.

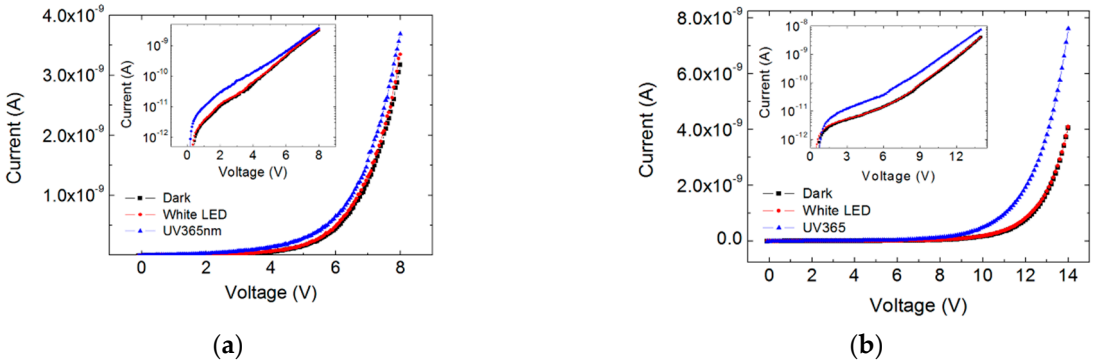

Figure 5. I-V dependencies in dark and under warm light and UV illumination measured in lateral configuration on samples annealed at 700 (**a**) and 1000 °C (**b**). The inset figures show the same dependencies in semi-logarithmic scale.

4. Conclusions

Selective UV sensitivity has been found in MOS structures with silicon nanocrystals in a SiO_2 matrix and amorphous Si nanoparticles in a $SiO_{1.7}$ matrix. I-V measurements in transversal and lateral configuration show that both types of structures have higher response to UV light than to light in the visible range. The UV selectivity is explained by assuming that light generates photocarriers in nanoclusters outside of the contact areas, which contribute to the current through the dielectric. The photogenerated carriers diffuse or are driven by the electric field under the top contacts leading to increase of the photocurrent. It was estimated that the material with a-Si nanoparticles responds to wavelengths close to or smaller than 480 nm, while the material with nanocrystals responds to wavelengths ≤ 690 nm. The observed difference results from the larger gap of the a-Si nanoparticles. The responsivity of the structure with nanocrystals to UV light is higher, which makes it attractive for UV sensor, though its response to visible light is also slightly higher. The top contacts of structures with Si nanocrystals have to be optimized in order to obtain higher responsivity when the material is used in UV sensors.

Author Contributions: Conceptualization, N.N. and D.N.; Methodology, N.N., M.C. and B.V.; Nanoparticle synthesis D.N., E.M. and V.D.; TEM, XPS, M.C., O.P.; Electrical and optical characterization, J.P., D.M., R.N., A.A.; Writing—review and editing, N.N.; Supervision, B.V.

Funding: This work was partially supported by the European Regional Development Fund within the OP "Science and Education for Smart Growth 2014–2020", project NO. BG05M2OP001-1.001-0008-C01. The authors gratefully acknowledge PFCE-2019, SEP-Mexico for funding the APC.

Conflicts of Interest: The authors declare no conflict of interest.

References

1. Ostraat, M.L.; De Blauwe, J.W.; Green, M.L.; Bell, L.D.; Brongersma, M.L.; Casperson, J.; Flagan, R.C.; Atwater, H.A. Synthesis and characterization of aerosol silicon nanocrystal nonvolatile floating-gate memory devices. *Appl. Phys. Lett.* **2001**, *79*, 433. [CrossRef]
2. Hiller, D.; Jivanescu, M.; Stesmans, A.; Zacharias, M. Pb (0) centers at the Si-nanocrystal/SiO2 interface as the dominant photoluminescence quenching defect. *J. Appl. Phys.* **2010**, *107*, 084309. [CrossRef]
3. Pavesi, L.; Turan, R. (Eds.) *Silicon Nanocrystals: Fundamentals, Synthesis and Applications*; John Wiley Sons: Hoboken, NJ, USA, 2010.
4. Tiwari, S.; Rana, F.; Hanafi, H.; Hartstein, A.; Crabbe, E.; Chan, K. A silicon nanocrystals based memory. *Appl. Phys. Lett.* **1996**, *68*, 1377. [CrossRef]
5. Walters, R.J.; Bourianoff, G.I.; Atwater, H.A. Field-effect electroluminescence in silicon nanocrystals. *Nat. Mater.* **2005**, *4*, 143. [CrossRef] [PubMed]
6. Marconi, A.; Anopchenko, A.; Wang, M.; Pucker, G.; Bellutti, P.; Pavesi, L. High power efficiency in Si-nc/SiO_2 multilayer light emitting devices by bipolar direct tunneling. *Appl. Phys. Lett.* **2009**, *94*, 221110. [CrossRef]
7. Conibeer, G.; Green, M.A.; Corkish, R.; Cho, Y.H.; Cho, E.C.; Jiang, C.W.; Fangsuwannarak, T.; Pink, E.; Huang, Y.; Puzzer, T.; et al. Silicon nanostructures for third generation photovoltaic solar cells. *Thin Solid Films* **2006**, *511–512*, 654. [CrossRef]
8. MMonroy, E.; Omnès, F.; Calle, F. Wide-bandgap semiconductor ultraviolet photodetectors. *Semicond. Sci. Technol.* **2003**, *18*, R33–R51. [CrossRef]
9. Sheng, X.; Yu, C.; Malyarchuk, V.; Lee, Y.-H.; Kim, S.; Kim, T.; Shen, L.; Horng, C.; Lutz, J.; Giebink, N.C.; et al. Silicon-Based Visible-Blind Ultraviolet Detection and Imaging Using Down-Shifting Luminophores. *Adv. Opt. Mater.* **2014**, *2*, 314–319. [CrossRef]
10. Sang, L.; Liao, M.; Sumiya, M. A Comprehensive Review of Semiconductor Ultraviolet Photodetectors: From Thin Film to One-Dimensional Nanostructures. *Sensors* **2013**, *13*, 10482–10518. [CrossRef]
11. Schühle, U.; Hochedez, J.F. Solar-blind UV detectors based on wide band gap semiconductors. *Obs. Photons Space* **2013**, *9*, 467–477.
12. Li, L.; Liu, Z.; Wang, L.; Zhang, B.; Liu, Y.; Ao, J.-P. Self-powered GaN ultraviolet photodetectors with p-NiO electrode grown by thermal oxidation. *Mat. Sci. Semicon. Proc.* **2018**, *76*, 61–64. [CrossRef]

13. Hasan, M.R.; Ting Xie, T.; Barron, S.C.; Liu, G.; Nguyen, N.V.; Motayed, A.; Rao, M.V. Self-powered p-NiO/n-ZnO heterojunction ultraviolet photodetectors fabricated on plastic substrates. *APL Mater.* **2015**, *3*, 106101. [CrossRef]
14. Patel, M.; Kim, J. Transparent NiO/ZnO heterojunction for ultra-performing zero-bias ultraviolet photodetector on plastic substrate. *J. Alloy. Compd.* **2017**, *729*, 796–801. [CrossRef]
15. Ghose, S.; Rahman, S.; Rojas-Ramirez, J.S.; Caro, M.; Droopad, R.; Arias, A.; Nedev, N. Structural and optical properties of β-Ga_2O_3 thin films grown by plasma-assisted molecular beam epitaxy. *J. Vac. Sci. Technol.* **2016**, *34*, 02L109. [CrossRef]
16. Lamastra, F.R.; Grilli, M.L.; Leahu, G.; Belardini, A.; Li Voti, R.; Sibilia, C.; Salvatori, D.; Cacciotti, I.; Nanni, F. Diatom frustules decorated with zinc oxide nanoparticles for enhanced optical properties. *Nanotechnology* **2017**, *28*, 375704. [CrossRef]
17. Lamastra, F.R.; Grilli, M.L.; Leahu, G.; Belardini, A.; Li Voti, R.; Sibilia, C.; Salvatori, D.; Cacciotti, I.; Nanni, F. Photoacoustic Spectroscopy Investigation of Zinc Oxide/Diatom Frustules Hybrid Powders. *Intern. J. Thermophys.* **2018**, *39*, 110. [CrossRef]
18. Ghose, S.; Rahman, S.; Hong, L.; Rojas-Ramirez, J.S.; Jin, H.; Park, K.; Klie, R.; Droopad, R. Growth and characterization of β-Ga_2O_3 thin films by molecular beam epitaxy for deep-UV photodetectors. *J. Appl. Phys.* **2017**, *122*, 095302. [CrossRef]
19. Patil-Chaudhari, D.; Ombaba, M.; Oh, J.Y.; Mao, H.; Montgomery, K.H.; Lange, A.; Mahajan, S.; Woodall, J.M.; Islam, M.S. Solar Blind Photodetectors Enabled by Nanotextured β-Ga_2O_3 Films Grown via Oxidation of GaAs Substrates. *Photonics J.* **2017**, *9*, 2300207. [CrossRef]
20. Arias, A.; Nedev, N.; Ghose, S.; Rojas-Ramirez, J.S.; Mateos, D.; Curiel-Alvarez, M.; Perez, O.; Suarez, M.; Valdez-Salas, B.; Droopad, R. Structural, Optical, and Electrical Characterization of β-Ga_2O_3 Thin Films Grown by Plasma-Assisted Molecular Beam Epitaxy Suitable for UV Sensing. *Adv. Mat. Sci. Eng.* **2018**, 9450157. [CrossRef]
21. Shieh, J.-M.; Lai, Y.-F.; Ni, W.-X.; Kuo, H.-C.; Fang, C.-Y.; Huang, J.Y.; Pan, C.-L. Enhanced photoresponse of a metal-oxide-semiconductor photodetector with silicon nanocrystals embedded in the oxide layer. *Appl. Phys. Lett.* **2007**, *90*, 051105. [CrossRef]
22. Yu, Z.; Aceves-Mijares, M. A ultraviolet-visible-near infrared photodetector using nanocrystalline Si superlattice. *Appl. Phys. Lett.* **2009**, *95*, 081101. [CrossRef]
23. Hossain, S.M.; Anopchenko, A.; Prezioso, S.; Ferraioli, L.; Pavesi, L.; Pucker, G.; Bellutti, P.; Binetti, S.; Acciarri, M. Subband gap photoresponse of nanocrystalline silicon in a metal-oxide-semiconductor device. *J. Appl. Phys.* **2008**, *104*, 074917. [CrossRef]
24. Curiel, M.A.; Nedev, N.; Nesheva, D.; Soares, J.; Haasch, R.; Sardela, M.; Valdez, B.; Sankaran, B.; Manolov, E.; Bineva, I.; Petrov, I. Microstructural characterization of thin SiO_x films obtained by physical vapor deposition. *Mat. Sci. Eng.* **2010**, *174*, 132–136. [CrossRef]
25. Curiel, M.; Petrov, I.; Nedev, N.; Nesheva, D.; Sardela, M.R.; Murata, Y.; Valdez, B.; Manolov, E.; Bineva, I. Formation of Si nanocrystals in thin SiO_2 films for memory device applications. *Mat. Sci. Forum* **2010**, *644*, 101. [CrossRef]
26. Nesheva, D.; Nedev, N.; Levi, Z.; Brüggemann, R.; Manolov, E.; Kirilov, K.; Meier, S. Absorption and transport properties of Si rich oxide layers annealed at various temperatures. *Semicond. Sci. Technol.* **2008**, *23*, 045015. [CrossRef]
27. Luna-López, A.; Carrillo-López, J.; Vázquez-Valerdi, D.E.; García-Salgado, G.; Díaz-Becerril, T.; Ponce-Pedraza, A.; Flores-Gracia, F.J. Morphological, compositional, structural, and optical properties of Si-nc embedded in SiO_x films. *Nanoscale Res. Lett.* **2012**, *7*, 604. [CrossRef]
28. Zhang, X.; Liu, Q.; Liu, B.; Yang, W.; Li, J.; Niu, P.; Jiang, X. Giant UV photoresponse of a GaN nanowire photodetector through effective Pt nanoparticle coupling. *J. Mater. Chem.* **2017**, *5*, 4319–4326. [CrossRef]

Journal of Materials Education Vol. 40 (1-2): 59-70 (2018)

ART, SCIENCE AND TECHNOLOGY IN STAINED GLASS WINDOWS AND IN CAVE PAINTINGS

Oscar Perez[a], Benjamin Valdez[a], Michael Schorr[a], Amir Eliezer[b], Amparo Oliveros[c], J. M. Bastidas[d]

[a] Institute of Engineering, Department of Materials, Minerals and Corrosion, Universidad Autónoma de Baja California (UABC), C.P. 21280 Mexicali, Mexico.
[b] Corrosion Research Center, Sami Shamoon College of Engineering, Beer Sheva, Israel.
[c] Faculty of Pedagogy and Educational Innovation, Universidad Autónoma de Baja California (UABC), C.P. 21280 Mexicali, Mexico.
[d] National Center for Metallurgical Research (CENIM), CSIC, Ave. Gregorio del Amo 8, C.P. 28040 Madrid, Spain.

ABSTRACT

We describe two human activities in which science and art interact to produce creative works that contribute to human culture. The first is production of stained glass windows for medieval cathedrals applying metallic nanoparticles to obtain distinct colors. The second is the ancient cave paintings depicting humans, animals and geometric symbols, by artist-painters, using ground, colored minerals, encountered in their surroundings. The materials and techniques applied are analyzed and recorded, employing instrumental and chemical methods. A selection on educational aspects is also presented, including modern trends in the formation of engineers such as Teaching of Science, Technology, Engineering and Mathematics (STEM) and Science, Technology, Engineering, Art and Mathematics (STEAM), all combined.

Keywords: *Art vs. science, metallic nanoparticles, stained glass windows, cave painting*

1. INTRODUCTION

Art and science are commonly seen as separate issues. However, since the beginning of times, art and science have been an intrinsic and essential part of human nature and activity. On the other hand, the differences between art and science are not as big as they seem. Sometimes it is a matter of parallel narratives, describing both disciplines; with linguistic creativity they can be bridged and explained. Both try to discover the great and fundamental secrets and enigmas of nature!

This article is, in certain form, a sequel of three articles already published in this journal comparing water vs blood [1], water pipelines vs blood vessels [2] and ethanol vs gasoline [3].

The first work of art is mentioned in the Bible (Exodus 31:1-11) when Bezalel, an artist "filled in wisdom, in understanding and in knowledge", was chosen to build and decorate the Ark of Testimony, using gold, silver, copper, wood, stone and textiles. During centuries famous master artists, inspired by biblical stories, created works of art: paintings, sculptures, engravings.

Science and art are interrelated human activities that complement and support each other. Yet, they also differ from one another. Science is an intellectual activity concentered with the discovery of the physical world and its phenomena entailing unbiased observations and systematic experimentation. Science involves the pursuit of knowledge, covering facts and truths about the operation of the fundamental laws of nature and the mechanisms of its processes.

Art on the other hand, comprehends the use of skills and imagination aimed at creating aesthetic objects, artifacts, environments or expressions of ideas and feelings that can be shared with other human beings. It includes a number of modes of expression such as painting, sculpture, music, dance, literature, filmmaking, theatre, etc.

In this study the two activities science and art are addressed: the stained glass windows of public structures and prehistoric paintings done on rock walls by cave dwellers.

2. THE GREAT MASTERS

If we were all born with basically similar brains, having more or less the same configuration and the same potential, why in history do only few people actually seem to execute and realize that potential?

The ordinary explanation for the existence of a Mozart, or a Leonardo da Vinci, revolves around natural talent and intelligence. How else to explain such remarkable prowess except in terms of something innate?

Their trajectories and creations made them masters, great historical figures. In this context, two extraordinary geniuses Leonardo da Vinci and Johann Wolfgang Goethe have been selected to represent the wonderful combination of science and art work, that pertain to whole humankind, for all future generations [4].

2.1 Leonardo da Vinci: artist, scientist, engineer

Born in 1452, Leonardo da Vinci was prevented from studying and practicing the traditional professions, as well as from obtaining any kind of higher education because he was an illegitimate son of the notary Piero da Vinci. However, he developed drawing skills due to his fascination for the diversity of life, rocky formations, and the waterfalls on the outskirts of the Vinci village, near to Florence. At age fourteen he started to work for the great painter Verrocchio, a place where the art work was taken as serious as science. Due to his great ability, he becomes a Verrocchio's key assistant when he was only twenty years old. Leonardo had an enormous capacity to capture extremely real and expressive faces. Recent studies have revealed some secrets about the Leonardo's layers superposition technique, making clear his detailed painting method, as well as his dedicated study of objects, plants, insects and human faces. Thus, without bowing to the circumstances, he went his own way combining arts and science.

2.2 Johann Wolfgang Goethe: writer, scientist, statesman

Johann Wolfgang von Goethe (1749-1832) born in Frankfurt on the Main, Germany, had a prominent education. He learned arts, sciences, many languages, several trades, fencing and dance. He was a person of protean talents, interests, appetites and achievements who lived

through a special time of wars and revolution in Europe. The Young Goethe joined the Leipzig University, leading a life of some excesses. In 1768 he was in the verge of death for days due to pulmonary hemorrhage. When Goethe overcomes his illness, was full of ideas and experienced an insatiable curiosity for the vital force. He harbored very rebellious thoughts that he channeled in an epistolary novel, "The sorrows of the Young Werther"; it was precursory of the movement that throughout Europe would be known as romanticism. By 1775, one year after his literary success, Goethe slowly sauntered into his new passion in the life, the sciences. He focused on geology, botany and anatomy. His style was unusual, and he concluded that all forms of the human knowledge are manifestation of the same vital force he had felt in his experience at the verge of death. He believed that the mind was made to relate things. If so, why would an individual have to stop at poesy or judge that the art and science are dissociated, or restrict their intellectual interests?

3. CULTURAL HERITAGE

The cultural heritage of a nation comprises the ancient structures, monuments, statues and physical artifacts, usually made from raw materials: stone, wood and metals [5].

The metallic tools, artistic objects and statues e.g. equestrian, constitute an integral part of the national patrimony, yet at the same time, they are the global, universal heritage of humankind since they are widely spread out through different areas, civilizations and continents [6].

Historical metalwork are part of a heritage structure or decorative elements of historic buildings which are made of copper alloys (bronze, brass) or ferrous alloys (cast or wrought iron), steels and in more modern time stainless steels, aluminum and titanium [7]. These metalwork pieces are exposed outdoors under uncontrolled environmental conditions of solar radiation, moisture, temperature, winds and chemical and physical factors, natural and anthropogenic pollutants, acid rain, and bird droppings. Buried archeological, historic and artistic artifacts suffer from corrosion by the soil chemical constituents, by microorganisms, dissolved salts and in the presence or absence of air and water [8].

The cultural and social relevance of this patrimony is evident by the activities and resources of numerous international and national, public and private, professional associations, R&D institutions, museums displaying collections of antiquities. Their laboratories and government authorities are involved in the preservation, conservation and restoration of those historic objects.

Many rock art (RA) sites, in particular cave paintings, were declared world heritage by the United Nations, Educational, Scientific and Cultural Organization, and UNESCO.

The ascending history of metals is tightly linked to the environmental conditions, in particular to the local climate, mainly its humidity and temperature and, also to the social, cultural and technological values and concepts, of the inhabitants and their political institutions, which promoted the metals permanence and their intelligent use. With advances in metallurgy knowledge and experience, these metalworkers created more corrosion resistant tools and structures, based on new alloys, casts, forging, heat treatments and protective coatings [7].

4. GLASS: ART AND INDUSTRY: ANCIENT AND MODERN

The invention of glass was, as most of discoveries, an accident. There is a story that once a ship belonging to some traders in natural soda drop anchor and scattered along the shore to prepare a meal. Since, however, no stones suitable for supporting their cauldrons were forthcoming; they rested them on lumps of soda from their cargo. When these became heated and were completely mingled with the sand on the beach a strange translucent liquid flowed forth in streams; and this, was the origin of glass.

Many materials such as wood, stone, clay,

leather, and fibers were used by ancient peoples to make their dwellings, tools, arms, cooking wares, or oil lamps. They are frequently mentioned in the Bible, but glass appears only once, in Job 28:17, "the gold and the glass cannot equal it, nor can it be exchanged for jewels of fine gold" expressing the greater value of glass.

In ancient times, artisans in Egypt, Mesopotamia, and Phoenicia created small glass bottles, with narrow long necks, by blowing molten glass, to contain perfumes and scents. The modern glass industry produces planar, transparent glasses for buildings, land vehicles and aircraft windows as well as food containers of many shapes and sizes, all under computer software control.

4.1 Glass-light interaction

The electromagnetic spectrum, which we generally call light, refers to that part of the spectrum that is visible to the human eye. The colors we see are the result of the interaction between light and matter in nanometric and greater scale. In general, the predominant mechanism for perceiving a color occurs by reflection of light in different materials, starting from the point of emission of light, bouncing on objects, until reaching our eyes. However, there are effects that occur since this light is generated: diffraction, refraction, and dispersion. A classic example of diffraction occurs in the double-slit experiment, when a beam of incident light passes through two slits with very small spacing between them an interference pattern is generated. The effect of reflection is basically when we see ourselves in a mirror, where the reflected and incident angles are the same with respect to the reflection surface. Dispersion occurs in rough objects where the light is deflected in all directions in such case, opacity effect results. Finally, when the light passes from one medium to another, its speed changes, this is called refraction, an example is the pencil in a water glass, where the light pass through three different mediums; air, water and glass, making different the angle of pencil outside and inside the glass. Glass-light interaction notably is observed in the Lycurgus Cup, a special piece of ancient glass art and industry, containing gold and silver nanoparticles made by Roman glassmakers in the fourth century A.D. Researchers at the British Museum found that the cup reflects light as a green color, while the transmitted light shows a ruby coloration. (Figure 1)

Figure 1. The Lycurgus cup, ancient glass containing metallic nanoparticles.

4.2 Metallic nanoparticles in stained glass windows

In contrast to events occurring at larger scales, at the nanoscale the quantum nature of a system dominates the response to different stimuli. A clear example of this is the metallic gray color of a large piece of silver that remains the same even if we cut it into pieces of different shapes and sizes, such as a spoon, or an earring, a

sphere, or a prism. On the other hand, the color of silver nanoparticles depends completely on their shape and size. Thus, 100 nanometer silver prisms have a red color, 100 nanometer spheres have a gray color, and 50 nanometer spheres have a blue color. For several centuries, man has made devices composed of nanoscale structures, of course, many times without knowing it. An example of this are the very colorful stained glass windows of European cathedrals that were built in the late middle ages and during the Renaissance [9,10]. (Figure 2)

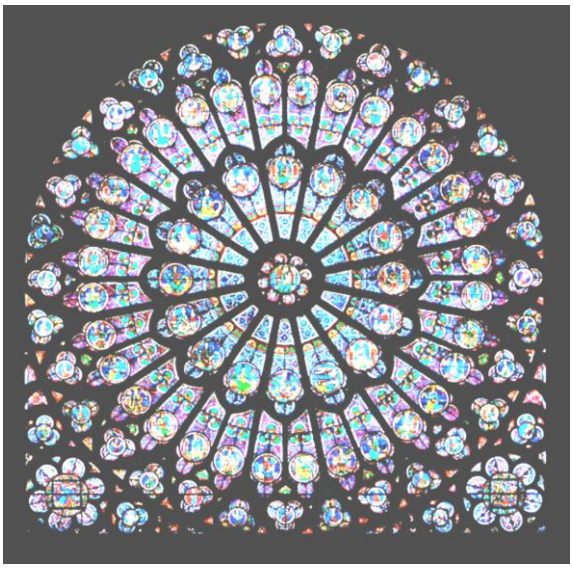

Figure 2. Stained glass windows at the Notre Dame Cathedral, Paris.

Incorporating certain salts of gold, silver, or copper, among other materials, during the manufacture of glass, made these stained glasses. Depending on the type of salt and the baking time, the colors were controlled, from yellow and green to intense red. Another more recent example is the transparent colored roof of the Cosmovitral Botanical Garden in Toluca, state of Mexico, Mexico. Considered the world's largest, it has 45 tons of blown glass, 25 tons of lead frames and 500 thousand fragments of glass, distributed in 30 thousand sections and endowed with 28 different colors [11]. (Figure 3)

H-shaped lead frames are commonly used to assemble glass parts in the stained glass windows of medieval cathedrals. These are

Figure 3. Roof of the Cosmovitral Botanical Garden, Toluca, México.

soldered to each other using a melted tin-lead alloy. Stronger metals such as iron are also used to support large glass windows panels and connect them to the walls of buildings [9]. Lead frames and iron supporting elements are a first-hand document for the study of technical and historical development of the stained glass windows of cathedrals, as well as for the evaluation of their state of conservation.

5. CAVE PAINTINGS

The prehistoric peoples started human civilization when they discovered the fire, learned to master it and prepared earthenware for coking their food. With its light and heat energy they expelled the darkness and coldness of winter nights and with a burning torch illuminated their caves to perform their pictorial arts.

Art, science and technology interact in cave paintings, which are spread out worldwide. About 30,000 years ago, human hunters-gatherers dispersed across Europe and Africa, invented new lithic and bone tools, sought the meaning of life in ritual, tribal ceremonies, and became creative artists [10]. Their fantastic achievements as galleries of mythical animals, human of both sexes, celestials and geometric figures are encountered in many countries: Altamira in Spain [12]; Lascaux in France [13]; Baja California in México [14,16]; Arizona in USA; Siberia in Russia; Botswana in Africa [17]; Patagonia in Argentina and more. Animal designs, including kangaroo-like figures, engraved on the stones of northern Australia, are among the world´s oldest art, showing that people were putting their cultural stamp on the landscape. The painters obtained theirs red ocher color as a powder, by scraping pieces of hematite, a ferric mineral. In South Africa, scientist have dated stone Age paintings created by hunters-gathers peoples some 5,700 years ago depicting humans and animals. The RA is a prominent part of the national cultural heritage of many countries and, accordingly, it is also the global heritage of the whole humankind. These RA sites are located in mountainous, desert, arid and tropical regions of several continents. In these harsh environments the painters selected their sites: walls, ceiling, shelters and caves, which provide solid rock surfaces and mineral materials to create their paints [18].

5.1 The artists

The painters-artists belonged to a notable group of the tribe, with a mission to tell a story, which played a significant role in communicating cultural values in a social context, including scenes of their life such as magic hunting. Perhaps, they believed that a deer depicted on the rock wall would help to capture it in the wilderness.

Their paintings have both elegance and strength, giving them a freshness of expression, sometimes rather rugged and naive. The artists expressed an artistic impulse to adorn their dwellings or, perhaps, their magic temples. The famous mural painters Pablo Picasso from Spain, and Rufino Tamayo from México, visited their country cave paintings and were overwhelmed by their magnificent beauty and artistic excellence [19].

5.2 The materials: mineral pigments and painting techniques

The painter, as a creative artist, cares about his materials, tools and surfaces, needs to understand their properties and behavior and manipulates them for the preparation of his paint palette.

He encounters around his area white minerals: calcite, gypsum and kaolin, which were used as support or as diluents for colored pigments. Red, orange and yellow pigments were obtained from hematite and/or limonite; malachite and other copper containing minerals provided blue or green pigments; while black color was based on wood charcoal or carbonized bones. [20,21]. (Table 1)

Table 1. Mineral pigments for producing rock art paints.

Color	Pigment
Black	Carbon: C
White	Calcite: $CaSO_3$ Gypsum: $CaSO_4.2(H_2O)$ Kaolin: $Al_2Si_2O_5(OH)$
Red	Hematite: Fe_2O_3 Gypsum: $CaSO_4.2(H_2O)$
Orange	Hematite + Limonite: Fe_2O_3+$FeO(OH).2(H_2O)$
Yellow	Limonite: $FeO(OH).2(H_2O)$

The painters mixed these charcoal pieces with animal fat and used them for drawing contours of their fantastic animals.

The color depends also on the average particle size, on the presence of other trace metallic elements, and or whether water is chemically bonded to the crystalline structure. If the paint

is applied as a soft, thick paste, only a small amount of water was required for wet grinding. The minerals were ground in man-made round bedrock bowls, carved in the stone floor using lithic tools, and then mixed with water.

It is interesting to note that crushing, grinding and mixing were well-known techniques, widely practiced by the local tribes to prepare their gathered food. The latter consisted of hard seeds, dry fruits and starchy roots and there were processed using lithic or wooden mortar and pestle stones. The heat treatment and the grinding of the minerals change their optical, physical and mechanical properties, related to the paint applicability, such as color, particle size and shape, rheology, fluidity and viscosity, density, paste (or slurry), agglutination between particles adhesion to the rock wall and the cave ceiling. The silhouettes of the painter's hands appear in numerous cave walls, especially in the "cave of hands" in Patagonia, Argentina. The artists tell us that they were painting leaving their signature and telling: Do not forget us! (Figure 4)

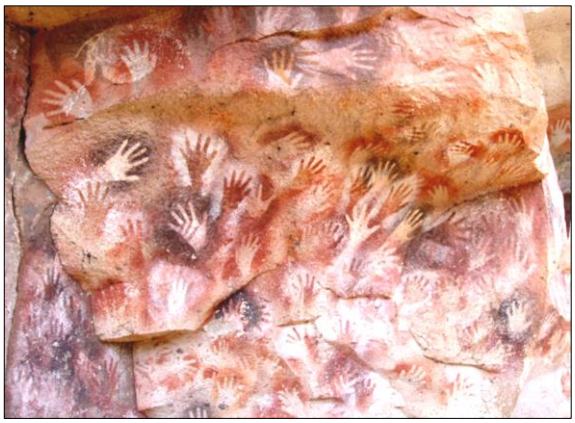

Figure 4. Cave of hands, rock art, Patagonia, Argentina.

5.3 The paintings

The thick paint was applied within incised contours or white and black outlines that were scratched on the rock rough surface with a piece of chalk or charcoal. The actions necessary for selection of the site and the paint preparation and application are presented in Table 2.

Table 2. Paint Preparation and Application

Paint preparation and application process
1.Selection of a site, cave and rock surface.
2.Mental creation of the picture composition, components and colors.
3.Collection of mineral, pigment, water and binder.
4.Crashing, grinding and comminution of the minerals in the stone bowls.
5.Mixing of ground minerals, pigment, water and binder to prepare a paste or a slurry according to solids content.
6.Application of a paste type paint, pressing and moving the hand fingers, for lines.
7.Application of a slurry type paint with animal skins by hand or with a stick, for large surfaces.
8.Penetration of the fine, wet paint particles into the rock surface of granular texture, exhibiting cracks, voids, crevices and hollows.
9.Drying, solidification and incrustation of the paint particles in the rock surface.
10.Conversion of the dry paint layer into a dense, hard, adhered and cohesive mineral-base coating.

The paintings are well preserved. No mechanical disintegration or chemical decomposition, deterioration or detachment has been observed during the last centuries, even if they are exposed to humidity, weathering, rainfall and water infiltration, to erosion by wind-borne dust, or affected by indirect or direct intense solar radiation. The applied paint returns to its original dry, natural state as mineral oxides and/or silicates, and is now an integral, adhering and cohesive layer, clinging to the rock surface.

A vivid scene of a group of painters standing on their wooden scaffolds and their assistants preparing the mineral paints is depicted in Figure 5 created by a local Mexican artist.

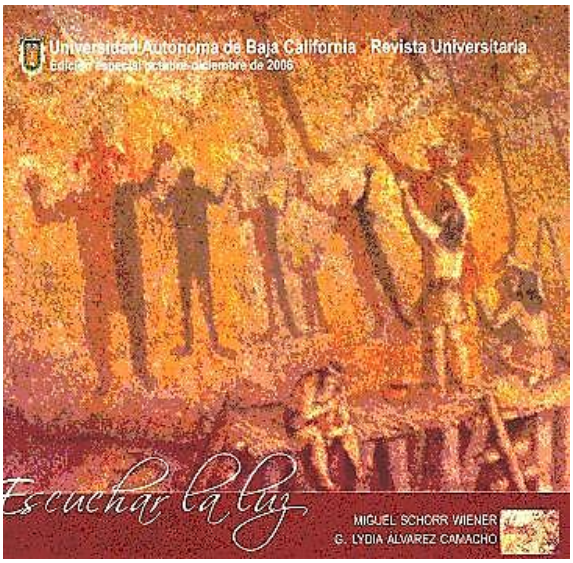

Figure 5. Rock painters standing on scaffolds.

Determination of the physicochemical characteristics, the microstructure and the texture of the polychrome painting will be extremely useful in the conservation and restoration of the rock paintings. National and regional authorities have the mission to preserve, protect and rehabilitate the RA expressions for the education and enjoyment of future generations, emphasizing the central role of art in human life.

6. METHODS AND INSTRUMENTS

At present, making, measuring, observing, and manipulating objects at nanometric scales is a challenge, it involves tools such as scanning and transmission electron microscopes, and atomic force microscopes that allow us to observe individual nanoparticles. Other tools permit us to measure the optical, magnetic, thermal, and electronic response of a set of particles. Moreover, there are sophisticated methods for the synthesis of nanostructures. These may be: physical, such as vapor deposition for ultra-thin films and electron nanolithography; or chemical methods such as colloids and reduction-oxidation, to form nanometric structures.

6.1 Microscopic examination

In microscopic examination or structural analysis, the structure of material is studied under magnification. In optical microscopes, the maximum magnification achieved is about 1,000 x. Thus, a nanometer can be scaled thousand times, therefore it is not eligible for nanostructures analysis, since the human eye distinguishes only about 100 micrometers. Fortunately, there are current technologies that achieve a magnification of up to 1,000,000 x, such as scanning electron microscopy (SEM); or with atomic resolution, such as the transmission and atomic force microscopes. Thus, we can see and analyze nanometric structures, as well as individual nanoparticles, dispersed or embedded in any material, such as resins, semiconductors, and even glass.

6.2 Chemical Analysis

Analytical methods are often classified as classical or instrumental. This classification is largely historical, as classical methods preceded instrumental methods by a century or more. In a very broad sense, an instrument for chemical analysis converts an analytical signal that is not usually detectable or directly understandable by

a human being, in a form that it is. For example, graphs of energy versus intensity, or wavelength versus refraction. Thus, an analytical instrument can be considered as a communication device between the system under study and the scientist. Some widely used instrumental methods that work by radiation emission are X-ray, UV, visible, and electron emission spectroscopies. A common method of radiation absorption used in conjunction with SEM is Energy Dispersive X-ray Spectroscopy (EDS or EDX) in which the accelerated electrons from the electron source, called electron gun, impacts and generates X-rays from the analyzed sample. There are also methods of radiation absorption, such as X-ray, UV, Visible, and IR photometry, nuclear magnetic resonance, and electron spin resonance spectroscopy.

Painting samples colored red, orange-red, black and white were collected from several sites in "El Vallecito", Tecate, Baja California, Mexico. The samples were analyzed by SEM to identify the material's morphology. In parallel, EDS analysis were carried out to obtain information about the chemical composition (Table 1).

7. COMPARATIVE STUDIES: EDUCATIONAL ASPECTS

In the last course, 2nd Semester 2017, the students prepared and discussed in the classroom the subjects of several articles. As examples, two titles and contents are mentioned:

The human culture: writers and writings, comparing the Egyptian scribes, the Hebrew writers (sofrim) of the Bible Old Testament books and writers of the Gospels New Testament, citing their themes, languages, writing tools and materials and more.

The influence of air pollution on human and animal health, emphasizing the interaction between these species and the appearance of common diseases.

Both articles have been submitted to journals belonging to public editorials, and are under revision.

Pedagogy is the science and art of teaching, being one of the oldest professions related to the development of human civilization.

The Engineering Institute of the University of Baja California is devoted to research and teaching in a culturally diverse and pluralistic faculty, with many Mexican and foreign students working on their M. Sc. and D.Sc. theses. A course entitled "Methodology of Publications" is presented to these students that are interested in writing and publishing suitable articles based on their advanced research activities.

This course is attended by many graduate students. It addresses many subjects e.g., materials engineering, conventional and renewable fuels, climate change, corrosion and protection, geothermal energy, metallic nanoparticles, medical bioengineering, marine infrastructure, materials recycling, comput-ational science and environmental challenges and. Other disciplines allow one to collaborate with industry and society by means of advanced research and education. The modern, actual factors affecting the global environment include among others increasing water and energy demands, intensifying industrial activities and growing and more urbanized population. Several selected works have already been published in JME [1, 2, 3].

The interaction between teacher and student, in the classroom and also outside, will help to implement the classical, old relation of teaching and learning, for the benefit of both, teachers and students.

The successful graduates will be expected to provide enlightened guidance and leadership to a new generation of students and to advance scientific and technical areas producing diverse comparative studies. Behind the scenes, teachers and students reach a working, tacit and comprehensive agreement that supports their academic activity.

There are well accepted tools for reflection and critical thinking: Science, Technology, Society (TST); Science, Technology, Engineering, Mathematics (STEM); and the recently expanded: Science, Technology, Engineering, Art and Mathematics (STEAM). In Institutions of High Education these tools improve the students understanding and knowledge of the partnership between science and art for the benefit of both groups. Several multidisciplinary journals are being published, devoted to the study of teaching and learning applying STEM/STEAM education disciplines. The Organization for Economic Cooperation and Development (OECD) established educational policies for Latin America based on the STEM model. It combines a number of pedagogical contents that emphasize educational strategies, including implement-ation of experimental works and finding successful mentors in the STEM area.

NACE International, linked to the National Association of Corrosion Engineers, USA relies on the STEM tool, to award scholarships to promote higher education in the area of Materials and Corrosion proving hands-on corrosion experiments and curricula for teachers to inspire, educate and excite their students.

A program called "Environment, Art and Society" created and operated by Florida International University (FIU), receives financial support from the National Science Foundation (NSF), US. It brings together multidisciplinary team of educators, researchers, managers and students, to address environment and society problems, protecting their artistic manifestation across cities and cultures. This is a multicultural, multidisciplinary, lively study that promotes the education of flexible and adaptable professionals with knowledge in basic science and modern society needs, particularly in integrated art and science.

The passion of teachers and students to achieve wisdom and understanding will make themselves better persons and the world a better place to study and to live in.

8. CLOSING REMARKS

This study presents two areas in which science and art are interconnected: the stained glass windows of European cathedrals and the cave paintings of humans, animals and celestial symbols, engraved on rock walls and shelters. Their materials nature, composition, properties and applications techniques are described. A section on the education aspects of teaching and learning, based on the principles of science and art, emphasizes their utility in the formation of engineers, with knowledge of universal culture.

The combined actions of scientists and artists have contributed to the world monuments, artifacts creations and literature that illuminate and lighten the lives of the people, during the millennia.

9. ACKNOWLEDGMENTS

The authors express their gratitude to the Project No. MAT2015-71761−R of the MINECO/FEDER, Spain, for financial support. The economic aid provided by CONACYT-Consejo Nacional de Ciencia y Tecnología with the number 415238 and the scholarship 292624, Mexico is appreciated.

REFERENCES

1. M. Schorr, N. Lotan, B. Valdez, A. Eliezer, M. Carrillo, *Metals corrosion and biological respiration: similarities and disparities: an overview, J. Mater. Ed.* **33**, 59 (2011).
2. M. Schorr, B. Valdez, E. Valdez, A. Eliezer, N. Lotan, M. Carrillo, *Water pipelines and blood vessels: a comparison of hard and soft materials, J. Mater. Ed.* **34**, 59 (2012).
3. M. Schorr, B. Valdez, E. Valdez, A. Eliezer, N. Lotan, Amparo Oliveros, M. Carrillo, R. Salinas, A. Eliezer, *A comparative study: Ethanol metabolism in the human body vs gasoline combustion in*

a vehicle motor, J. Mater. Ed. **33** (3-4) 133-140, (2011).

4. A. Greene, *Mastery, Viking,* ISBN 06700 2496 (2012).
5. L.S. Selwyn, *Metals and Corrosion: A Handbook for the Professional Conservation*, Canadian Conservation Institute, (2004).
6. D.M. Bastidas, M. Criado, S. Fajardo, V.M. Iglesias, E. Cano, J.M. Bastidas, *Copper deterioration: Causes, diagnosis and minimized risk, Int. Mater. Rev.* **55** 99 127 (2010).
7. E. Cano, De La Fuente, D.M. Bastidas, *Use of EIS for the evaluation of the protective properties of coatings for metallic cultural heritage: A review. J. Solid State Electrochem.* **14**, 381−391 (2010).
8. E. Cano, D.M. Bastidas, V. Argyropoulos, S. Fajardo, A. Siatou, J.M. Bastidas, C. Degrigny, *Electrochemical characterization of organic coatings for protection of historic steel artefacts, J. Solid State Electrochem.* **14,** 453−463 (2010).
9. M. García-Heras, M.A. Villegas, E. Cano, F. Cortés-Pizarro, J.M. Bastidas, *A conservation assessment on metallic elements from Spanish Medieval stained glass windows, J. Cult. Herit.* **5**, 311−317 (2004).
10. C. Noguez, *Comprimiendo la luz, Ciencia*, Julio-Septiembre 38-45 (2016). (Spanish)
11. E. Boynton, *A traveler's Oasis: Tolucas's Cosmovitral, http://www.oh-i-see.com* (2015).
12. C. Heras, *El descubrimiento de la cueva de Altamira.* In J.A. Lasheras (ed.) *Redescubrir Altamira*: Madrid: Turner Libros. 17-28 (2002).
13. J.P. Rigaud, *Art treasures from the ice age Lascaux cave*, National Geographic Magazine, **174** (4) 482-499 (1988).
14. J. Bendimez Patterson, *El arte rupestre del norte de Baja California, Antología de la arqueología de Baja California:* 32-40. Instituto Nacional de Antropología e Historia INAH, Mexicali, Mexico. *http//www.inah.gob.mx* (1999). (Spanish)
15. H.W. Crosby, *The Cave Paintings of Baja California. Discovering the great of an unknown people.* Sunbelt Natural History Books, Sunbelt Publications, San Diego. *http//www.harrycrosby.com* (2000).
16. J.M, Cobo, B. Valdez, M. Schorr, F. Oviedo, *Pinturas rupestres de la Rumorosa, Baja California, Mexico. Sites, rocks, materials, in "Estudios del Desierto",* M Schorr. Editor, *Editorial Universidad Autónoma de Baja California*. (2006). (Spanish)
17. B. Lee, *Botswana, Rock Paintings and Archeological Legacy,* National Geographic Magazine, **178** (6), 68-69 (1990).
18. The Economist. *Neanderthals, a rock engraving reveals an ancient form of art,* September 6th: 32 (2014).
19. J. Graff, *Saving beauty,* Time Magazine, May 15: 25-42 (2006).
20. B. Valdez, J. Cobo, M. Schorr, R. Zlatev, L. Cota, *Characterization of materials and techniques used in Mexican rock paintings*, Rock Art Research **25,** 131-135 (2008).
21. B. Valdez, J. Cobo, M. Schorr, *The physicochemical characterization of Baja California rock art,* Proceedings, International Congress of Archaeology and Rock Art, La Paz, Bolivia. 31-32. (2012).

This page intentionally left blank